DISS. ETH. NO. 26531

Experimental Investigation of Frustrated Magnetism in Two Dimensions

A thesis submitted to attain the degree of

Doctor of Sciences of ETH Zurich
(Dr. sc. ETH Zurich)

presented by

Simon Luca Bettler

MSc ETH Physics, ETH Zürich
born August 1st, 1990
citizen of
Zweisimmen BE, Switzerland

accepted on the recommendation of
Prof. Dr. Andrey Zheludev, examiner
Dr. Stéphane Raymond, co-examiner

2020

Abstract

This thesis is focused on magnetic systems where magnetic interactions are effectively restricted to two spatial dimensions. In addition, the studied materials are magnetically frustrated, meaning that the no classical, magnetically ordered ground state can simultaneously minimize the energy on all magnetic bonds. Such materials are good candidates to realize new quantum phases, either by slightly perturbing the relative strength of exchanges by chemical exchange or external pressure, or applying external magnetic fields.

As a prototype for pressure-induced ordering, where the critical pressures are known, magnetic and lattice excitations in the quantum antiferromagnet $(C_4H_{12}N_2)Cu_2Cl_6$ (PHCC) are studied across two pressure-induced phase transition at $P_c = 4.3$ kbar and $P_1 = 13.4$ kbar using Raman spectroscopy. It is confirmed that neither transition is a result of a structural transformation. The magnetic scattering shows a pronounced pressure dependence and undergoes substantial changes at both transitions. The results are in clear contradiction with previous neutron studies, which detected only minor changes of the magnon spectrum at P_1. A number of phonons show anomalous frequency shifts at low temperatures. This effect is pressure dependent and for two of the observed phonons reverses sign at around P_1. The anomalous behavior is attributed to magnetoelastic coupling in $(C_4H_{12}N_2)Cu_2Cl_6$.

Again using Raman spectroscopy, magnetic and vibrational excitations in the Shastry-Sutherland material $SrCu_2(BO_3)_2$ are studied using Raman spectroscopy at hydrostatic pressures up to 34 kbar and temperatures down to 2.6 K. The frequency of a particular optical phonon, the so-called pantograph mode, shows a very strong anomalous temperature dependence below about 40 K. We link the magnitude of the effect to the magnetic exchange energy on the dimer bonds in the Sutherland-Shastry spin lattice in this material. The corresponding dimer spin correlations are quantitatively estimated and found to be strongly pressure dependent. At around $P_2 \sim 22$ kbar they switch from antiferromagnetic to being predominantly ferromagnetic.

Single crystal neutron diffraction, inelastic neutron scattering, magnetization and magnetic torque experiments are used to study the phase diagram, magnetic structure and spin waves in $Pb_2VO(PO_4)_2$, a prototypical layered $S = 1/2$

ferromagnet with frustrating next nearest neighbor antiferromagnetic interactions. The observed excitation spectrum is found to be inconsistent with a simple square lattice model previously proposed for this material. At least four distinct exchange coupling constants are required to reproduce the measured spin wave dispersion. The degree of magnetic frustration is correspondingly revised and found to be substantially smaller than in all previous estimates. A previously unreported phase is revealed just below the saturation field for an external field applied perpendicular to the *ab*-plane.

Zusammenfassung

Diese Dissertation befasst sich mit magnetischen Systemen, in welchen sich die Wechselwirkungen primär auf zwei Raumdimensionen begeschränken. Zusätzlich sind die magnetischen Wechselwirkungen in den untersuchten Materialien frustriert. Das bedeutet, dass kein klassischer, magnetisch geordneter Grundzustand gleichzeitig die Bindungsenergie aller magnetischen Bindungen minimieren kann. Solche Materialien sind vielversprechende Kandidaten, um neue Quantenphasen zu realisieren. Diese können durch eine Veränderung der relativen Stärke der Wechselwirkungen, oder anlegen eines externen Feldes geschehen. Die relative Stärke von Wechselwirkungen wird meist durch chemische Substitution oder externen Druck verändert. Als Prototypen für druckinduzierte Ordnung in einem Quantenparamagneten untersuchen wir das Material $(C_4H_{12}N_2)Cu_2Cl_6$. Mittels Ramanspektroskopie werden die Signaturen zweier druckinduzierter Phasenübergänge bei $P_c = 4.3$ kbar und $P_1 = 13.4$ kbar im Spektrum magnetischer und Gitteranregungen analysiert. Es bestätigt sich, dass keiner der beiden Übergänge struktureller Natur ist. Die magnetischen Anregungen sind stark druckabhängig und verändern sich bei beiden Übergängen substantiell. Dies ist im klaren Widerspruch zu früheren Untersuchungen mittels Neutronenstreuung, welche nur eine geringfügige Veränderung des Magnonenspektrums bei P_1 fanden. Mehrere Phononen zeigen ungewöhnliche Veränderungen der Phononenfrequenz bei tiefen Temperaturen. Dieser Effekt ist druckabhängig und für zwei der ungewöhnlichen Phononen wird ein Vorzeichenwechsel des Effekts bei P_1 beobachtet. Dieses ungewöhnliche Verhalten wird magnetoelastischer Kopplung in $(C_4H_{12}N_2)Cu_2Cl_6$ zugeschrieben.

Mit derselben Strategie werden die magnetischen und Gitteranregungen im Shastry-Sutherland-Material $SrCu_2(BO_3)_2$ bei hydrostatischen Drücken bis zu 34 kbar und Tieftemperaturen bis 2.6 K erforscht. Die Frequenz eines bestimmten optischen Phonons, der sogenannten Pantograph-mode, zeigt eine sehr starke, ungewöhnliche Temperaturabhängigkeit unterhalb von 40 K. Wir zeigen, dass die Stärke des Effekts proportional zur magnetischen Austauschenergie auf der Dimer-Bindung ist. Die entsprechenden Spin-Korrelationen auf der Dimer-Bindung werden quantitativ abgeschätzt und zeigen eine starke Druck-

abhängigkeit. Bei cirka $P_2 \sim 22$ kbar wechseln die Dimer-Korrelationen das Vorzeichen und sind oberhalb dieses Drucks vornehmlich ferromagnetisch.

Neben diesen Studien druckinduzierter Phasenübergänge in Quantenmagneten werden mittels Neutronendiffraktion und -spektroskopie an Einkristallen, Messungen des magnetischen Drehmoments im Hochfeld und der Magnetisierung das Phasendiagramm, die magnetische Struktur und die Spinwellen in $Pb_2VO(PO_4)_2$ untersucht. Dieses Material ist ein prototypischer, geschichteter $S = 1/2$ Ferromagnet mit frustrierenden antiferromagnetischen Wechselwirkungen mit seinen übernächsten Nachbarn. Das beobachtete Spinwellen-Spektrum ist nicht mit einem simplen frustrierten Quadratgitter vereinbar, welches bisher zur Beschreibung dieses Materials herangezogen wurde. Mindestens vier unterschiedliche Austauschwechselwirkungen sind notwendig, um die gemessenen Spinwellen angemessen zu beschreiben. Der Grad magnetischer Frustration wird dementsprechend revidiert und ist signifikant kleiner als in vorherigen Abschätzungen. Eine bisher unbekannte Phase wird knapp unterhalb des Saturierungsfelds beobachtet, wenn das externe Feld senkrecht zu den 2D-Schichten in der *ab*-Ebene angelegt wird.

Contents

Acknowledgments

This project could not have been realized without the help and support of a large number of people and institutions who were involved. Firstly, I would like to express my profound gratitude to my advisor Prof. Andrey Zheludev for the continuous support of my Ph.D study, for his patience, motivation, insightful anecdotes and the guidance to keep me on track. I would also like to express my gratitude to Dr. Stéphane Raymond for being a co-examiner of this thesis and supporting me during the experiment on IN12 at the ILL in Grenoble. It goes without saying that the outcome of a neutron scattering experiment heavily depends on the local support at the facility. I truly appreciate the efforts of Eric Ressouche and Ketty Beauvois(D23, ILL, Grenoble) and Yiming Qiu (MACS, NCNR, Gaithersburgh MD). The torque magnetometry experiments were carried out with the support of Ilya Sheikin at the LNCMI-G. Complementary Electron Spin Resonance experiments on $Pb_2VO(PO_4)_2$, which helped pinning down the magnetic model of $Pb_2VO(PO_4)_2$ were performed by Sergei Zvyagin and Oleksiy Ponomaryov at the Helmholtz Zentrum Dresden-Rossendorf.

I would like to acknowledge the efforts of Andreas Stuker and his team from the D-PHYS workshop as well as Isabel Altdorfer and her team from the Laboratory Support Group for the continuous support in designing and manufacturing of the sample holders for the neutron-scattering experiments, pressure cells for Raman spectroscopy as well as cryogenics and gas control systems to run the Raman experiments.

I am deeply indebted to all present and past members of our research group for the useful discussions and pleasant teamwork. Therefore, I would like to thank Brigitte Abt, Vivek Bhartiya, Dominic Blosser, Shravani Chillal, Leonardo Facheris, Yaoxuan Feng, Daniel Flavian Blasco, Stanislaw Galeski, Severian

Gvasaliya, Shohei Hayashida, Manuel Hälg, Dan Hüvonen, Florian Landolt, Alexandra Mannig, Johannes Möller, Gérard Perren, Kirill Povarov, Nicole Reynolds, Gediminas Simutis, Lena Stoppel, Matthias Thede, Alexandra Walby, Erik Wulf and Zewu Yan. I am particularly grateful for the support of Gediminas Simutis and Severian Gvasaliya to improve the spectrometer, cryostat performance and the pressure cell. I am deeply indebted to Gérard Perren and Zewu Yan who grew the crystals for these projects. Furthermore, I am very grateful to Dominic Blosser, who performed the first-principles calculations on $(C_4H_{12}N_2)Cu_2Cl_6$, helped me set up the phonon calculation for $SrCu_2(BO_3)_2$ and read my thesis draft, providing encouraging comments.

List of Publications

The present work has in parts been published in

1 **S. Bettler**, L. Stoppel, Z. Yan, S. Gvasaliya and A. Zheludev.
"Sign-switching of dimer correlations in $SrCu_2(BO_3)_2$ under hydrostatic pressure.",
Phys. Rev. Research **2**, *012010(R) (2020) doi: 10.1103/PhysRevResearch.2.012010*

2 V. K. Bhartiya, K. Yu. Povarov, D. Blosser, **S. Bettler**, Z. Yan, S. Gvasaliya, S. Raymond, E. Ressouche, K. Beauvois, J. Xu, F. Yokaichiya and A. Zheludev.
"Presaturation phase with no dipolar order in a quantum ferro-antiferromagnet.",
Phys. Rev. Research **1** *033078 (2019) doi: 10.1103/PhysRevResearch.1.033078*

3 **S. Bettler**, F. Landolt, Ö. Aksoy, Z. Yan, S. Gvasaliya, Y. Qiu, E. Ressouche, K. Beauvois, S. Raymond, A.N. Ponomaryov, S.A. Zvyagin and A. Zheludev.
"Magnetic structure and spin waves in the frustrated ferro-antiferromagnet $Pb_2VO(PO_4)_2$.",
Phys. Rev. B **99**, 184437 (2019) doi: 10.1103/PhysRevB.99.184437

4 **S. Bettler**, G. Simutis, G. Perren, D. Blosser, S. Gvasaliya and A. Zheludev.
"High pressure Raman study of the quantum magnet $(C_4H_{12}N_2)Cu_2Cl_6$.",
Phys. Rev. B **96**, 174431 (2017) doi: 10.1103/PhysRevB.96.174431

Chapter 1

Introduction

Quantum magnets are models of choice to realize the complex physics of quantum phase transitions [1] and novel quantum phases [2]. In such materials, phase transitions can often be induced by an external magnetic field, as for example in the so-called Bose-Einstein condensation (BEC) of magnons [3–5]. Another way to potentially drive these systems towards criticality is by applying external pressure and thereby changing the strength of magnetic interactions. If a material cannot choose a ground states which minimizes the energy on all magnetic bonds — such compounds are called frustrated — this approach is particularly promising. In classical spin systems, geometric frustration is usually resolved by the "least frustrated" magnetically ordered state. The actual ground state spin configuration depends on the type and strength of frustration. As a function of this parameter, one expects transitions between different ordered phases. These "classical" transition points are a promising area to look for novel *quantum* phases and excitations [2]. The aim of this PhD project is to find experimental evidence for the existence of novel phases in quantum magnets and probe their magnetic and lattice excitations. The following materials realize — to a close approximation — three transitions of great interest to condensed matter research:

1. $(C_4H_{12}N_2)Cu_2Cl_6$: Magnetic soft mode transition in a quantum paramagnet. In quantum paramagnets, i.e., spin systems with a quantum disordered spin-singlet ground state and a gap in the magnetic excitation spec-

trum a small perturbation of the exchange pathways may in rare cases lead to a complete softening of the spin gap. The result is a unique magnetic soft-mode quantum phase transition to a long range-ordered state that breaks the SO(3) symmetry of the underlying Heisenberg Hamiltonian.[1] This transition is clearly distict from the field-induced BEC which breaks only O(2) symmetry. Only a handful of real materials undergo pressure-induced magnetic quantum phase transitions of the described type. To date, only three examples are known: $TlCuCl_3$ [6, 7], $KCuCl_3$ [8] and $(C_4H_{12}N_2)Cu_2Cl_6$ (PHCC)[9–11]. In the latter, pressure-induced ordering was first detected by μ-SR at $P_c = 4.3$ kbar[9]. Inelastic neutron scattering studies confirmed the transition to be of a soft-mode nature[10, 11]. A second transition was detected in PHCC by μ-SR at a higher pressure of $P_1 \sim 13.4$ kbar[9]. It clearly corresponds to a rather drastic change in the magnetic structure, and is possibly a Lifshitz (commensurate to incommensurate) transition. Surprisingly though, inelastic neutron scattering experiments [11] did not detect any drastic changes in the excitation spectrum of PHCC upon crossing P_1. Also unknown is to what extent the crystal lattice and phonons are involved, if at all, in either of the two transitions. All these issues we address in the first part of this thesis by means of high pressure Raman spectroscopy.

2. $SrCu_2(BO_3)_2$: Transition from an exact dimer state to Néel order and possible intermediate phases in the fully frustrated Shastry-Sutherland lattice. The Shastry-Sutherland model is arguably one of the most important constructs in the field of quantum magnetism. It demonstrates that a gapped quantum paramagnet can occur in a well-connected Heisenberg spin Hamiltonian beyond the unique topology of a single dimension. Its key feature is geometric frustration of antiferromagnetic (AF) interactions between AF $S = 1/2$ dimers arranged on a particular 2-dimensional lattice such that adjacent dimers are orthogonal to one-another [12]. For sufficiently strong frustration the *exact* ground state is a product of AF singlets on each dimer bond J'. For weak frustration one recovers the semi-classical Néel-ordered phase. What happens in-between has been hotly debated [13–31]. The most intriguing intermediate phase proposed is the so-called plaquette state [16, 18, 22]. Dimer singlets are destroyed to be replaced by singlets composed of *four* spins connected via the inter-dimer bonds J. Translational symmetry is broken and some or all of the dimer spin cor-

relations become predominantly *ferromagnetic* (FM). The only known and much studied experimental realization of the model is $SrCu_2(BO_3)_2$, where $S = 1/2$ Cu^{2+} ions form dimers via Cu-O-Cu superexchange pathways, which are connected through (BO_3) units. With a frustration ratio $J/J' \sim 0.6$ it is reliably in the dimer phase, with a spin gap $\Delta = 3$ meV in the excitation spectrum[32, 33]. In this material J/J' can be continuously tuned by hydrostatic pressure [34]. The frustration ratio increases steadily with pressure, eventually leading to a Néel ordered state above 30 kbar [35]. Moreover, already at $P_c \sim 18$ kbar the original dimer phase gives way to a new quantum paramagnet, presumed to be the plaquette state [34–38]. Thus, theoretical predictions for exotic phases of the Shastry-Sutherland model are put to the experimental test. In the present work we infer the strength of dimer spin correlations in $SrCu_2(BO_3)_2$ from their effect on a particular optical phonon, called the pantograph mode. This mode is strongly affected by magnetic correlations on the dimer bond. The phonon frequency is measured with very high precision using Raman spectroscopy. We show that around P_c correlations on the dimer bond switch from AF to dominantly FM, and thereby independently confirm the destruction of the AF-dimer ground state.

3. $Pb_2VO(PO_4)_2$: A frustrated square lattice material? An outstanding example for novel ground states emerging as a consequence of frustration is the frustrated Heisenberg ferromagnet on a square lattice frustrated by antiferromagnetic (AF) next-nearest neighbor coupling. The classical model is either a collinear ferromagnet or a "columnar" AF (CAF) structure. The $S = 1/2$ quantum model near the transition between these classical states, for $-0.7 < J_2/J_1 < -0.4$, is predicted to be a so-called spin nematic.[39–41] This exotic quantum phase shows no conventional dipolar magnetic order but features spontaneously anisotropic quantum spin fluctuations. In strong enough applied fields a nematic phase is supported for all $J_2/J_1 < -0.4$.[42, 43]

To this day, the only known potential experimental realizations of the ferro-antiferro square lattice model are among layered vanadophosphates.[44] Our understanding of these compounds is far from complete though, since most experiments to date were done on powder samples. $Pb_2VO(PO_4)_2$ is perhaps the most thoroughly studied member of the series. The consensus was that this compound

is a good "baseline" ferro-antiferro square lattice system, substantially frustrated but still in the classical CAF phase. In the present work we report the results of neutron diffraction, inelastic neutron scattering, magnetization and magnetic torque measurements on *single crystal* samples of this compound. We determine how strongly the excitations deviate from those of a perfect square lattice and how two-dimensional the material really is. Furthermore, we accurately measure the direction and magnitude of the ordered moment at low temperatures and identify a previously unreported phase just below the saturation field.

Chapter 2

Models and model materials

Quantum magnets offer a large variety of linking patterns, dimensionalities and — most importantly — well-defined short-range interactions. This makes them useful prototypes in the study of quantum phase transitions and frustrated magnetism[45]. In the following, a short recapitulation of basic properties of the models and phase transitions considered in this thesis is given. The corresponding model systems studies in this work are introduced and their most important characteristics are outlined.

2.1 Pressure-induced order in weakly coupled spin-1/2 dimers

Perhaps the simplest quantum paramagnet consists of a lattice of spins with strong dimer bonds J' which are weakly coupled by inter-dimer bonds J as shown in fig.2.1. In the limit of isolated dimers ($J = 0$), the Hamiltonian is simply

$$\hat{H} = J'\mathbf{S_1}\mathbf{S_2}. \tag{2.1}$$

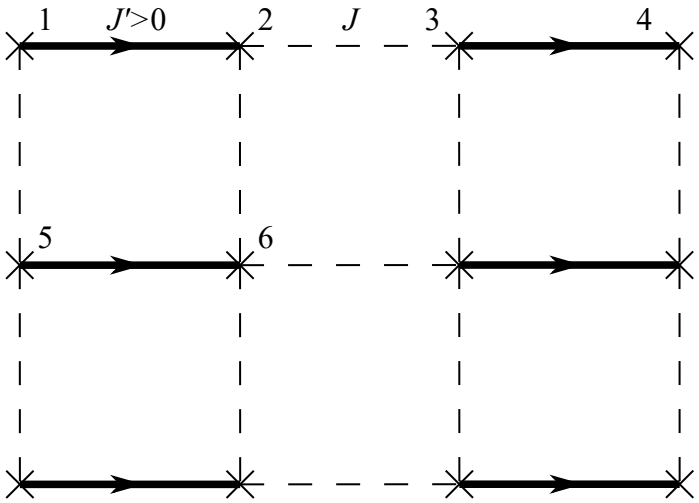

Figure 2.1: Lattice of weakly coupled dimers with intradimer(bold) and interdimer(dashed) bonds connecting localized spins(×). Arrows indicate the dimer orientation.

The possible configurations of a single pair of spins are:

$$\begin{aligned} |S_{1,2}\rangle &= \frac{|\uparrow\downarrow\rangle - |\downarrow\uparrow\rangle}{\sqrt{2}} \\ |T^{+}_{1,2}\rangle &= |\uparrow\uparrow\rangle \\ |T^{0}_{1,2}\rangle &= \frac{|\uparrow\downarrow\rangle + |\downarrow\uparrow\rangle}{\sqrt{2}} \\ |T^{-}_{1,2}\rangle &= |\downarrow\downarrow\rangle \end{aligned} \tag{2.2}$$

We can rewrite the Hamiltonian as[46]

$$\begin{aligned} \langle\hat{H}\rangle = \langle J'\vec{S_1}\vec{S_2}\rangle &= \frac{J'}{2}\left\langle (S_1+S_2)^2 - S_1^2 - S_2^2\right\rangle \\ &= \frac{J'}{2}(S_{tot})^2 - \frac{J'}{2}(\hbar S_1(S_1+1) + \hbar S_2(S_2+1)) = \frac{J'}{2}S_{tot}^2 - \frac{3J'}{4} \\ &= \frac{J'}{2}S_{tot}(S_{tot}+1) - \frac{3J'}{4} \\ &= \begin{cases} \frac{J'}{4} & \text{if } S_{tot}=1 \\ \frac{-3J'}{4} & \text{if } S_{tot}=0 \end{cases} \end{aligned} \tag{2.3}$$

There is therefore a non-degenerate ground state, which is a product of singlets, separated from the first excited states by a gap with $\Delta E = J'$.

$$\begin{aligned} |GS\rangle &= \bigotimes_{(ij)} |S_{ij}\rangle \\ |1^{st}ES\rangle &= |T^+_{ij}\rangle \bigotimes_{(i'j')} |S_{i'j'}\rangle \end{aligned} \tag{2.4}$$

While the ground state is well-defined, we can put a triplet on any of the dimers to produce an excited state. Therefore, the excited state degeneracy is equal to the number of dimers in the system.

We now want to find out how triplets hop, once we turn on J. To first order in perturbation theory, the probability for the triplet hopping from dimer (1,2) to the dimer (3,4) is

$$(\langle T^+_{1,2}| \otimes \langle S_{3,4}|)(JS_2 \cdot S_3)(|S_{1,2}\rangle \otimes |T^+_{3,4}\rangle) \tag{2.5}$$

The initial and final states are

$$\begin{aligned} \langle T^+_{1,2}| \otimes \langle S_{3,4}| &= \langle \uparrow\uparrow | \otimes \left(\frac{\langle \uparrow\downarrow | - \langle \downarrow\uparrow |}{\sqrt{2}} \right) = \frac{\langle \uparrow\uparrow\uparrow\downarrow | - \langle \uparrow\uparrow\downarrow\uparrow |}{\sqrt{2}} \\ |S_{1,2}\rangle \otimes |T^+_{3,4}\rangle &= \frac{| \uparrow\downarrow\uparrow\uparrow\rangle - | \downarrow\uparrow\uparrow\uparrow\rangle}{\sqrt{2}} \end{aligned} \tag{2.6}$$

This time it is more useful to write $S_2 \cdot S_3 = S^z_2 S^z_3 - 1/2(S^+_2 S^-_3 + S^-_2 S^+_3)$:

$$\begin{aligned} &(\langle T^+_{1,2}| \otimes \langle S_{3,4}|)(J'S_2 \cdot S_3)(|S_{1,2}\rangle \otimes |T^+_{3,4}\rangle) \\ &\quad = \frac{J'}{2} \left(\langle \uparrow\uparrow\uparrow\downarrow | - \langle \uparrow\uparrow\downarrow\uparrow | \right) \left(S^z_2 S^z_3 + 1/2(S^+_2 S^-_3 + S^-_2 S^+_3) \right) \left(| \uparrow\downarrow\uparrow\uparrow\rangle - | \downarrow\uparrow\uparrow\uparrow\rangle \right) \\ &\quad = \frac{J'}{2} \left(\langle \uparrow\uparrow\uparrow\downarrow | - \langle \uparrow\uparrow\downarrow\uparrow | \right) \left(\frac{1}{4}(-| \uparrow\downarrow\uparrow\uparrow\rangle + | \uparrow\downarrow\uparrow\uparrow\rangle) + \frac{1}{2}(| \uparrow\uparrow\downarrow\uparrow\rangle - 0 + 0 - 0) \right) \\ &\quad = -\frac{J'}{4} \end{aligned} \tag{2.7}$$

If — instead — J connected the sites 2 and 4, the sign of the hopping amplitude would be positive. If we look at the bonds $J_{1,5}$ or $J_{2,6}$ we see that we would get $-| \uparrow\uparrow\downarrow\uparrow\rangle$ and $| \uparrow\uparrow\uparrow\downarrow\rangle$ respectively and we get a hopping amplitude $J/4$ for each of these bonds. Therefore, the total amplitude for a triplet to hop from

dimer (1,2) to dimer (5,6) is $J/2$. If we Fourier transform to get the dispersion in reciprocal space, we get the dispersion

$$\hbar\omega(k) = \frac{-J}{2}\cos(k_x) + J\cos(k_y). \tag{2.8}$$

The minimum of the dispersion is located at $(k_x, k_y) = (0, \pi)$ and $\hbar\omega(0,\pi) = -\frac{3J}{2}$. So the gap of the weakly coupled dimers is in the simplest approximation $\Delta E = J' - \frac{3}{2}J$. By varying the ratio J/J', it is possible to close the gap and drive the system into a Néel ordered state. The critical value has been determined to a very high precision by by Quantum Monte Carlo simulations and is $(J/J')_c = 0.52337(3)$[47]. If the bandwith and gap are comparable a simple dimer expansion is not appropriate anymore and the excitations have to be treated in the framework of bond operator theory[]. Typically, the dispersion relation is of the form[49]:

$$\begin{aligned} \hbar\omega &= \sqrt{A + B\epsilon_k}, \\ \epsilon_k &= \sum_i c_i J_i \cos(d_{i,x}k_{i,x} + d_{i,y}k_{i,y} + d_{i,z}k_{i,z}). \end{aligned} \tag{2.9}$$

The ratio of inta- and inter-dimer couplings is not something that can be tuned at the turn of a knob in experiments. The only options to drive such a transition in a real material are to either apply external pressure or chemical substitution. The latter has the disadvantage of oftentimes introducing disorder into the system. This is why in this work hydrostatic pressure was used as a means to modify the ratio of exchange constants.

2.1.1 $(C_4H_{12}N_2)Cu_2Cl_6$

$(C_4H_{12}N_2)Cu_2Cl_6$ is an extensively studied and well understood quantum paramagnet with a gap $\Delta = 1$ meV[50]. The crystal structure is triclinic, space group $P\bar{1}$, with lattice parameters $a = 7.984(4)$, $b = 7.054(4)$, $c = 6.104(3)$ Å, $\alpha = 111.23(8)°$, $\beta = 99.95(9)°$, and $\gamma = 81.26(7)°$. [51] The magnon dispersion relation is known from neutron experiments,[50] with the magnon band extending between Δ and 2.7 meV. The topology of magnetic interactions between the $S = 1/2$ Cu^{2+} ions is believed to be rather complicated. The magnetic interactions are primarily in the (ac)-plane. The copper-chloride layers are separated

by organic spacers(Fig. 2.2b and c) with the interlayer dispersion being of the order $\lesssim$0.1 meV[52]. Therefore, an empirical Ansatz of the bond operator theory form was previously used to fit the dispersion in the (ac)-plane, both at ambient and under applied hydrostatic pressure[11, 50]:

$$\begin{aligned}(\hbar\omega(\mathbf{Q}))^2 =& B_0 + B_h\cos(2\pi h) + B_l\cos(2\pi l) \\ &+ B_{hl}(\cos(2\pi(h+l)) + \cos(2\pi(h-l))) + B_{2h}\cos(4\pi h) + B_{2l}\cos(4\pi l).\end{aligned} \tag{2.10}$$

The individual bond energies are then extracted by making use of sum rules for the equal-time structure factor[11, 50]. To some degree the system can be viewed as composed of antiferromagnetic dimers defined by the nearest neighbor exchange J_1(Fig.2.2a). However, bond energies associated with a frustrated second-nearest-neighbor coupling J_2 and the sixth-nearest-neighbor antiferromagnetic bond J_6 are only slightly, if at all, smaller. There is evidence that it is the bond J_1 that is most affected by the application of hydrostatic pressure.[11] With increasing pressure the intra-dimer bond energy $J_1\langle\mathbf{S}_0\mathbf{S}_1\rangle$ becomes progressively weaker, more than halving at 9 kbar[11].

Close to the zone boundary of the magnetic Brillouin zone, the — otherwise sharp — magnon decays into a broad two-particle continuum[53]. We will probe the pressure-dependence of this continuum with Raman spectroscopy. In addition, we will investigate the effect of magnetic correlations on lattice excitations as a function of temperature and pressure. This provides additional information on the magnetic ground state and phase transitions. This second route will be even more important for the study of magnetic correlations in the Shastry-Sutherland model system $SrCu_2(BO_3)_2$ (sec.2.2.2).

Structural motifs The crystal structure contains isolated organic cations and infinite chains of $[Cu_2Cl_6]^{2-}$ dimers parallel to the crystallographic c-axis(Fig.2.2). The organic cations and chains interact through hydrogen bonds, which provide the stability of the lattice[51]. The strongest magnetic interactions between the Cu^{2+} ions are along the so-called dimer bond. Copper ions are connected trough Cu-Cl(2)-Cu pathways with bond angles 95.8°[54]. This bond energy is E_1-1.3(3) meV[50]. The second-strongest bond runs along the crystallographic

a-direction trough Cu-Cl(1)-Cl(2)-Cu linkings. The corresponding bond energy is E_6=-0.92(5) meV. Bond 2 is frustrated with a bond energy E_2=0.7(3) meV.

Crystal Growth The crystals were grown in solution through the thermal gradient method. When large crystals were grown for inelastic neutron scattering, small, deuterated crystals were produced as a byproduct. The procedure adopted for growing large single crystals of $(C_4H_{12}N_2)Cu_2Cl_6$ for inelastic neutron scattering is described in [55]. A single crystal of $(C_4H_{12}N_2)Cu_2Cl_6$ inside the pressure cell together with ruby balls, which are used as an in-situ pressure gauge, is shown in Fig.2.3.

Sample description The used samples were deuterated crystals of $(C_4H_{12}N_2)Cu_2Cl_6$ with sizes ranging from 0.2 mm for high-pressure measurements to 3 mm for ambient pressure measurements. For high-pressure measurements the lower limit for the sample size is set by the fact that for measurements of magnetic excitations, the sample has to be oriented along a specific crystal axis within the pressure cell. The upper limit for the sample size is given by diameter of the gasket bore.

2.2 Pressure-driven phase transitions in the Shastry-Sutherland model

2.2.1 Exact dimer ground state of the Shastry-Sutherland model and its limits

In section 2.1 we considered a system of collinear dimer singlets arranged on a square lattice. What if now the dimers were arranged such that each singlet is orthogonal to its neighbours as shown in figure 2.4 with dimer bonds J', which are connected by J-bonds. Such an arrangement of dimers is called the Shastry-Sutherland model(SSM) and has an exact dimer ground state for $J/J' \lesssim 0.5$[56]. To gain insight as to why this arrangement is of particular interest amongst frustrated two-dimensional spin systems, let's show that the state with dimer singlets on all the J'-bonds is the exact ground state for an extended range of J'/J. There are two points to be shown[46]:

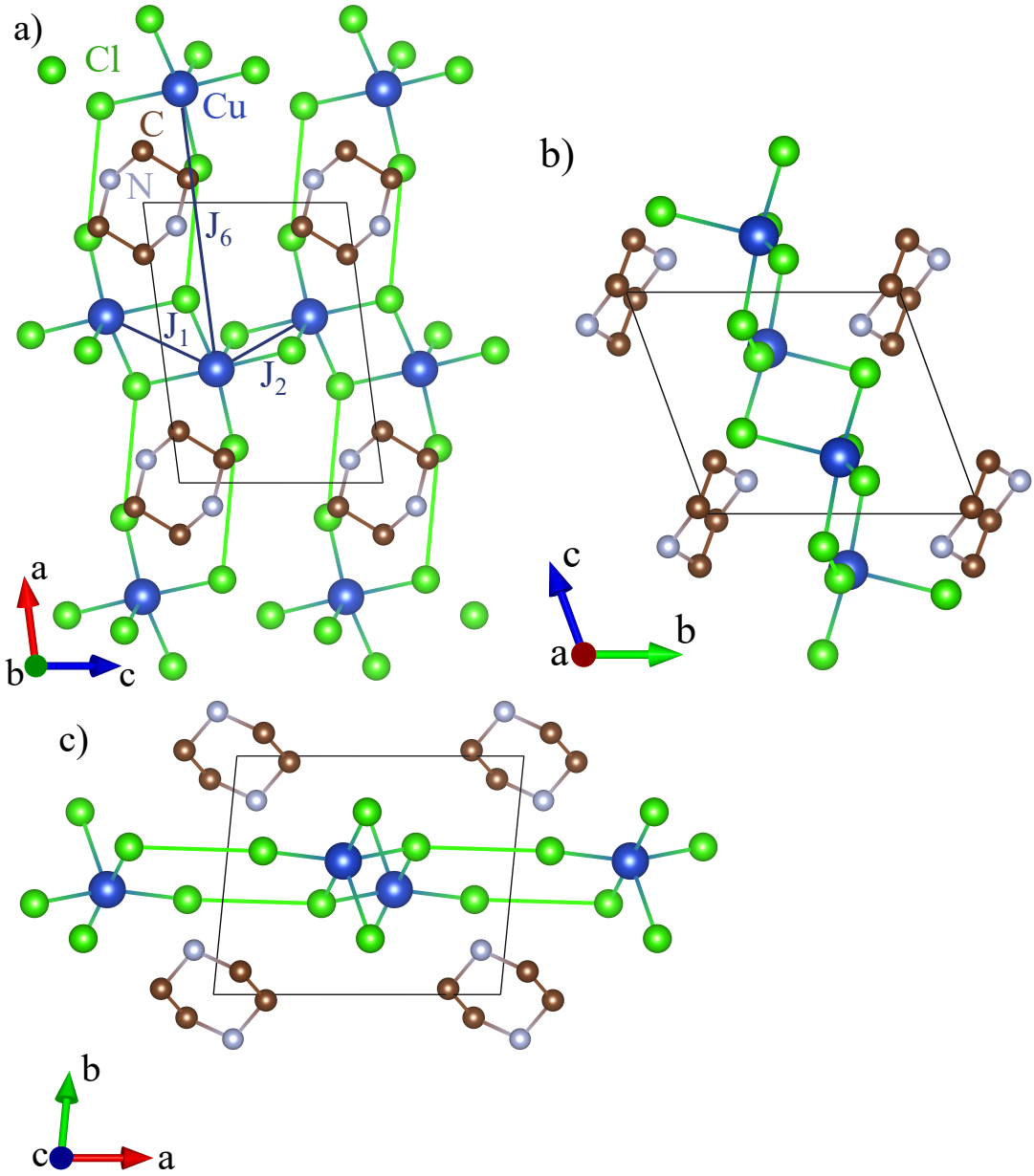

Figure 2.2: Crystal structure of $C_4H_{12}N_2)Cu_2Cl_6$ a) viewed along the crystallographic b-axis with the most important bonds indicated, b) viewed along the crystallographic a-axis, c) viewed along the crystallographic c-axis.

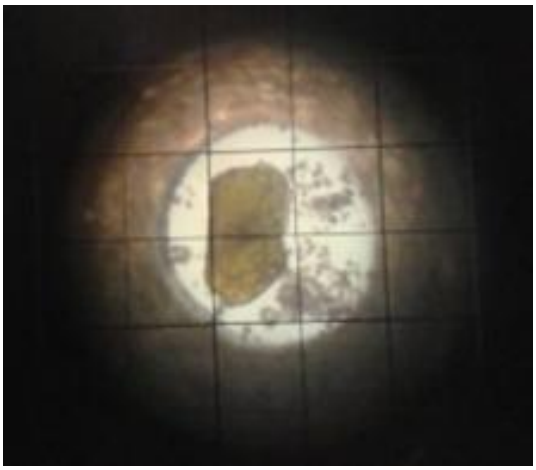

Figure 2.3: A typical cell loading with a sample of $(C_4H_{12}N_2)Cu_2Cl_6$ and rubies scattered around the sample. Gasket bore diameter ∼0.6 mm.

1. Show the dimer state is an eigenstate of the Hamiltonian,

2. Show it has the lowest possible energy.

Let's start by proving it is an eigenstate. Consider the situation depicted in Fig. 2.5a). It captures the essence of the interaction of one dimer with its neighbours. The Hamiltonian for the interaction of site 2 with sites 3 and 4 is[46]:

$$H_J = J(S_2S_3 + S_1S_4) = JS_2(S_3 + S_4), \tag{2.11}$$

where $S_2 + S_3$ can be either 0 or 1. First, we want to show that a product of singlet states is an eigenstate of this Hamiltonian. Acting with this Hamiltonian on the product state of sites 2-4, we get

$$H_J(|\sigma_2\rangle\otimes|S_{3,4}\rangle) = J\sum_\alpha S_2^\alpha(S_3^\alpha+S_4^\alpha)(|\sigma_2\rangle\otimes|S_{3,4}\rangle) = J\sum_\alpha S_2^\alpha|\sigma_2\rangle\otimes(S_3^\alpha+S_4^\alpha)|S_{3,4}\rangle. \tag{2.12}$$

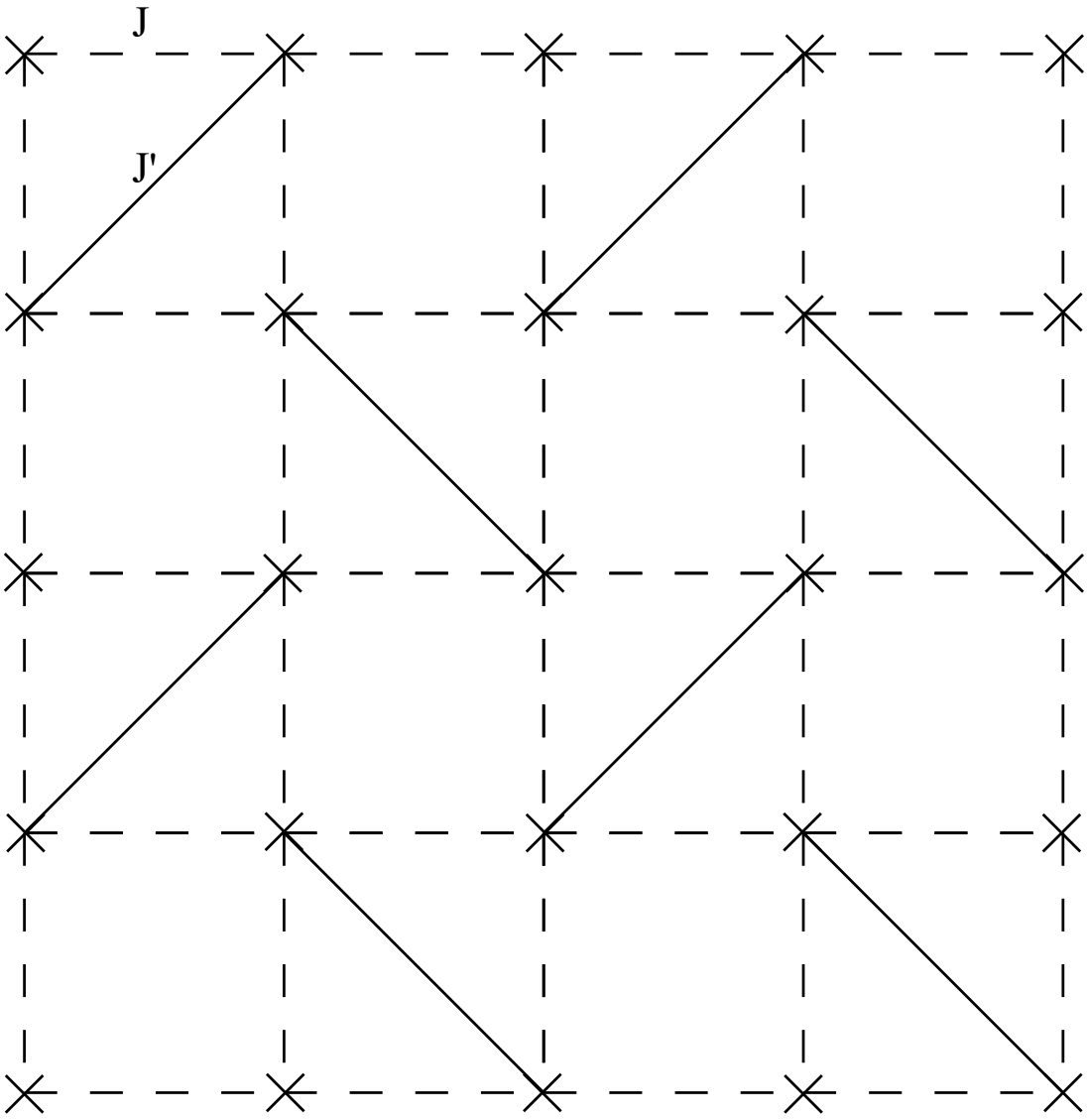

Figure 2.4: Shastry-Sutherland lattice of orthogonal dimers with exchange constant J' and inter-dimer coupling J.

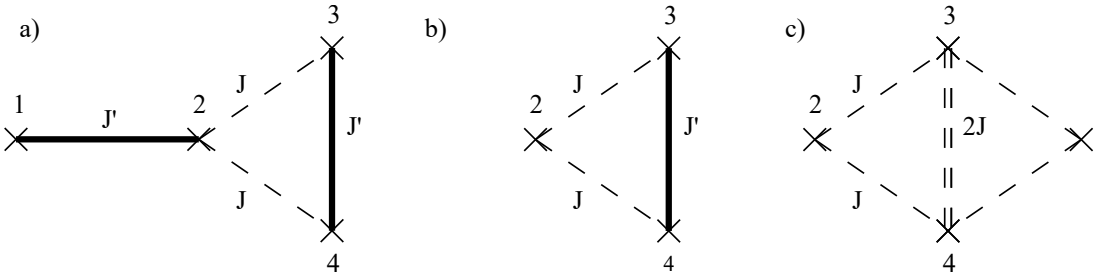

Figure 2.5: a) A pair of dimers in the Shastry-Sutherland lattice with corresponding inter-dimer couplings. b) The relevant couplings for the inter-dimer exchange c) Breaking up the dimer bonds into triangles with equal couplings along the edges. Adapted from Ref.[46].

Further,

$$\begin{aligned}
(S_3^z + S_4^z)\frac{|\uparrow\downarrow\rangle - |\downarrow\uparrow\rangle}{\sqrt{2}} &= 0, \\
(S_3^+ + S_4^+)\frac{|\uparrow\downarrow\rangle - |\downarrow\uparrow\rangle}{\sqrt{2}} = \frac{0 - |\uparrow\uparrow\rangle + |\uparrow\uparrow\rangle - 0}{\sqrt{2}} &= 0, \\
(S_3^- + S_4^-)\frac{|\uparrow\downarrow\rangle - |\downarrow\uparrow\rangle}{\sqrt{2}} = \frac{|\downarrow\downarrow\rangle - 0 + 0 + |\downarrow\downarrow\rangle}{\sqrt{2}} &= 0, \\
\Rightarrow S_x|S_{3,4}\rangle = -S_x|S_{3,4}\rangle = 0,\ S_y|S_{3,4}\rangle = -S_y|S_{3,4}\rangle &= 0.
\end{aligned} \tag{2.13}$$

Consequently,

$$J\sum_\alpha S_2^\alpha|\sigma_2\rangle \otimes (S_3^\alpha + S_4^\alpha)|S_{3,4}\rangle = 0. \tag{2.14}$$

Now we have to show that this state minimizes the energy. If we look at the triangle made up by sites 2-4(Fig.2.5b), we can rewrite the Hamiltonian

$$\mathcal{H} = JS_2S_3 + JS_2S_4 + J'S_3S_4 = JS_2S_3 + JS_2S_4 + 2JS_3S_4 + (J' - 2J)S_3S_4 \tag{2.15}$$

For $J' > 2J$, the last term is always negative for antiparallel S_3, S_4. For now let $J' = 2J$. Then we can rewrite the Hamiltonian in terms of triangles(Fig.2.5c)[46]):

$$\mathcal{H} = \sum_\triangle J(S_iS_{i+1} + S_iS_{i+2} + S_{i+1}S_{i+2}) = \sum_\triangle \frac{J}{2}\left((S_i + S_{i+1} + S_{i+2})^2 - 3\cdot\frac{3}{4}\right). \tag{2.16}$$

For $S = 1/2$, this is minimized if $(S_i + S_{i+1} + S_{i+2}) = 1/2$ and we get $E_{min} = -\frac{3J}{2}$. The extra $(J' - 2J)S_{i+1}S_{i+2}$ term ensures that the singlet is located on the J'-bond. The product of singlets therefore is indeed the exact ground state of the SSM for $J' > 2J$. More advanced numerical work has shown that the ground state is exact up to $J/J' = 0.68$[16]. For $J/J' > 0.86$ the model is expected to host long range magnetic order [16]. What happens in-between has been hotly debated [13–31]. The most intriguing intermediate phase proposed is the so-called plaquette state [16, 18, 22]. Dimer singlets are destroyed to be replaced by singlets composed of *four* spins connected via the inter-dimer bonds J. Translational symmetry is broken and some or all of the dimer spin correlations become predominantly *ferromagnetic* (FM).

2.2.2 $SrCu_2(BO_3)_2$

The only known and much studied experimental realization of the Shastry-Sutherland model is $SrCu_2(BO_3)_2$, where $S = 1/2$ Cu^{2+} ions form J'-dimers via Cu-O-Cu superexchange pathways(Fig. 2.6a), which are connected through (BO_3) units (Fig. 2.6b) [33]. With a frustration ratio $J/J' \sim 0.6$ [32] it is reliably in the dimer phase, with a spin gap $\Delta = 3$ meV [33] in the excitation spectrum. We are incredibly lucky that in this material J/J' can be continuously tuned by hydrostatic pressure [34]. The frustration ratio increases steadily with pressure, eventually leading to a Néel ordered state above 30 kbar [35]. Moreover, already at $P_c \sim 18$ kbar the original dimer phase gives way to a new quantum paramagnet, presumed to be the plaquette state [34–38]. Thus, theoretical predictions for exotic phases of the SSM are put to the experimental test.

Using phonons to probe magnetic correlations In the present work we infer the strength of dimer spin correlations in $SrCu_2(BO_3)_2$ from their effect on certain optical phonons, which can be measured using Raman spectroscopy in a diamond-anvil pressure cell. The changes of the crystal lattice, which are induced by magnetic correlations are summed up under the label of magnetoelastic coupling. The leading magnetoelastic terms contributing to the ground

state energy of a Heisenberg system are[57]:

$$E_H = E_H^0 + \sum_{i,i'} \frac{\partial J_{ii'}}{\partial u_m} \mathbf{S_i} \cdot \mathbf{S_{i'}} u_m + \sum_{i,i'} \frac{\partial J_{ii'}}{\partial \eta_j} \mathbf{S_i} \cdot \mathbf{S_{i'}} \eta_j + \tag{2.17}$$

$$+ \sum_{i,i'} \frac{\partial^2 J_{ii'}}{\partial u_m \partial u_n} \mathbf{S_i} \cdot \mathbf{S_{i'}} u_m u_n + \sum_{i,i'} \frac{\partial^2 J_{ii'}}{\partial \eta_j \partial \eta_k} \mathbf{S_i} \cdot \mathbf{S_{i'}} \eta_j \eta_k + \sum_{i,i'} \frac{\partial^2 J_{ii'}}{\partial u_m \partial \eta_j} \mathbf{S_i} \cdot \mathbf{S_{i'}} u_m \eta_j + \ldots, \tag{2.18}$$

where u_m denotes ionic displacements from the reference structure and $\eta_j (j = 1, \ldots, 6)$ are the homogeneous strains in Voigt notation[58]. As can bee seen from equation 2.18, magnetic correlations can couple to both ionic displacements and lattice deformations. In $SrCu_2(BO_3)_2$, the onset of magnetic correlations is accompanied by structural distortions[59]. We will make use of magnetoelastic coupling to investigate magnetic correlations in $SrCu_2(BO_3)_2$ under pressure. The main idea is as follow. As has been established in other dimer systems, the development of pair spin correlations at low temperatures leads to a magnetic contribution to the rigidity of the corresponding bond [60–62]. This, in turn, gives rise to anomalous shifts of certain phonon frequencies at unusually low temperature. In complex structures it may be difficult to associate these shifts with any particular magnetic bonds [62]. For the highly symmetric structure of $SrCu_2(BO_3)_2$ though, the assignment of measured phonons to particular atomic motions is greatly simplified(cf. appendix A). At $\hbar\omega \sim$198 cm^{-1} (=24.5 meV) there is a specific optical excitation, the so-called pantograph mode, visualized in (Fig. 2.6b) [63].

It directly modulates the the intra-dimer coupling constant J', which is especially sensitive due to an almost 90° Cu-O-Cu bond angle[63]. At same time, its effect on J is expected to be negligible in comparison[59, 63]. The frequency of this phonon is related to the second derivative of the energy of the corresponding ionic displacement with respect to the displacement amplitude u: $\omega^2 \propto \partial^2 E / \partial u^2$. Each dimer's magnetic contribution is $J' \mathbf{S}_1 \mathbf{S}_2$. The frequency of the pantograph mode is much larger than the magnetic energy scale. This ensures an adiabatic coupling scenario where the spin correlations are unaffected by the phonon which is "too fast". Since the vibration mode spans the entire sample, the magnetic

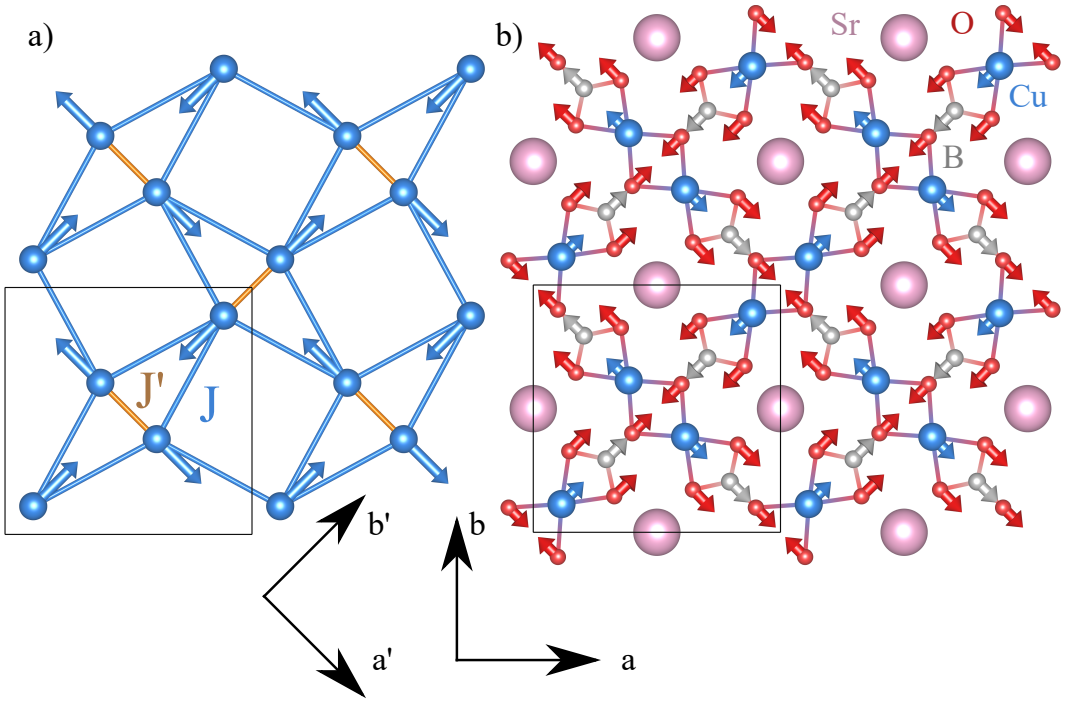

Figure 2.6: a) Lattice of orthogonal coupled dimers in $SrCu_2(BO_3)_2$ with intra-dimer interaction J' and inter-dimer interaction J. Copper atomic motions of the pantograph mode are indicated as arrows. b) Relative atomic displacements of the pantograph mode in a single layer of $SrCu_2(BO_3)_2$.

energy needs to be summed (averaged) over all dimers. With this in mind:

$$\delta\omega = \omega - \omega_0 \propto \omega^2 - \omega_0^2 \propto \frac{\partial^2 J'}{\partial u^2} \langle \mathbf{S}_1 \mathbf{S}_2 \rangle, \tag{2.19}$$

where ω_0 is the mode frequency in the absence of any magnetic correlations and it is assumed that $|\omega - \omega_0| \ll \omega_0$. The anomalous magnetic frequency shift of the pantograph mode is thus proportional to the dimer spin correlator. This also follows from the calculation of the corresponding spin-phonon coupling constant [64] that assumes a particular power-law u-dependence of J [65].

Crystal Growth Single-phase powders of $SrCu_2(BO_3)_2$ were synthesized by using the solid-state reaction method. Stoichiometric amounts of commercially available precursors CuO, $Sr(NO_3)_2$ and B_2O_3 from Sigma-Aldrich were ground

in an agate mortar. The mixture was heated up to 1000°C at a gas flow rate of 10 cc/min of 99.99% O_2 in a cubic Muffle furnace for 96 hrs with several intermediate grindings. The prepared powders were compacted into rods 5.0 mm in diameter and 100 mm long in a hydraulic isostatic press at 70 MPa for 20 minutes. The rods were sintered at 1150°C for 72 hrs in a Muffle furnace. Single crystals were grown by the flux optical floating-zone method. Crystals were grown at 0.5 MPa 99.99% oxygen pressure. $LiBO_2$ was used as a flux.

Structural motifs $SrCu_2(BO_3)_2$ crystallizes in the space group $I\bar{4}2m$ (No.121). The lattice parameters are a = 8.995(l) $\mathring{A}$ and c = 6.649(l) $\mathring{A}$, and there are four formula units per unit cell[59, 66]. Layers of orthogonal Cu^{2+} dimers —connected through $(BO_3)^{-3}$-units in the ab-plane —are separated along the c-direction by Sr^{2+} counter-ions. The dimer bonds are formed through Cu-O-Cu bonds with bridging angle 85.7° [59].

2.3 Frustrated square lattice — spin-nematic order?

Another possibility to frustrate the square lattice Heisenberg model is to introduce next-nearest-neighbor couplings. A case in point is the Heisenberg ferromagnet on a square lattice frustrated by antiferromagnetic (AF) next-nearest neighbor coupling. The classical model is either a collinear ferromagnet(FM) or a "columnar" AF (CAF) structure.

Consider the classical ground state energies of the two situations depicted in Fig.2.7. Equating these energies, we find that there is a transition between the two ground states at a critical value $\frac{J_2}{J_1} = -0.5$. These classical phase transitions are good starting points to look for new quantum phases. Indeed, for the $S = 1/2$ quantum model, a so-called spin-nematic phase with no dipolar magnetic order but spontaneously anisotropic spin fluctuations is predicted near the classical phase boundary[39–41]. Close to the saturation field, a nematic phase is supported for all $J_2/J_1 < -0.4$, as long as the material is very two-dimensional[42, 43]. The transition from the CAF phase to spin-nematic order

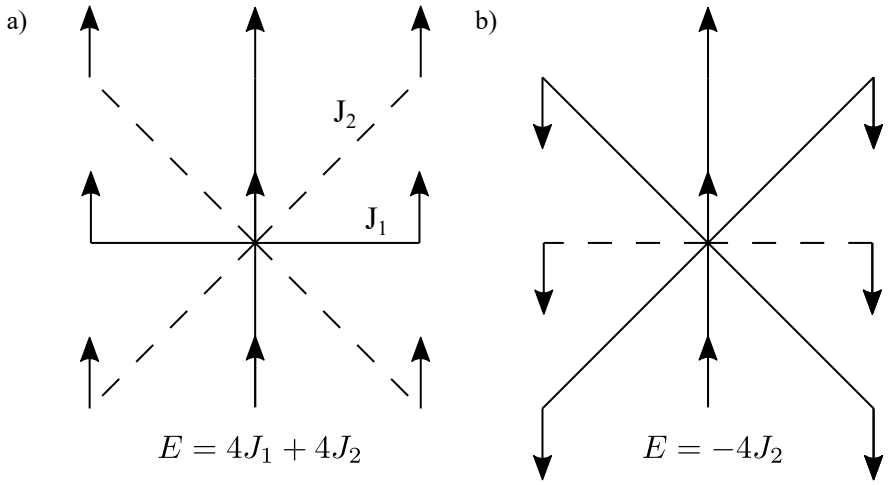

Figure 2.7: Sketch of the classical ground states and their respective energies for the frustrated square lattice with ferromagnetic nearest neighbor and antiferromagnetic next-nearest neighbor couplings for ferromagnetic(a) and columnar antiferromagnetic(b) order.

is expected to be first order, while the transition from a partially polarized paramagnetic phase to the spin-nematic phase is thought to be second order[67].

2.3.1 $Pb_2VO(PO_4)_2$

There are very few known potential experimental realizations of the ferro-antiferromagnet square lattice model. Most promising compounds belong to the family of layered vanadophosphates[44]. The most thoroughly studied compound is $Pb_2VO(PO_4)_2$, which has a magnetically ordered CAF structure[68, 69]. The exchange constants $J_1 = -0.52$ meV and $J_2 = 0.84$ meV were first estimated from magnetic susceptibility data[70]. These values are reasonably consistent with the frustration ratio deduced from quasielastic diffuse magnetic neutron scattering assuming a perfect square lattice model[69]: $J_2/J_1 \sim -2.4$. $Pb_2VO(PO_4)_2$ was also probed by Q-band electron spin resonance (ESR) [71], NMR [72] and magnetometry as well as specific heat [73] experiments on small single crystal samples. These experiments provided evidence for substantial ferro-antiferro frustration in this compound, while still putting it clearly in the classical CAF phse.

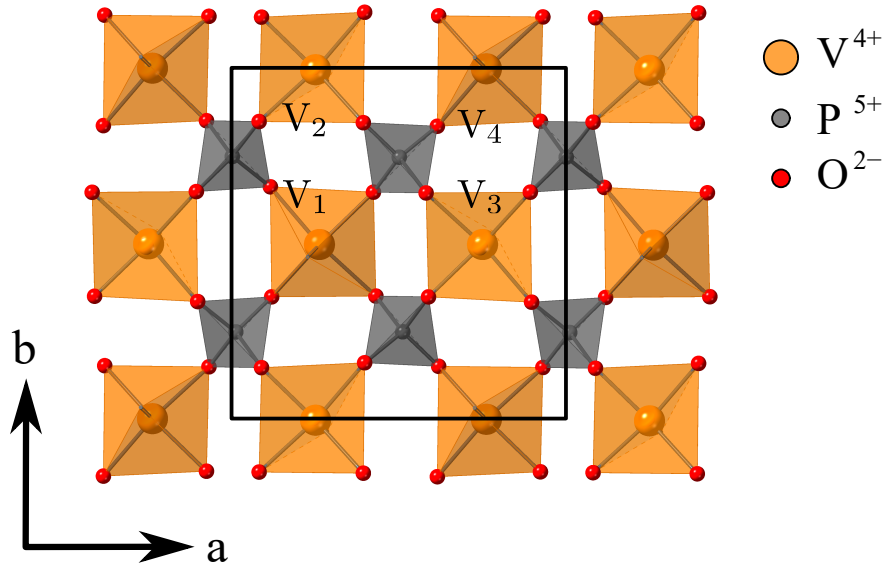

Figure 2.8: A single vanadophosphate layer in the crystal structure of $Pb_2VO(PO_4)_2$ showing the crystallographic unit cell and the four distinct V^{4+} ions that it contains.

Structural motifs $Pb_2VO(PO_4)_2$ crystallizes in space group $P12_1/a1$ (No.14) with lattice parameters a=8.747(4), b=9.016(5), c=9.863(9) Å, β=100.96(4)°[74]. Each unit cell contains four formula units. The crystal structure features layers of VO_5 pyramids connected through PO_4 tetrahedra in the (*ab*)-plane (Fig. 2.8). The V-layers are separated by phosphate tetrahedra and lead ions (Fig. 2.9). As can be seen in Fig.2.9 the layers are slightly buckled. Within each layer, symmetry allows for three distinct nearest neighbor and two next-nearest neighbor interactions. The exchange paths for nearest neighbor ferromagnetic interactions as well as next-nearest neighbor antiferromagnetic exchanges both run through two bridging oxygen atoms. The individual V-O-O bridging angles along the ferromagnetic and antiferromagnetic exchange paths are in the ranges of 100 to 120 degrees and 160 to 180 degrees respectively[74].

Crystal Growth Single crystals of $Pb_2VO(PO_4)_2$ were grown by the Bridgman technique. Powders of $Pb_2(VO)(PO_4)_2$ were synthesized in a Ar flowed Muffle furnace using stoichiometric amounts of high-purity commercially available pre-

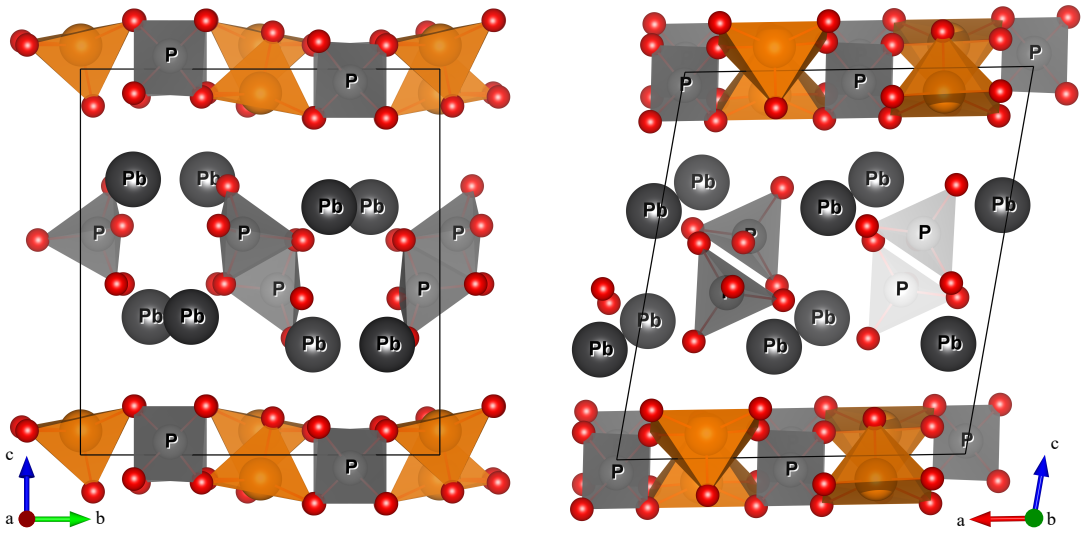

Figure 2.9: Crystal structure of $Pb_2VO(PO_4)_2$ viewed (a) along the crystallographic a-axis, (b) along the crystallographic b-axis. Vanadium atoms are orange, lead atoms dark grey, phosphorous atoms are light grey and oxygen atoms red.

cursors of PbO(99.999%), $NH_4H_2PO_4$(99.999%), V_2O_3(99.99%) and V_2O_5(99.99%)(Sigma-Aldrich). The family of vanadylphosphate compounds, including $Pb_2VO(PO_4)_2$ melt incongruently. Therefore, they can only be grown by the flux method. The molten compound in the crucible needs holding for more than 24 h, to ensure homogenous melting. Centimeter-sized single crystals of $Pb_2(VO)(PO_4)_2$ were grown in a tapered quartz tube, using the self-flux Bridgman method at 1000°C using a modified vertical tube muffle furnace. The growth speed was controlled between 2mm/hr and 4mm/hr. During the growing period, care was taken to prevent ingress of oxygen though the enclosure of the quartz tube. A small piece of metallic tantalum was used as an oxygen scavenger. The single crystal used for neutron diffraction had a mosaic spread of 0.6 ° and weighed 23 mg (Fig.2.10), the crystal used in the inelastic neutron scattering experiments weighed 1.5 g and had a mosaic of 0.6° (Fig.2.11). The single crystal used for magnetization measurements was rod-shaped with dimensions $3 \times 1 \times 0.5$ mm^3. The sample orientation and a high resolution polarized-light micrograph of the sample surface

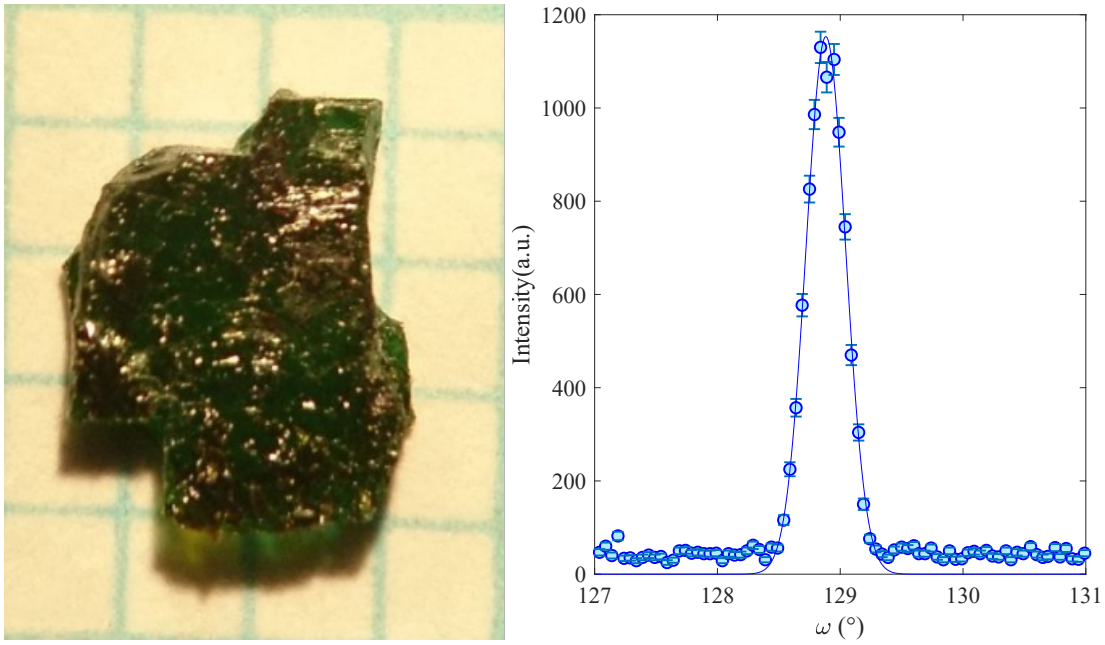

Figure 2.10: Left: Single crystal of $Pb_2VO(PO_4)_2$ used for neutron diffraction experiments. Right: Rocking scan of (2 0 0) from $Pb_2VO(PO_4)_2$ crystal used for neutron diffraction measured on CEA-CRG D23.

are shown in figure 2.12. No indication of crystal domains or sample twinning was found.

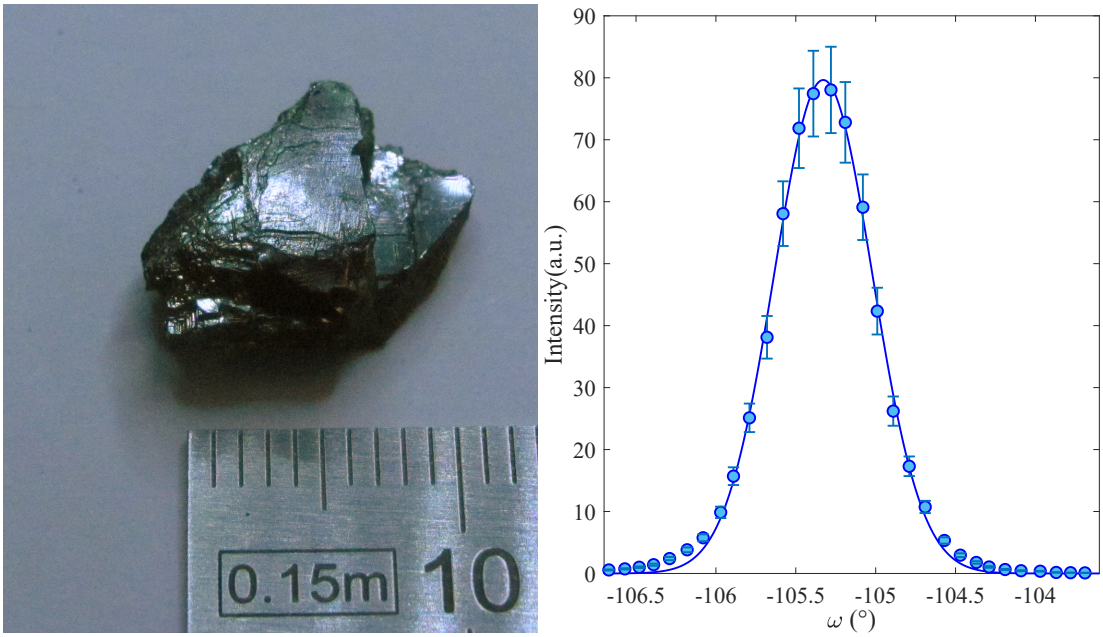

Figure 2.11: Left: Large single crystal of $Pb_2VO(PO_4)_2$ used for inelastic neutron scattering experiments. Right: Rocking scan of (0 2 0) nuclear reflection from $Pb_2VO(PO_4)_2$ crystal used for neutron spectroscopy, measured on IN3.

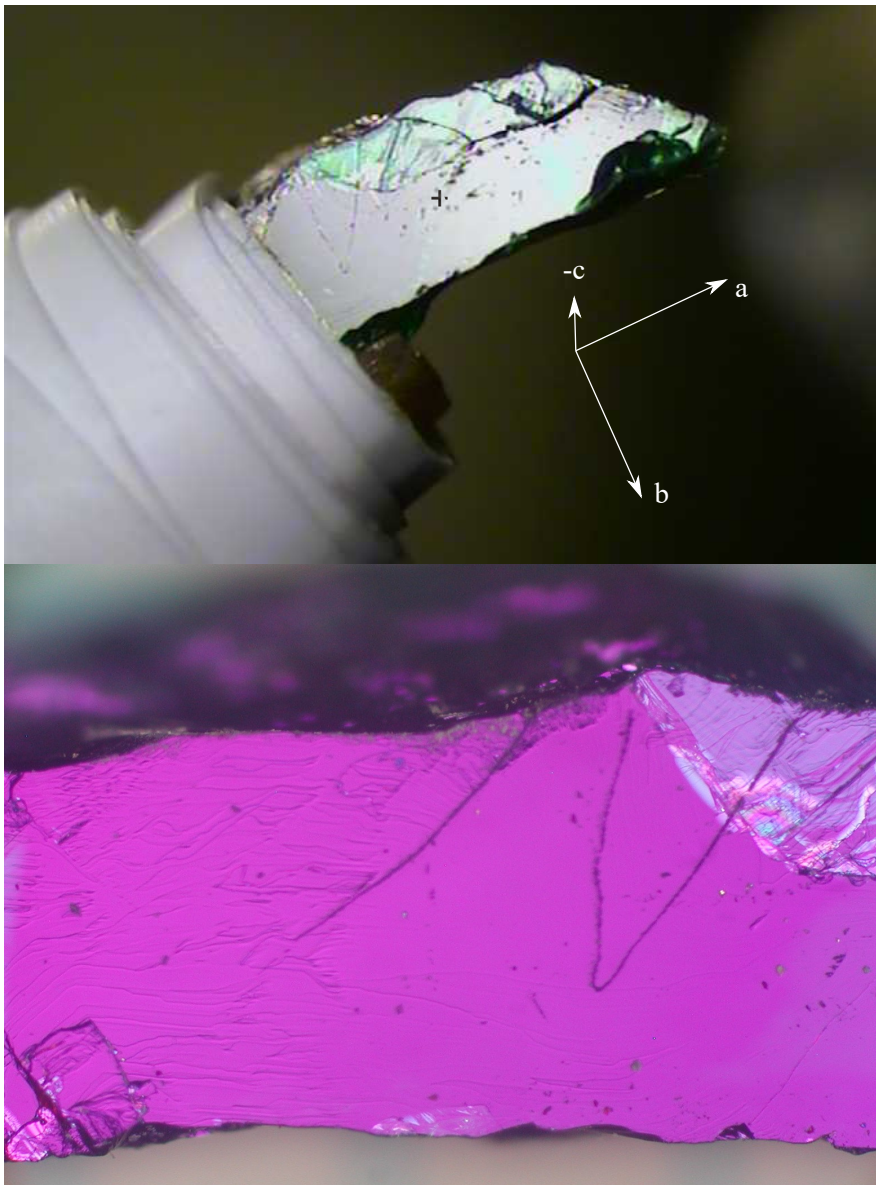

Figure 2.12: Top: Single crystal of $Pb_2VO(PO_4)_2$ used for magnetization experiments. Bottom: High resolution micrograph of the sample surface of the $Pb_2VO(PO_4)_2$ crystal used for magnetization measurements.

Chapter 3

Experimental techniques

In this chapter, the most important experimental techniques used in this work are introduced. The basic measurement principles and the effectively measured quantities of the performed experiments are presented.

3.1 Sample characterization and alignment

Samples for Raman scattering were oriented in a Bruker D8 x-ray diffractometer with a Molybdenum anode($\lambda = 0.71073$ Å). To avoid sample pollution due to adhesives, MiTeGen MicroGripper™ sample mounts of various sizes were used. For $(C_4H_{12}N_2)Cu_2Cl_6$, cleaving of the crystals lead to the formation of copper chloride on the cleaved surface. Thus as-grown sample surfaces were necessary for the acquisition of high quality data.
For $SrCu_2(BO_3)_2$, the single crystal rod produced through the floating-zone technique was crushed into small pieces. High quality samples were selected in a polarized microscope and then oriented on the x-ray diffractometer. All measurements under pressure were performed on the single crystal shown in figure 3.1.

Single crystals of $Pb_2VO(PO_4)_2$ were oriented on the x-ray diffractometer and further characterized by magnetization measurements. The crystals were aligned on the sample holders for neutron scattering experiments on the neutron instruments given in table 3.1.

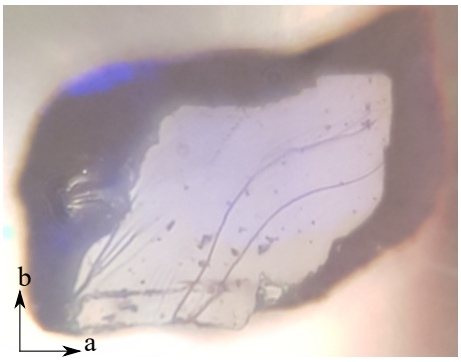

Figure 3.1: The single crystal of $SrCu_2(BO_3)_2$ used for all the Raman spectroscopy measurements under pressure.

Experiment	Alignment station
Neutron diffraction on CEA-CRG D23	OrientExpress[75]
Inelastic neutron scattering on MACS	PHADES
Inelastic neutron scattering on IN12	IN3

Table 3.1: Neutron scattering instruments and corresponding alignment stations used in this work.

3.2 Raman Spectroscopy

3.2.1 Why is Raman scattering useful for magnetism?

In recent years, there has been a growing interest in pressure-induced phase transitions occuring in quantum magnets[6, 7, 9, 11, 76, 77]. While — within some limits — high-pressure experiments are possible to perform with neutron scattering, they remain very challenging to this day. In particular, spectroscopic studies are typically limited to pressures below ∼20 kbar[78].

In contrast, Raman scattering is ideally suited for high-pressure experiments. Diamond anvil cells allow to reach pressures far beyond the capabilities of the most advanced high-pressure sample environment available for inelastic neutron scattering. In addition, high-quality IIa diamonds, which have practically zero background at small energy transfers, have recently become affordable. This allows to study the pressure-dependence of magnetic excitations in quantum

magnets at energies as low as 1 meV. In addition to the challenges to reach high pressures for neutron scattering experiments, the precise quantification of said pressure still constitutes a major challenge.[79] Thanks to the long tradition of high pressure research with Raman spectroscopy, a selection of pressure markers have been accurately calibrated[80, 81]. The most common pressure gauge is fluorescence from the ruby R1 line, which is what is used in these studies as well. The main shortcoming of Raman scattering is that — because visible light carries only very small momentum — only excitations at $\mathbf{Q} \approx 0$ can be probed. Furthermore, temperatures below 3 K are very difficult to achieve because of sample heating by the laser an necessary optical access windows. A major disadvantage of neutron scattering is the need for very large samples. In contrast, Raman scattering can be performed on very small samples. Typical sample dimensions for high pressure experiments are of order 0.2-0.5 mm.

3.2.2 Light Scattering Fundamentals

When a sample is irradiated with light, there are many processes which can occur. Most incoming photons are scattered elastically, which is called Rayleigh scattering. There is however the possibility that the photons create internal excitations and scatter inelastically. It is these processes that are studied in Raman spectroscopy. The energy difference between incoming and outgoing light is analyzed to learn about the nature of internal excitations of the studied sample.

A Raman scattering setup therefore consists of a narrow-frequency source of light,in our case a laser source is used, beam optics to direct the light onto the sample and collect the scattered light, a spectrometer and a photon detector to analyze the inelastically scattered light.

3.2.3 Macroscopic interpretation of Raman scattering

Electromagnetic waves have both electric and magnetic components. Surprisingly, Raman scattering from magnetic excitations does not occur primarily because of a direct coupling of light to magnetic moments. Instead, it is a result of of a coupling to the electric moments of the scattering medium. One may think of a medium as being made up by a collection of microscopic electric dipoles which can produce a finite macroscopic polarization. If no internal excitation is

created by the incoming light, they will always oscillate with the frequency of the incident electromagnetic wave and re-emit photons with the same frequency.

A normal mode of the scattering medium can however modify its susceptibility. The polarizability of the system may depend on whether the elementary oscillators are in the ground state or have been excited into a collective higher-energy state. Let ν be a characteristic variable of the excitation like the normal mode vector. The polarization $\mathbf{P}$ of the medium can be expanded in terms of the external electric field $\mathbf{E}_{in}$ [82]:

$$P^{\xi}(r) = \chi^{\xi\mu}(\omega_{in})\mathbf{E}^{\mu}_{in} + \frac{\partial\chi^{\xi\mu}}{\partial\nu}(\omega_{in}, -\omega)\nu(\omega)\mathbf{E}^{\mu}_{in} + \ldots, \tag{3.1}$$

where ω is the frequency of the internal excitation and χ is the first order susceptibility, which produces elastic scattering. Electromagnetic waves can also create an excitation in the scattering medium. In such a case, in equation 3.1, $\frac{\partial\chi}{\partial\nu}(\omega_{in}, -\omega)$ is replaced by $\frac{\partial\chi}{\partial\nu}(\omega_{in}, \omega)$. The scattering off a pre-existing excitation is called anti-Stokes scattering, while the creation of an excitation is called Stokes scattering. A schematic representation of the possible light scattering processes is given in figure 3.2. The question is now, which information about the elementary excitations of the crystal is obtained by Raman scattering.

For an isotropic insulator without magnetic ions, the radiation of light by Stokes and anti-Stokes polarizations can be derived from Maxwell's equations[83]:

$$(\nabla^2 + k^2_{sc})\mathbf{E}_{sc}(\mathbf{r}, \omega_{sc}) = -\frac{\omega^2_{sc}}{\epsilon_0 c^2}\mathbf{P}(\mathbf{r}, \omega_{sc}), \tag{3.2}$$

where $k_{sc} = \frac{n_{sc}\omega_{sc}}{c}$ and c is the velocity of light in vacuum. The solution for the scattered field is[83]

$$\mathbf{E}_{sc}(\mathbf{r}, \omega_{sc}) = \frac{\omega^2_{sc}}{4\pi\epsilon_0 c^2}\int_V d^3\mathbf{r}'\frac{\exp(ik_{sc}|\mathbf{r} - \mathbf{r}'|)}{|\mathbf{r} - \mathbf{r}'|}\mathbf{P}(\mathbf{r}', \omega_{sc}). \tag{3.3}$$

The final scattering cross section in the far-field limit is[83]

$$\frac{\mathrm{d}^2\sigma}{\mathrm{d}\Omega\mathrm{d}\omega_{sc}} = \frac{\omega_{in}\omega^3_{sc}n_{sc}V}{(4\pi\epsilon_0 c^2)^2 n_{in}|E_{in}|^2}\int \mathrm{d}^3(\mathbf{r_1} - \mathbf{r_2})\exp(i\mathbf{k_{sc}}\cdot(\mathbf{r_1} - \mathbf{r_2})) \tag{3.4}$$

$$\times \langle(\mathbf{e_{sc}}\cdot\mathbf{P}^*(\mathbf{r_1}, \omega_{sc}))(\mathbf{e_{sc}}\cdot\mathbf{P}(\mathbf{r_2}, \omega_{sc}))\rangle. \tag{3.5}$$

There are two things to notice here:

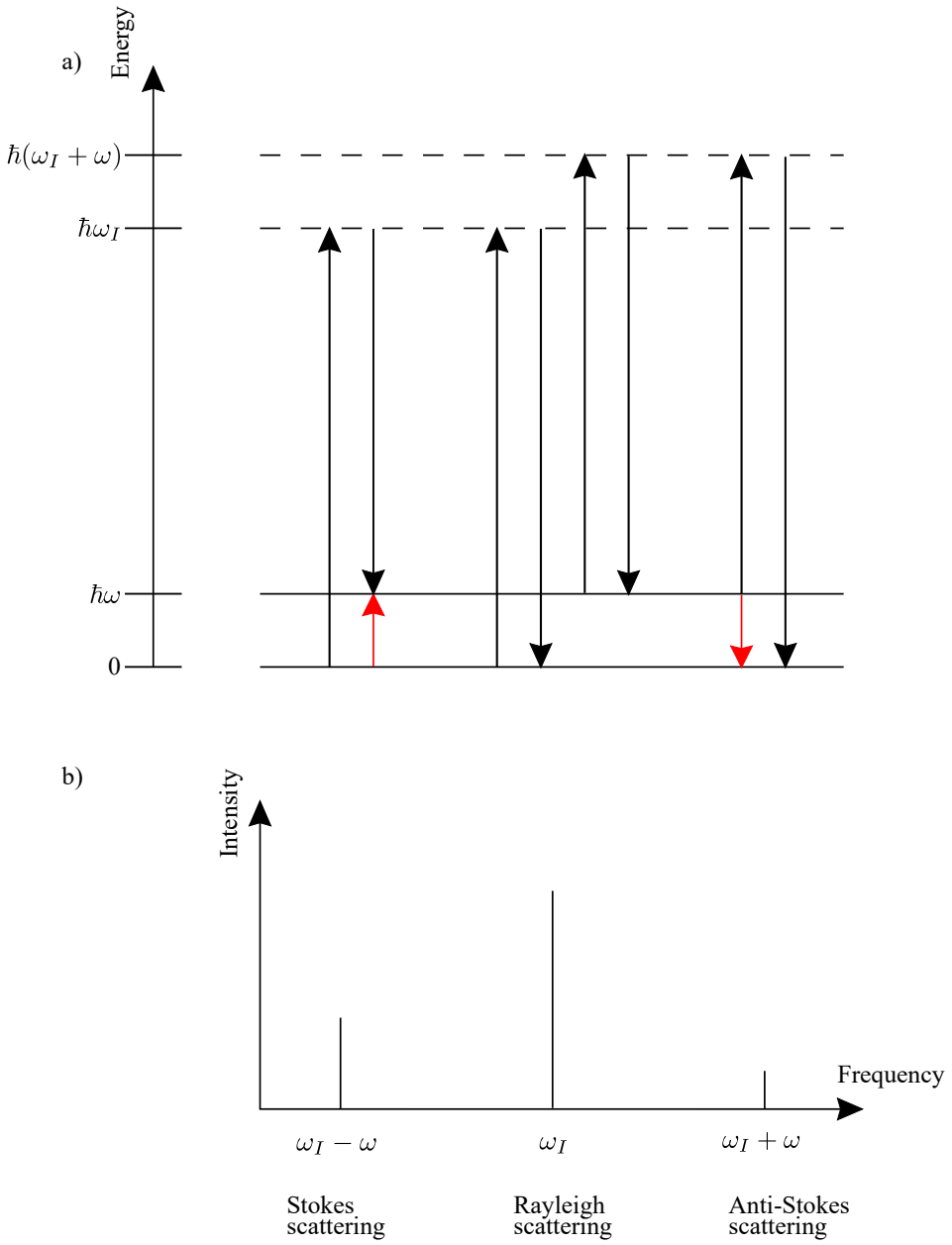

Figure 3.2: a)The three possible light scattering processes for a single remitted photon. b) Sketch of a Raman scattering spectrum. The inelastic peaks are typically several orders of magnitude smaller than the elastic peak. The relative intensity of Stokes and Anti-Stokes scattering depends on the population factor of the excited state.

1. Raman scattering yields information on the pair correlation function involving the fluctuating polarization.

2. The cross section has an approximate ω^4 dependence on the laser frequency.

So any excitation which leads to a fluctuating polarization produces a Raman signal. Raman scattering can be used to investigate optical phonons[84, 85], magnetic excitations[86] and electronic degrees of freedom[87]. In the following paragraph a short recapitulation of the Raman scattering mechanism for magnetic excitations is given, since this thesis' focus is primarily on magnetic insulators.

Magnetic Raman scattering An effective Hamiltonian for the interaction of light with the magnetic system can be written as[83]

$$\mathcal{H}_{int} = \sum_{\mathbf{r}} \sum_{\alpha,\beta} E^{\alpha}_{in} \chi^{\alpha\beta}(\mathbf{r}) E^{\beta}_{sc} \tag{3.6}$$

For magnetic materials with localized spins the susceptibility can be expanded in terms of spin operators[83, 88]:

$$\chi^{\alpha\beta}(\mathbf{r}) = \chi_0^{\alpha\beta}(\mathbf{r}) + \sum_{\mu} K_{\alpha\beta\mu}(\mathbf{r}) S^{\mu}_{\mathbf{r}} + \sum_{\mu,\nu} G_{\alpha\beta\mu\nu}(\mathbf{r}) S^{\mu}_{\mathbf{r}} S^{\nu}_{\mathbf{r}} + \sum_{\delta} \sum_{\mu,\nu} H_{\alpha\beta\mu\nu}(\mathbf{r},\delta) S^{\mu}_{\mathbf{r}} S^{\nu}_{\mathbf{r}+\delta} + \dots \tag{3.7}$$

The $K-$ and $G-$terms in equation 3.7 give rise to one-magnon scattering. In the simplest case of a ferromagnet in a cubic environment, the K-term takes the form $K \sum_i (\mathbf{E}_{in} \times \mathbf{E_{sc}}) \cdot \mathbf{S}_i$. The details of the term differ for less symmetric environments and other magnetic structures. However, the dominant one-magnon contribution is often still found in cross-polarization[86]. The G-term is typically not relevant in a backscattering geometry since it involves terms of the form $(E^z_{in}E^+_{sc} + E^+_{in}E^z_{sc})(S^+_{\mathbf{r}}S^z_{\mathbf{r}} + S^z_{\mathbf{r}}S^+_{\mathbf{r}})$ and $(E^z_{in}E^-_{sc} + E^z_{in}E^-_{out} + E^-_{in}E^z_{sc})(S^-_{\mathbf{r}}S^z_{\mathbf{r}} + S^z_{\mathbf{r}}S^-_{\mathbf{r}})$[83]. The $H-$term, which involves spin operators on different sites, could in principle also give rise to one-magnon scattering with terms $S^{\pm}_{\mathbf{r}}S^z_{\mathbf{r}+\delta}$ and $S^z_{\mathbf{r}}S^{\pm}_{\mathbf{r}+\delta}$[83, 88], however they would still not be important in a backscattering geometry. An important consequence of the $H-$term is that it gives rise to two-magnon scattering in which a pair of magnons is created and annihilated[83].

The interaction Hamiltonian for the $H-$term typically can be rewritten as[83]:

$$\mathcal{H} = \sum_{\mathbf{r},\delta} \sum_{\alpha,\beta,\mu,\nu} E_{in}^{\alpha} E_{sc}^{\beta} H_{\alpha\beta\mu\nu}(\mathbf{r},\delta) S_{\mathbf{r}}^{\mu} S_{\mathbf{r}+\delta}^{\nu} \tag{3.8}$$

Again, for a simple cubic ferromagnet it takes the form[83, 89]

$$\mathcal{H} = \sum_{\mathbf{r},\delta} ((H_1 - \frac{1}{3} H_3)\mathbf{E_{in}} \cdot \mathbf{E_{sc}} + H_3 (E_{in} \cdot \hat{\delta})(E_{out} \cdot \hat{\delta}) \mathbf{S_r} \cdot \mathbf{S_{r+\delta}}, \tag{3.9}$$

where H_1 and H_3 are magneto-optic coefficients and $\hat{\delta}$ is the unit vector in the direction of δ, which is the vector connecting the magnetic sites. The strongest contribution to two-magnon scattering can therefore be expected for incident and scattered light polarization along the bond directions.

3.2.4 Raman Spectrometer

A TriVista triple grating spectrometer with excitation laser central wavelengths 532 nm and 660 nm was used. The advantage of a triple grating spectrometer along with a reasonably narrow laser line(<1 MHz) is that a high stray light rejection is combined with a very good spectral resolution. The good stray light rejection allows for the measurement very close to the Rayleigh line, while the high spectral resolution permits the tracking of very small shifts of excitation energies. The experimental arrangement is shown in figure 3.3. The linearly polarized light is passed in turn through a beam expander BE, a polarization rotator $\lambda/2$ and an attenuator A before being directed into the sample through a focusing microscope M. The scattered light is collected by the microscope objective lens and focused onto the entrance slit S_1 of the spectrometer via a Bragg Notch filter(BNF), a polarization analyzer(PA) and a quarter-wave plate($\lambda/4$). The light is dispersed by grating G_1 before passing slit S_2, which limits the spectral range of the scattered light. Grating G_2 cancels the dispersive action of G_1 and recombines the remaining light while focusing it onto the third grating. The first two gratings together with the second slit therefore act as a bandpass filter. The light is finally dispersed again by G_3 and directed onto the liquid nitrogen cooled two-dimensional charge coupled device(CCD) detector.

Since the spectrometer is operated in backscattering geometry to allow the use of focusing optics, the z(xx)z, z(xy)z, z(yx)z and z(yy)z polarization geometries

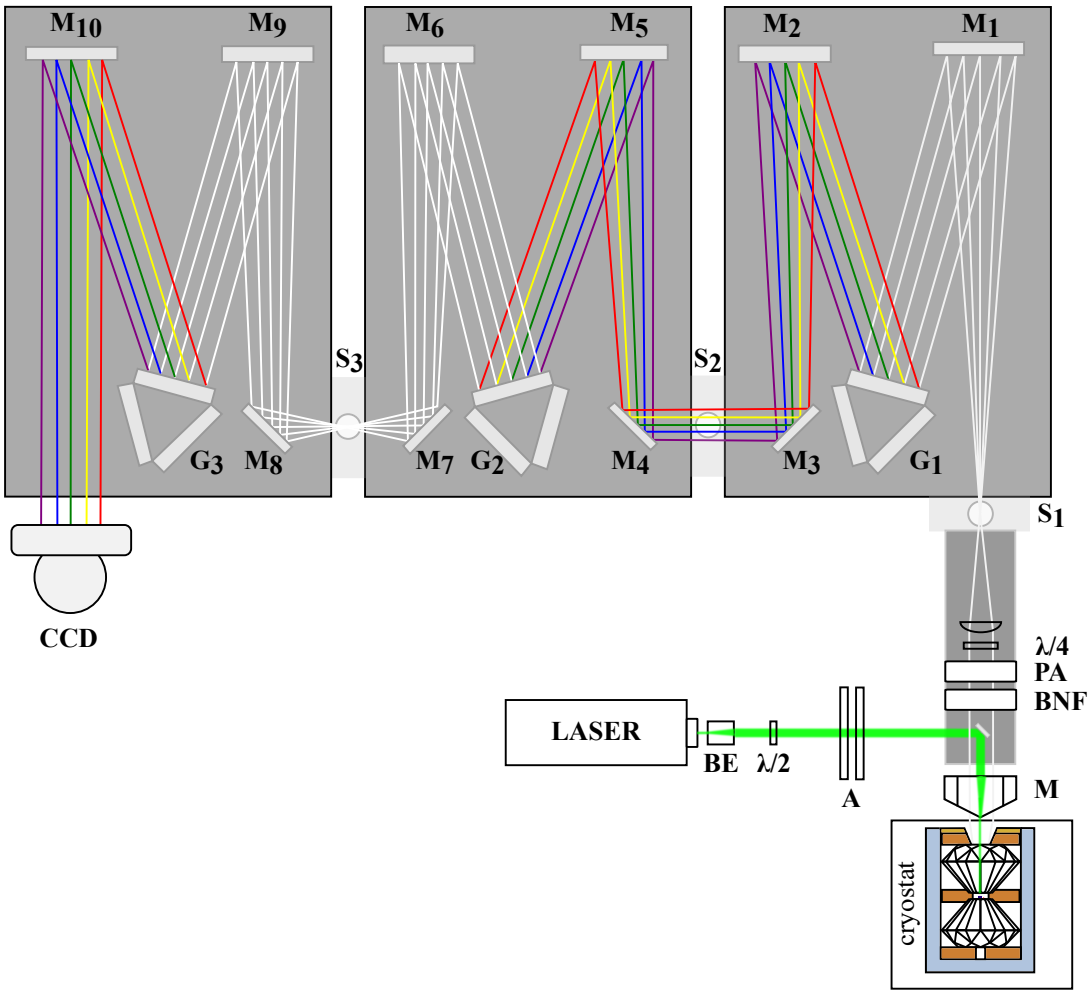

Figure 3.3: Left: Schematic of the light dispersion in triple subtractive mode to allow measurements very close to the Rayleigh line. Right: Schematic of the spectrometer in triple subtractive mode with the pressure cell in the sample chamber.

are accessible. Due to the excellent stray light rejection of the spectrometer, measurements with energy transfers as small as 1 meV were possible.

3.2.5 Raman scattering sample environment

Cryostat The pressure cell and sample were cooled with a liquid helium continuous-flow cryostat which rendered possible measurements in the temperature range from 2.6 K to room temperature. For ambient pressure measurements a simple planar cold finger was employed, with the sample in thermal contact with the cold finger through Apiezon N vacuum grease. This allowed for larger samples to be used, facilitating the orientation of the sample. For measurements with the pressure cell, a copper cold finger with a cavity to hold the pressure cell was used. To ensure good thermal contact Apiezon N vacuum grease was applied to the interface between the pressure cell and the cold finger. The pump used to ensure the circulation of liquid helium had a pumping speed of 35 m^3/h.

Pressure Cell The pressure cell setup used was an Opposing-Plates Diamond Anvil Cell with a diamond culet diameter in the range 1-1.5 mm with the basic design adapted from ref. [90]. The cell plates were manufactured from the nickel-copper alloy Monel-400. Copper-Beryllium gaskets with a hole diameter of 0.6 mm and a thickness of 0.7 mm were employed. The backing plates were also manufactured from Copper-Beryllium was used. The Copper-Beryllium alloy used for both gaskets and backing plates contained 2 % Beryllium.

Pressure Transmitting Media As a pressure medium, Daphne Oil 7373 and liquefied argon were used. For experiments on $(C_4H_{12}N_2)Cu_2Cl_6$, Daphne Oil proved sufficient as it remains liquid at room temperature up to a pressure of 22 kbar[91]. This in principle allows for the measurement in the pressure range up to approximately 20 kbar without the need of heating the pressure cell when applying pressure. Secondly, conditions are expected to remain largely hydrostatic in the experimentally accessible pressure range[92] and thirdly, Daphne oil 7373 has the advantage of being easy to handle at room temperature. For the investigation of $SrCu_2(BO_3)_2$ the liquefaction of argon was necessary due to the higher critical pressures. Furthermore, $SrCu_2(BO_3)_2$ is subject to strong

magnetoelastic coupling. As a consequence, the experimental conditions have to be designed such that any external strains are minimized. Liquid argon has the advantage of being relatively simple to liquefy while providing very good hydrostaticity up to several tens of kbar pressure[92, 93]. Due to the very weak signal of $SrCu_2(BO_3)_2$, the structured background produced by the argon pressure transmitting medium was of comparable intensity to the signal from the sample. Therefore the signal of the medium was independently measured to subtract from the sample spectra.

To ensure that the low-temperature effects observed in the experiments are not a consequence of pressure changes in the cell, we have closely monitored the temperature-dependence of the pressure inside the cell. As can be seen from Fig.3.4 a), the pressure changes below 40 K are marginal. Most of the pressure change due to thermal expansion and solidification of argon occurs between room temperature and 40 K as seen in Fig.3.4 b). For Daphne oil 7373, the pressure changes between room temperature and cryogenic temperatures are known to be significantly smaller[91].

Pressure reference The rubies used as a pressure gauge are doped such as to maximize the ruby R_1 intensity at ambient temperature. At room temperature the ruby R_1 fluorescence line was found at around 694.2 nm. At base temperature the line was located at 693.26 nm.

Pressure measurement The red-shift of the ruby R_1 line was used as a pressure scale. At room temperature the pressure was obtained according to the calibration curve given by Ref.[80]:

$$P[\mathrm{GPa}] = \frac{A}{B}\left(\left(\frac{\lambda}{\lambda_0}\right)^B - 1\right), \tag{3.10}$$

with constants A=1904 and B=7.715 At 4.5 K and below, the pressure was calculated through the relation[81]:

$$\mathrm{P[GPa]} = A_0 \ln\left(\frac{\lambda}{\lambda_0}\right), \tag{3.11}$$

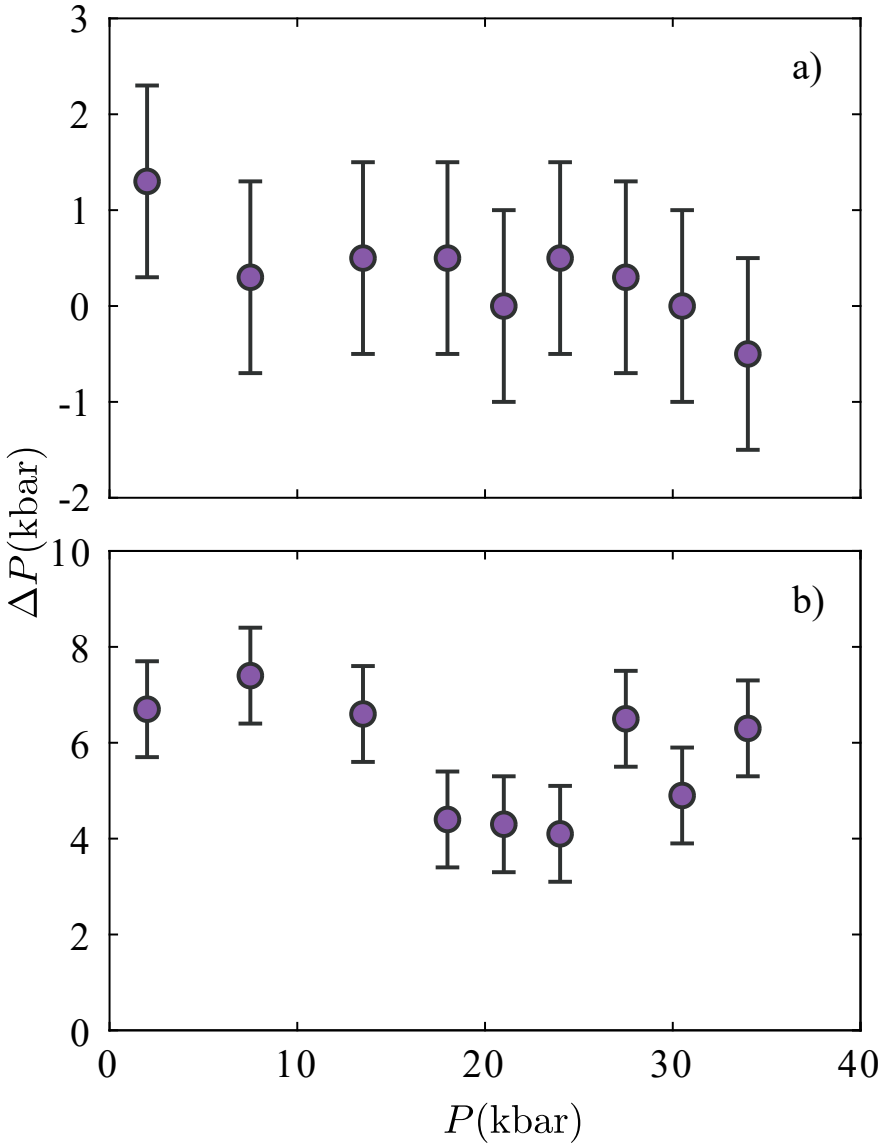

Figure 3.4: a) Measured pressure changes between 40K and base temperature. b) Measured pressure changes between room temperature and 40K.

with constant $A_0 = 1762$ GPa[81]. The peak positions and widths were extracted by fitting the Ruby R_1 and R_2 lines with Lorentzian peaks. The temperature-dependence of the ruby reference frequency was corrected for using the calibration given by Ref.[94].

Temperature measurement and control The temperature was measured by exploiting the temperature-dependence of the resistivity of the rhodium-iron alloy. This alloy has the advantage of the slope $\frac{dR}{dT}$ increasing very steeply below $\sim$ 15 K, making it extremely sensitive in the low-temperature-regime[95]. The thermometer was installed at the side of the cold finger. The temperature stability of the cryostat was better than 0.1 K at temperatures below $\sim$10 K and approximately 0.5 K above. The temperature in the cryostat was controlled through a needle valve at the helium transfer line and a heating coil. At elevated temperatures, the relative temperature stability was always $\lesssim$1 %.

3.3 Neutron Scattering

3.3.1 Why neutron scattering?

Neutrons are unique as a probe of matter because of three fundamental qualities which sets them apart from x-ray or electron scattering[96, 97]:

1. As neutrons have a rather large mass(m=1.675·10^{-27} kg), the energy of slow neutrons is comparable to the typical energies of elementary excitations in condensed matter systems. The energy transfers accessible through neutron scattering techniques are thus ideal to study dynamic properties. At the same time, the de-Broglie wavelength $\lambda = \frac{h}{mv}$ for typical neutron energies is similar to interatomic distances(few Å), making it a perfect fit to study structural properties of matter.

2. Because neutrons are electrically neutral, they interact only weakly with matter. Therefore, neutrons — in general — have a large penetration depth and allow to study the bulk properties of samples.

3. Neutrons carry a magnetic moment. This allows to determine materials' static and dynamic magnetic properties.

3.3.2 Basic principle of neutron scattering

The aim of a neutron scattering experiment is determining the probability for a neutron incident on the sample with wavevector k to be scattered to wavevector

k'. The relevant quantity of the scattering event is the momentum transfer

$$\hbar Q = \hbar(k - k'). \tag{3.12}$$

We call Q the scattering vector. The energy transferred in the scattering event is

$$\hbar\omega = \frac{\hbar^2}{2m}(k^2 - k'^2). \tag{3.13}$$

Together, these two equations ensure conservation of energy and momentum.

3.3.3 The neutron scattering cross section

The differential neutron scattering cross section corresponds to the ratio of neutrons scattered into the volume $\mathrm{d}\Omega\mathrm{d}\omega$ divided by the flux of the incident neutrons. Here, $\mathrm{d}\Omega$ denotes the solid angles and $\mathrm{d}\omega$, the range of energy transfers that make up the scattering volume. The starting point to find an expression for the cross section is Fermi's golden rule[97]:

$$\frac{\mathrm{d}^2\sigma}{\mathrm{d}\Omega\mathrm{d}\omega} = \left(\frac{m}{2\pi\hbar^2}\right)^2 \frac{k_f}{k_i} \sum_{\lambda_f,\sigma_f} \sum_{\lambda_i,\sigma_i} p_{\lambda_i} p_{\sigma_i} \left|\langle \mathbf{k_f}, \sigma_\mathbf{f}, \lambda_f | \hat{U} | \mathbf{k_i}, \sigma_\mathbf{i}, \lambda_i \rangle\right|^2 \cdot \delta(\hbar\omega + E_{\lambda_i} - E_{\lambda_f}), \tag{3.14}$$

where $|\lambda_i\rangle$ denotes the scatterer's initial state with energy E_{λ_i}, thermal population factor p_{λ_i} and $|\lambda_f\rangle$ designates the scatterer's final state. The spin states of the incoming and scattered neutrons are labelled with $\sigma_\mathbf{i}$ and $\sigma_\mathbf{f}$ and p_σ is the polarization probability. The interaction of the neutron with the scatterer is encoded in the operator $\hat{U}$ and depends on the specific scattering process. Finally, the delta function ensures energy conservation.

3.3.4 Nuclear scattering

Neutrons interact with nuclei through nuclear interactions which are very short-range. If the range of nuclear forces is negligible compared to the wavelength of neutrons, the interaction operator for the neutron-nucleus interaction can be approximated by the Fermi pseudopotential[96–98]:

$$\hat{U}(r) = \frac{2\pi\hbar^2}{m} \sum_j b_j \delta(r - \hat{R}_j), \tag{3.15}$$

where b_j is the scattering length of atom j. It is — in general — a complex number, with the real part corresponding to energy-independent scattering and the imaginary part corresponding to energy-dependent absorption[96, 97]. The values of b have been determined to great precision and are tabulated[99–101]. With the Fermi pseudopotential approximation, equation 3.14 takes the form:

$$\frac{\mathrm{d}^2\sigma}{\mathrm{d}\Omega\mathrm{d}\omega} = \frac{k_f}{k_i}\frac{1}{2\pi}\sum_{j,j'}\int_{-\infty}^{\infty}\langle e^{-i\mathbf{qR_{j'}(0)}}e^{-i\mathbf{qR_j(t)}}\rangle e^{-i\omega t}\mathrm{d}t, \tag{3.16}$$

where $\langle e^{-i\mathbf{qR_{j'}(0)}}e^{-i\mathbf{qR_j(t)}}\rangle = \sum_\lambda p_\lambda\langle\lambda|e^{-i\mathbf{qR_{j'}(0)}}e^{-i\mathbf{qR_j(t)}}|\lambda\rangle$. This can be rewritten in terms of correlation functions as [97]:

$$\frac{\mathrm{d}^2\sigma}{\mathrm{d}\Omega\mathrm{d}\omega} = N\frac{k_f}{k_i}\int_{-\infty}^{\infty}\mathrm{d}te^{-i\omega t}\int\mathrm{d}\mathbf{r}e^{i\mathbf{Qr}}\cdot\left(\langle b\rangle^2 G(\mathbf{r},t) + \left[\langle b^2\rangle - \langle b\rangle^2\right]G_s(r,t)\right), \tag{3.17}$$

where

$$G(\mathbf{r},t) = \frac{1}{N}\sum_{j,j'}\int\langle\delta\left(\mathbf{r'} - \hat{\mathbf{R}}_{\mathbf{j'}}(0)\right)\delta\left(\mathbf{r'} + \mathbf{r} - \hat{\mathbf{R}}_{\mathbf{j}}(t)\right)\rangle\mathrm{d}\mathbf{r'} \tag{3.18}$$

$$G_s(\mathbf{r},t) = \frac{1}{N}\sum_{j}\int\langle\delta\left(\mathbf{r'} - \hat{\mathbf{R}}_{\mathbf{j}}(\mathbf{0})\right)\delta\left(\mathbf{r'} + \mathbf{r} - \hat{\mathbf{R}}_{\mathbf{j}}(t)\right)\rangle\mathrm{d}\mathbf{r'}. \tag{3.19}$$

Here, $G(\mathbf{r},t)$ describes the probability of having a well-defined spatial and temporal correlation between the atom j' at position r and time $t = 0$ and the atom j at position $r' + r$ and time t. $G_s(\mathbf{r},t)$ is the self-correlation part, where $j' = j$. The two terms in equation 3.18 can be considered separately. They are called coherent and incoherent scattering cross sections[97]:

$$\left(\frac{\mathrm{d}^2\sigma}{\mathrm{d}\Omega\mathrm{d}\omega}\right)_{coh} = N\frac{k_f}{k_i}\langle b\rangle^2 S_{coh}(\mathbf{Q},\omega), \tag{3.20}$$

$$\left(\frac{\mathrm{d}^2\sigma}{\mathrm{d}\Omega\mathrm{d}\omega}\right)_{inc} = N\frac{k_f}{k_i}\left[\langle b^2\rangle - \langle b\rangle^2\right]S_{inc}(\mathbf{Q},\omega). \tag{3.21}$$

Any real system has different scattering lengths associated with different nuclei. The coherent scattering cross section is the scattering cross section an otherwise identical system where all atoms have the same scattering length $\langle b\rangle$ would have[96]. The incoherent part contains the terms needed to obtain the scattering

from the actual system which has various deviations of the scattering length from the mean value[96]. The simplest case is when the scattering system consists entirely of nuclei with nuclear spin $I = 0$. In such a case, the scattering is totally coherent and all the scattering lengths b are equal[96].

Elastic nuclear scattering In the case of elastic scattering $\hbar\omega = 0$, so $k_i = k_f$. In this situation equations 3.20 and 3.21 simplify to[96, 97]

$$\left(\frac{\mathrm{d}\sigma}{\mathrm{d}\Omega}\right)_{coh} = \langle b\rangle^2 \sum_{j\neq j'} e^{i\mathbf{Q}\cdot(\mathbf{R_{j'}}-\mathbf{R_j})}, \tag{3.22}$$

$$\left(\frac{\mathrm{d}\sigma}{\mathrm{d}\Omega}\right)_{inc} = (\langle b^2\rangle - \langle b\rangle^2) \sum_{j=j'} e^{i\mathbf{Q}\cdot(\mathbf{R_{j'}}-\mathbf{R_j})} = N(\langle b^2\rangle - \langle b\rangle^2). \tag{3.23}$$

The incoherent scattering therefore just produces a constant background. The coherent elastic neutron cross-section turns out to be[96, 97]

$$\frac{\mathrm{d}\sigma}{\mathrm{d}\Omega} = N_0 \frac{(2\pi)^3}{V} e^{-2W(\mathbf{Q})} \sum_{\tau} |S_\tau|^2 \delta(\mathbf{Q} - \tau), \tag{3.24}$$

where V is the unit cell volume, τ denotes a reciprocal lattice vector and $S_\tau = \sum_{\mathbf{d}} b_d e^{i\tau\cdot\mathbf{d}}$, with d the relative position of atoms in the unit cell, is the structure factor. $e^{-2W(\mathbf{Q})}$ is the so-called Debye-Waller factor. It contains information about the atomic displacements. For a cubic crystal of identical atoms $2W = \frac{1}{3}q^2\langle u^2\rangle$[96], where $\langle u^2\rangle$ is the mean square displacement of the atoms. So the information gathered from a elastic neutron scattering experiment is[97]:

- Size and symmetry of the unit cell from Bragg reflections' position and systematic absences.
- Location of atoms within the unit cell from observed Bragg peak intensities.
- Mean atomic displacements $\langle u^2\rangle$ from the Debye-Waller factor.

In this work, the first two are of primary interest. All measurements are performed at low temperatures and therefore the Debye-Waller factor correction is expected to be small.

3.3.5 Magnetic scattering

The primary difficulty in finding an expression for the magnetic neutron scattering cross-section is the calculation of the matrix elements in equation 3.14 for the interaction $\hat{U} = \hat{\mu} \cdot \mathbf{H}$, where $\hat{\mu}$ is the magnetic moment operator of the neutron and $\mathbf{H}$ is the local magnetic field generated by unpaired electrons[96, 97]. In the case of unpolarized neutrons, magnetic ions with fully localized magnetic moments and spin-only scattering, the master formula for magnetic scattering is obtained [96, 97]

$$\frac{\mathrm{d}^2\sigma}{\mathrm{d}\Omega \mathrm{d}\omega} = (\gamma r_0)^2 \frac{k_f}{k_i} F^2(\mathbf{Q}) e^{-2W(\mathbf{Q})} \sum_{\alpha,\beta} \left(\delta_{\alpha\beta} - \frac{Q_\alpha Q_\beta}{Q^2} \right) S^{\alpha\beta}(\mathbf{Q}, \omega), \tag{3.25}$$

where

$$S^{\alpha\beta}(\mathbf{Q}, \omega) = \frac{1}{2\pi\hbar} \sum_{j,j'} \int_{-\infty}^{\infty} e^{i\mathbf{Q}\cdot(\mathbf{R_j} - \mathbf{R_{j'}})} \langle \hat{S}_j^\alpha(0) \hat{S}_{j'}^\beta(t) \rangle e^{i\omega t} \mathrm{d}t \tag{3.26}$$

and $F^2(\mathbf{Q})$ is called the magnetic form factor. It is the Fourier transform of the normalized spin density of the magnetic ion[96]. The magnetic form factors for most ions have — in the dipole approximation — been tabulated in Ref. [101]. Therefore, in a neutron scattering experiment the scattered intensity is proportional to the Fourier transform of the spin pair correlation function in space and time[96, 97].

Magnetic structure determination Integrating over ω and replacing $\mathbf{l} = \mathbf{R}_j - \mathbf{R}_{j'}$ in equation 3.25, one obtains[96, 97]

$$\frac{\mathrm{d}\sigma}{\mathrm{d}\Omega} = (\gamma r_0)^2 e^{-2W(\mathbf{Q})} F^2(Q) \sum_{\alpha,\beta} \left(\delta_{\alpha\beta} - \frac{Q_\alpha Q_\beta}{Q^2} \right) \sum_l e^{i\mathbf{Q}\cdot\mathbf{l}} \langle \hat{S}_0^\alpha \rangle \langle \hat{S}_l^\beta \rangle. \tag{3.27}$$

The language to adequately describe magnetic structures is in terms of propagation vectors. The basic idea is to describe the ordered state as a distribution of magnetic moments, which has some periodicity and therefore can be Fourier-expanded[102]. The momentum transfer $\mathbf{Q}$ of a magnetic Bragg peak reflection can be decomposed into $\mathbf{Q} = \mathbf{H} + \mathbf{k}$, where $\mathbf{H}$ defines the Brillouin zone of the nuclear unit cell and $\mathbf{k}$ is the propagation vector of the magnetic superlattice. A magnetic structure is not limited to a single propagation vector and for complex

structures, multiple **k** may be necessary. Such a structure is called multi-**k**[102]. A further complication arises if there are more than one magnetic ion per unit cell. The propagation vector tells us about the translational symmetries of magnetic moments between unit cells but not how they are arranged inside the cell. This information is encoded in the relative intensities of the magnetic Bragg peaks[102]. In the case of multiple magnetic sites per unit cell, very often a magnetic structure with $\mathbf{k} = 0$ is observed. Depending on the space group of the crystal, this can correspond to a ferromagnetic, antiferromagnetic or even a non-collinear structure[102]. In such a situation, it is important to collect the intensities of many magnetic Bragg reflections to differentiate between these different configurations.

3.3.6 Neutron Instruments

Neutron scattering instruments can be classified into diffractometers to study elastic scattering and spectrometers for inelastic scattering. For inelastic scattering, the need to control the energy transfer leads to the requirement to quantitatively control the momentum of both incident and scattered neutrons. For diffraction it is sufficient to have control over the momentum transfer. A schematic representation of a triple axis spectrometer is shown in fig. 3.5a). The neutron energy of incident and scattered neutrons is selected by scattering the neutrons off pyrolytic graphite crystals. Data is typically gathered point-by-point by sampling reciprocal space through synchronized motions of the monochromator scattering angles, the sample rotation angle A3 and the scattering angle A4 whilst only detecting the scattered neutron with the energy fixed by the analyzer.

A single crystal diffractometer's basic design is similar, except that the scattered neutron energy is not analyzed and the detector is placed directly after the sample. Bragg peak intensities were measured by rotating A3 while keeping all other angles fixed (rocking scan).

3.3.7 Neutron Diffraction

The magnetic structure of $Pb_2VO(PO_4)_2$ was determined on the CEA-CRG D23 diffractometer at ILL using neutrons with the wavelength $\lambda = 2.35$ Å. The incoming neutron wavelength was selected using a pyrolytic graphite monochromator.

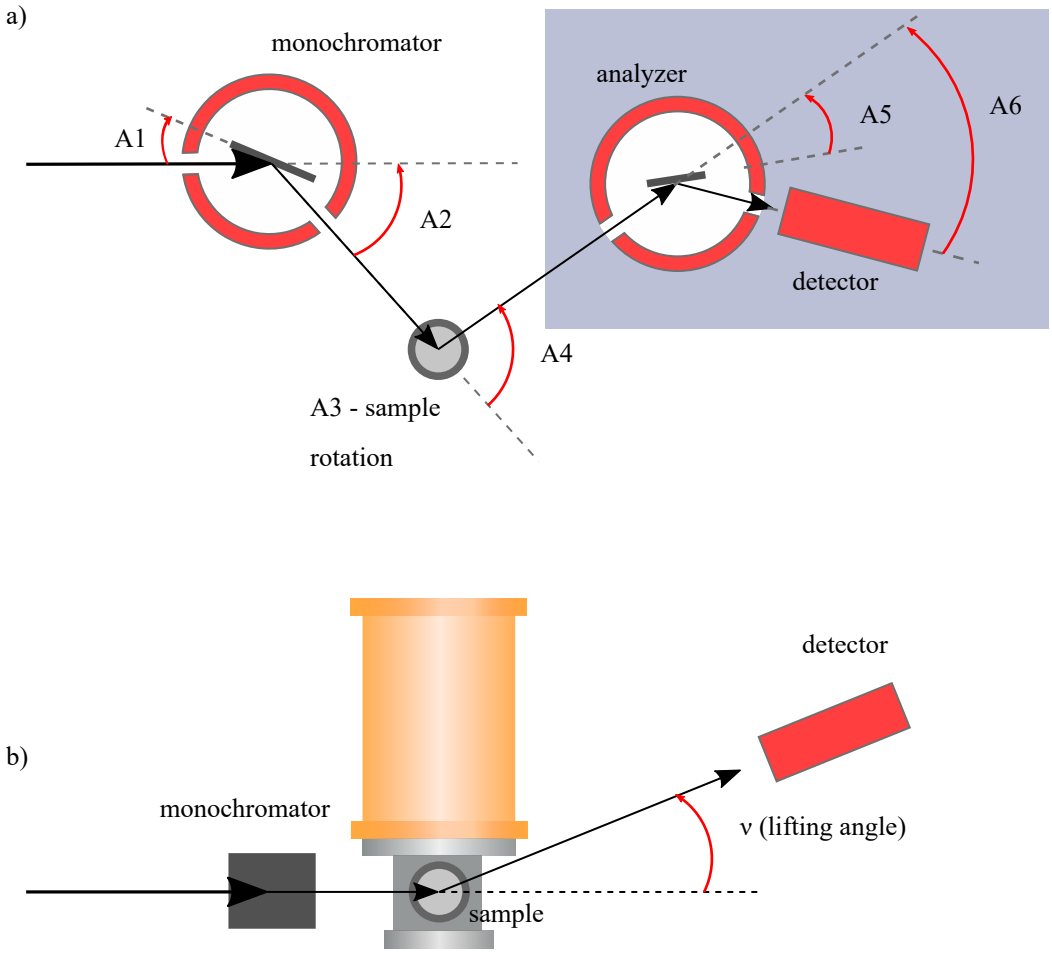

Figure 3.5: a) Schematic top view of a neutron 3-axis spectrometer. For a neutron diffractometer, the general layout is similar, except that the detector is placed directly after the sample without an energy-discriminating analyzer system(grey shaded). b) Schematic side view of a neutron diffractometer with a lifting counter detector, which can be moved on a circle around the sample position.

A pyrolytic graphite filter was used to suppress higher harmonics. Sample environment was a standard orange cryostat. Scattered neutrons were detected by a ^{3}He-gas detector tube. CEA-CRG D23 features a lifting counter detector which allows to reach Bragg peaks up to 29° away from the horizontal plane whilst using heavy sample environment such as orange cryostats or cryomagnets (Fig. 3.5b). This is particularly useful to determine magnetic structures in quantum magnets, where often very low temperatures are required. In systems with propagation vector $\mathbf{k} = 0$, it is imperative to collect a large number of magnetic Bragg peak intensities. In such situations, the ability to access out-of-plane Bragg peaks is essential to achieve a good refinement of the magnetic structure. In fact, magnetic ordering in $Pb_2VO(PO_4)_2$ corresponds to a $(0, 0, 0)$ propagation vector (recall that there are 4 magnetic atoms per unit cell). As a result, many magnetic Bragg reflections coincide with nuclear peaks. Magnetic reflections for which this was not the case were measured in usual rocking scans at 1.5 K counting about 45 s/point. For the remaining magnetic reflections we first measured the rocking curve of the underlying nuclear peak at $T = 5$ K $> T_N \sim 3.5$ K. Each scan was then analyzed using a Gaussian fit. Subsequently, the combined nuclear and magnetic contributions were measured at $T = 1.5$ K in short rocking scans near the top of the peak, counting about 60 s/point. To extract the magnetic contribution, these scans were fit using peak profiles of the same width as determined for the underlying nuclear peak above T_N.

The magnetic structure at T = 1.5 K was determined from an analysis of 11 measured magnetic reflections. These were normalized using the scale factor obtained from the least-square fitting of 22 nuclear Bragg peaks measured intensities (R-factor 4.2 %).

3.3.8 Inelastic neutron scattering

To enable the measurement of excitations, it is necessary to have quantitative control over the energy transfer between the incoming and scattered neutrons. A simple way to achieve this is to add an analyzer crystal between the sample and the detector(Fig. 3.5). This fixes the wavelength of neutrons which are scattered onto the detector and therefore the energy transfer. Because in such an instrument there are three axes of rotation(monochromator - sample - ana-

lyzer) such an instrument is called a 3-axis spectrometer. Spin wave excitations in $Pb_2VO(PO_4)_2$ were measured using the Multi-Angle Crystal Spectrometer (MACS) at NIST [103] and the IN12 3-axis instrument at ILL[104]. In both cases, the final neutron energy was fixed at E_f=3.7 meV. Higher-order beam contamination was suppressed by a cooled BeO filter on MACS and a cooled Be filter on IN12 after the sample. No collimators were used in either of the setups. Both experiments were performed at the base temperature of a dilution refrigerator below 0.1 K. The scattering planes were $(h, k, 0)$ and $(0, k, l)$ on MACS and IN12, respectively. The tabulated(MACS) and measured(IN12) energy resolution at the elastic position was correspondingly 0.17 meV and 0.12 meV full width at half maximum. On MACS the data were collected in constant-energy slices at 0.5, 1, 1.5, 1.75, 2 and 2.25 meV energy transfer. Each slice was taken by scanning the scattering angle in the typical range $-108°$ to $83°$ with $3°$ steps and the sample rotation angle in range $120°$ with $1°$ steps, while typically counting 60 s at each setting. IN12 data were taken in a series of constant-q scans centered along the $(0, k, 0)$, $(0, k, 2)$, $(0, 2.5, l)$ and $(0, 3, l)$ reciprocal-space rods with typical steps of 0.025 meV in energy transfer and counting about 120 s/point.

3.4 Vibrating Sample Magnetometry

A simple and reliable method to determine the magnetization of a material is so-called vibrating sample magnetometry[105, 106]. A small sample is placed at the center of a gradiometer pickup coil configuration. If this small sample with magnetization $\mathbf{M}$ is moved up and down inside the gradiometer, the change in flux through the pickup coils will induce a voltage:

$$V_{pickup} = -\frac{\mathrm{d}\Phi}{\mathrm{d}t} = -\frac{\mathrm{d}\Phi}{\mathrm{d}z}\frac{\mathrm{d}z}{\mathrm{d}t} = -AN\mu_0\frac{\mathrm{d}M_z}{dz}\frac{\mathrm{d}z}{\mathrm{d}t}, \tag{3.28}$$

where Φ is the flux through the coil, z is the vertical position of the sample, A is the cross-sectional area of the pickup coil with N windings and M_z is the vertical component of the sample magnetization. In this work, the commercial Quantum Design large bore Vibrating Sample Magnetometer option for the Physical Property Measurement System was used. The sample was attached with Apiezon N grease to a brass sample rod which is vertically oscillated inside the sample

chamber. The oscillation amplitude was 2 mm and the frequency $\nu = 40$ Hz [107]. The measured voltages are related to the sample magnetization of the sample by calibrating the setup with a Pd standard[107].

3.5 Magnetic torque

The first step in identifying a possible spin-nematic phase close to the saturation field is to determine the phase diagram close to the saturation field. Since in $Pb_2VO(PO_4)_2$ the saturation field is close to 21 T[108], such experiments have to be performed at a high-field facility. Indirect information on the size and direction of the magnetic moment at high fields is obtained by measuring the torque exerted by a homogeneous external magnetic field $\mathbf{H}$ on the sample with magnetization $\mathbf{M}$. The torque is then $\tau = \mathbf{M} \times \mu_0 \mathbf{H}$. The magnetic torque was measured by means of the capacitive-cantilever technique (e.g. Ref.[109, 110]). The sample is mounted on a thin BeCu-cantilever which flexes away from its equilibrium position due to the experienced torque. The flexing of the cantilever changes the capacitance of the capacitor made up by the base plate and the cantilever, which can be measured with very high precision.

The equation of motion of a simple setup (Fig.3.6) is

$$J\frac{\mathrm{d}^2\alpha}{\mathrm{d}t^2} = -k\alpha - D\frac{\mathrm{d}\alpha}{\mathrm{d}t} + \tau, \tag{3.29}$$

where D is the damping coefficient and k is the stiffness of the cantilever. J is the moment of inertia of the sample-cantilever assembly. The solution can be written as

$$\begin{aligned} \alpha(t) = \frac{\tau}{k} + A\exp(-\frac{D}{2J}t)\cos(\omega t), \\ \omega = \sqrt{\frac{k}{J} - \frac{D^2}{4I^2}}, \end{aligned} \tag{3.30}$$

where A is a constant. In the steady state the second term vanishes and the angle and the torque are proportional to each other with $\alpha = \tau/k$. The capacitance of a plate capacitor with inclined plates, as depicted in fig.3.6, is evaluated as

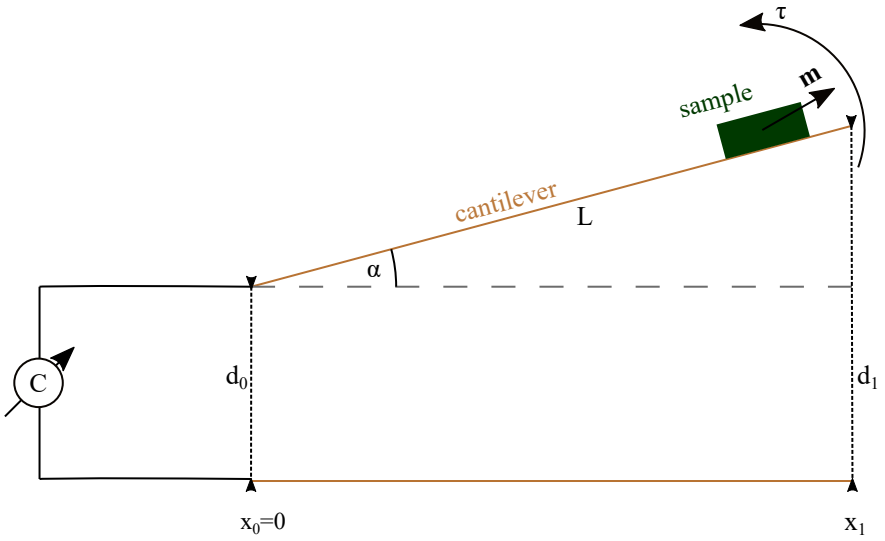

Figure 3.6: Sketch of a capacitive torque meter. For small flexing angles α, the capacitance change is proportional to the torque exerted on the sample(see text).

follows:

$$\tan\alpha = \frac{d_1 - d_0}{x_1} \tag{3.31}$$

$$\mathrm{d}C = \epsilon \frac{\mathrm{d}A}{\delta d} \tag{3.32}$$

$$\mathrm{d}A = y_1 \mathrm{d}x \tag{3.33}$$

$$\delta d = d_0 + x\tan\alpha \tag{3.34}$$

$$C = \int \mathrm{d}C = \int_0^{x_1} \epsilon \frac{y_1 \mathrm{d}x}{d_0 + x\tan\alpha} \tag{3.35}$$

$$= \epsilon y_1 \left[\cot\alpha \ln(d_0\cos\alpha + x\sin\alpha)\right]_0^{x_1} \tag{3.36}$$

$$= \epsilon y_1 \left(\frac{\ln(d_0\cos\alpha + x_1\sin\alpha)}{\tan\alpha} - \frac{\ln(d_0\cos\alpha)}{\tan\alpha}\right) \tag{3.37}$$

$$= \frac{\epsilon y_1}{\tan\alpha}\ln\left(1 + \frac{x_1}{d_0}\tan\alpha\right) = \frac{\epsilon y_1}{\tan\alpha}\ln\left(1 + \frac{x_1}{d_0}\frac{d_1 - d_0}{x_1}\right) \tag{3.38}$$

$$= \frac{\epsilon y_1}{\tan\alpha}\ln\left(\frac{d_1}{d_0}\right) = \frac{\epsilon y_1}{\tan\alpha}\ln\left(1 + \frac{L\sin\alpha}{d_0}\right). \tag{3.39}$$

Taylor expanding around $\alpha = 0$ gives

$$C = \epsilon y_1 \left(\frac{L}{d_0} - \frac{L^2 \alpha}{2 d_0^2} \right). \tag{3.40}$$

The change in capacitance is therefore directly proportional to the torque for small flexing angles.

Magnetic torque measurements were performed the Laboratoire National des Champs Magnéetiques Intenses in Grenoble (LNCMI-G). High magnetic fields were generated the by the resistive magnet M9 (36 T, 34 mm bore). The measurements were carried out in the cooling mixture of a $^3\mathrm{He} - {}^4\mathrm{He}$ dilution refrigerator. The measurements were performed with the external magnetic field aligned along the $b-$ and c^*-directions. Note that the b-direction is the easy axis of magnetic anisotropy[73] and that c^* is perpendicular to the a-b-plane with proposedly strong magnetic interactions. Magnetic torque data were fitted as suggested in ref. [111].

Chapter 4

$(C_4H_{12}N_2)Cu_2Cl_6$: Pressure-induced order in a quantum paramagnet

The results presented in this chapter are also published in
S. Bettler, G. Simutis, G. Perren, D. Blosser, S. Gvasaliya and A. Zheludev. "High pressure Raman study of the quantum magnet $(C_4H_{12}N_2)Cu_2Cl_6$.", Phys. Rev. B **96***, 174431 (2017) doi: 10.1103/PhysRevB.96.174431*

We probe the pressure-dependence of the two-magnon continuum in $(C_4H_{12}N_2)Cu_2Cl_6$ at $Q \approx 0$ with Raman spectroscopy. In addition, we investigate the effect of magnetic correlations on lattice excitations as a function of temperature and pressure. This provides additional information on the magnetic ground state and phase transitions.

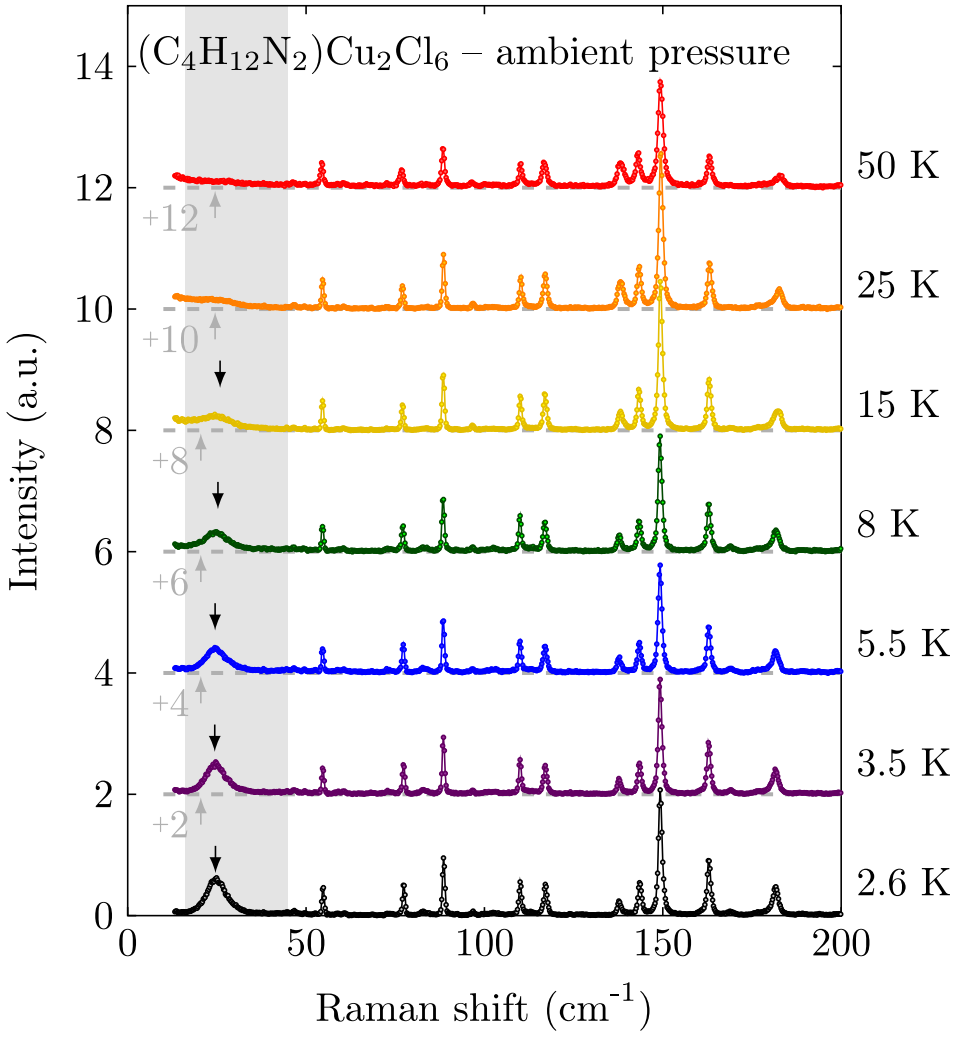

Figure 4.1: Measured temperature dependence of the Stokes Raman scattering spectra in $(C_4H_{12}N_2)Cu_2Cl_6$ in $\bar{Z}(XX)Z$ polarization at ambient pressure. Individual spectra are shown with incremental offsets for clarity. The arrows indicate the peak position of magnetic scattering.

4.1 Results

4.1.1 Ambient pressure

Magnetic scattering

At elevated temperatures, the measured Raman spectra are dominated by phonons. Below about 25 K, a broad continuum of excitations develops at low energies as shown in Fig. 4.1. This continuum is well separated from any phonons, which allows for a clean observation of its pressure-dependence without the necessity to subtract any lattice contributions. At $T = 2.6$ K the continuum is peaked at 24.6 cm^{-1} and has a full width at half maximum of 6 cm^{-1} as extracted from empirical Lorentzian fits. It is almost symmetric with a very slight tail extending towards higher energies. Its intensity increases with decreasing temperature, although its position remains largely unchanged. This is a strong indication that the low-energy feature is due to magnetic scattering [112–114].

Another confirmation comes from analyzing its energy range. Magnetic Raman scattering in quantum paramagnets is expected to originate primarily from two-magnon processes[86, 113]. A broad continuum is indicative of a substantial magnon bandwidth. For gapped quantum antiferromagnets such a continuum is confined in the energy range between 2Δ and twice the maximum magnon energy. For $(C_4H_{12}N_2)Cu_2Cl_6$, using the single magnon dispersion known from neutron studies[50], we can estimate the domain of this 2-magnon continuum to be between 16 cm^{-1} and 45 cm^{-1}. This range is indicated by the shading in Figs. 4.1 and 4.2, and indeed coincides with the domain of the observed continuum.

The magnetic nature of the continuum is also consistent with the observed polarization dependence of scattering. As shown in Fig. 4.2, the shape and position of the continuum is the same in all experimental configurations. However, its intensity is strongest in the $\bar{Z}(XX)Z$ geometry and much suppressed in the $\bar{Z}(YY)Z$ geometry. Thus, the signal is strongest for polarization along the two strongest magnetic bonds, similar to two-magnon scattering in other known dimer systems[61, 113].

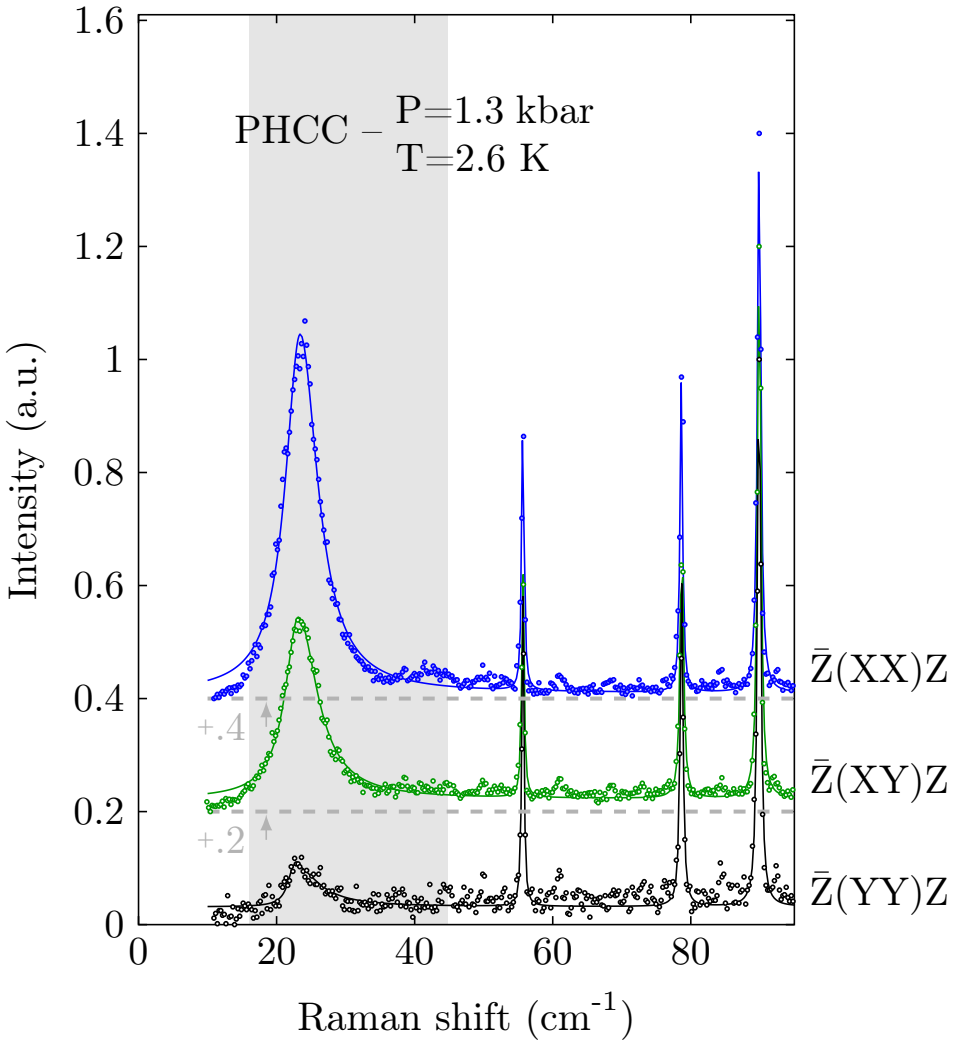

Figure 4.2: Symbols: Measured polarization dependence of the Stokes Raman scattering spectra in $(C_4H_{12}N_2)Cu_2Cl_6$ at base temperature at 1.3 kbar. The shaded area is as in Fig. 4.1. Lines are empirical Lorentzian fits. Individual spectra are shown with incremental offsets for clarity.

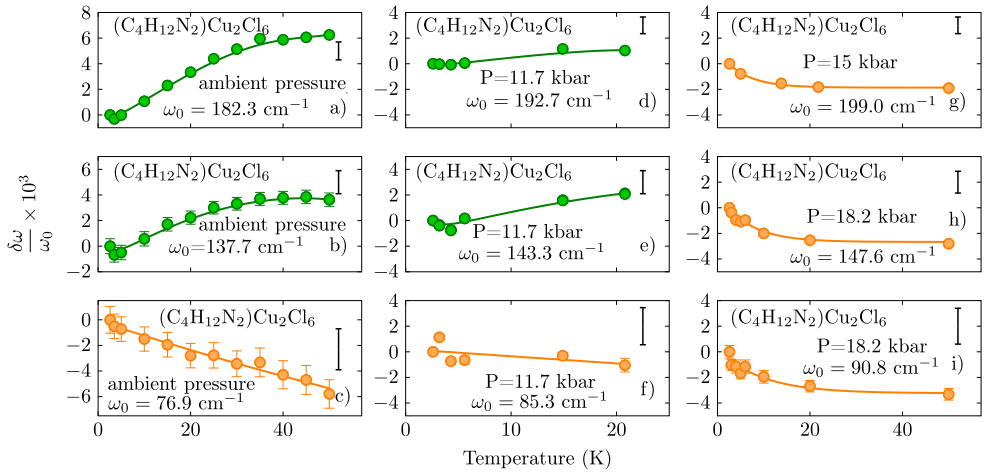

Figure 4.3: Relative frequency shifts of three representative anomalous phonons in $(C_4H_{12}N_2)Cu_2Cl_6$ against temperature at ambient pressure, just below the second transition and above the transition, as deduced from Lorentzian fits to the measured spectra. The detector bin sizes are shown in the upper right corners of each plot. Note that since each phonon peak is several detector bins wide, postulating its Lorentzian shape allows to determine the peak position with an accuracy greater than the bin size. Lines are guides to the eye.

Anomalous phonons

In the energy range 10-205 cm^{-1} that was studied in detail in our experiments, 11 strong phonon peaks were observed. Since the crystal is triclinic with space group $P\bar{1}$, point group C_i, all Raman active phonons have trivial A_g symmetry. From the measured spectra, the phonon frequencies were obtained in Lorentzian fits. As shown in Fig. 4.3, several of them exhibit anomalous temperature dependencies. Rather significant frequency shifts occur at *very low temperatures*, below 20 K. In this regime, two of the observed modes actually *harden* with increasing temperature.

In a bid to identify the eigenvectors of the anomalous phonons we performed density functional theory (DFT) *ab initio calculations* using the Quantum Espresso software package [115]. The non-local rVV10 functional [116] was used to incorporate Van der Waals and hydrogen bonding effects which are certainly important in this organomatallic compound. For all calculations the projector augmented

wave method was used. Pseudopotentials for the density functional suggested in Ref. [117] were generated using input parameters from the PSLibrary project (pslibrary.0.3.1)[118]. In all calculations the kinetic energy cutoff was 120 Ry and the charge density cutoff 600 Ry. Brillouin zone integration was performed using a 3x3x3 k-point grid.

For the 16 lowest-energy Raman-active modes the observed and calculated frequencies are listed in incremental order in the first two columns of Table 4.1. Additionally, measured and calculated phonon frequencies of a protonated sample are shown in the last two columms. The first 15 modes listed correspond to displacement patterns involving both the $[Cu_2Cl_6]^{2-}$ bitetrahedra as well as the organic ions. By contrast, the last mode listed in Table 4.1 – as well as all higher-energy modes – correspond to internal molecular modes of the piperazinium ion. Consequently this last mode shows a much larger shift in frequency upon H/D exchange.

A conclusive result of our DFT simulations is that the 10- to 205-cm^{-1} low-energy lines that were studied in detail all correspond to vibrations of the $[Cu_2Cl_6]^{2-}$ bitetrahedra with admixtures of low-energy vibrations of the piperazinium ions. This explains why almost all low-frequency vibrations are subject to substantial H/D isotope effect. At the same time it greatly complicates the vibrational landscape and makes the frequencies very sensitive to the difficult to account for Van-der-Waals interactions. Therefore, it appears impossible to unambiguously match the observed anomalous phonon lines to particular calculated ones. Few studies of $[Cu_2Cl_6]^{2-}$ vibrations in other materials have been reported to date. In a recent work, the authors also met considerable difficulties in assigning the low-frequency peaks to particular modes, as in our case[119].

4.1.2 Results under applied pressure

Magnetic excitations

As could be expected, magnetic Raman excitations in $(C_4H_{12}N_2)Cu_2Cl_6$ are strongly affected by hydrostatic pressure. As shown in Fig. 4.4, we observe a shift of the magnetic continuum to lower energies already at rather modest pressures. This is fully consistent with the previously observed softening of the spin gap [10]. Below $P_c \sim 4$ kbar, the spectral function retains its symmetric

Table 4.1: Comparison of calculated and measured phonon energies for $(C_4D_{12}N_2)Cu_2Cl_6$ and $(C_4H_{12}N_2)Cu_2Cl_6$ for the lowest vibrational modes in ascending order.

$(C_4D_{12}N_2)Cu_2Cl_6$		$(C_4H_{12}N_2)Cu_2Cl_6$	
Expt.(cm^{-1})	DFT(cm^{-1})	Expt.(cm^{-1})	DFT(cm^{-1})
54.4	49	57.0	52
76.9	74	77.1	75
88.3	76	91.5	78
96.4	85	103.9	88
109.8	93	112.5	99
116.7	105	124.6	113
137.7	117	139.4	120
143.2	126	149.5	130
149.0	137	152.8	140
162.7	148	164.8	151
182.3	160	184.7	160
206.1	181	207.0	184
278.2	258	278.3	258
290(2)	275	290(2)	275
305.3	302	304.7	303
319.9	305	406.1	387

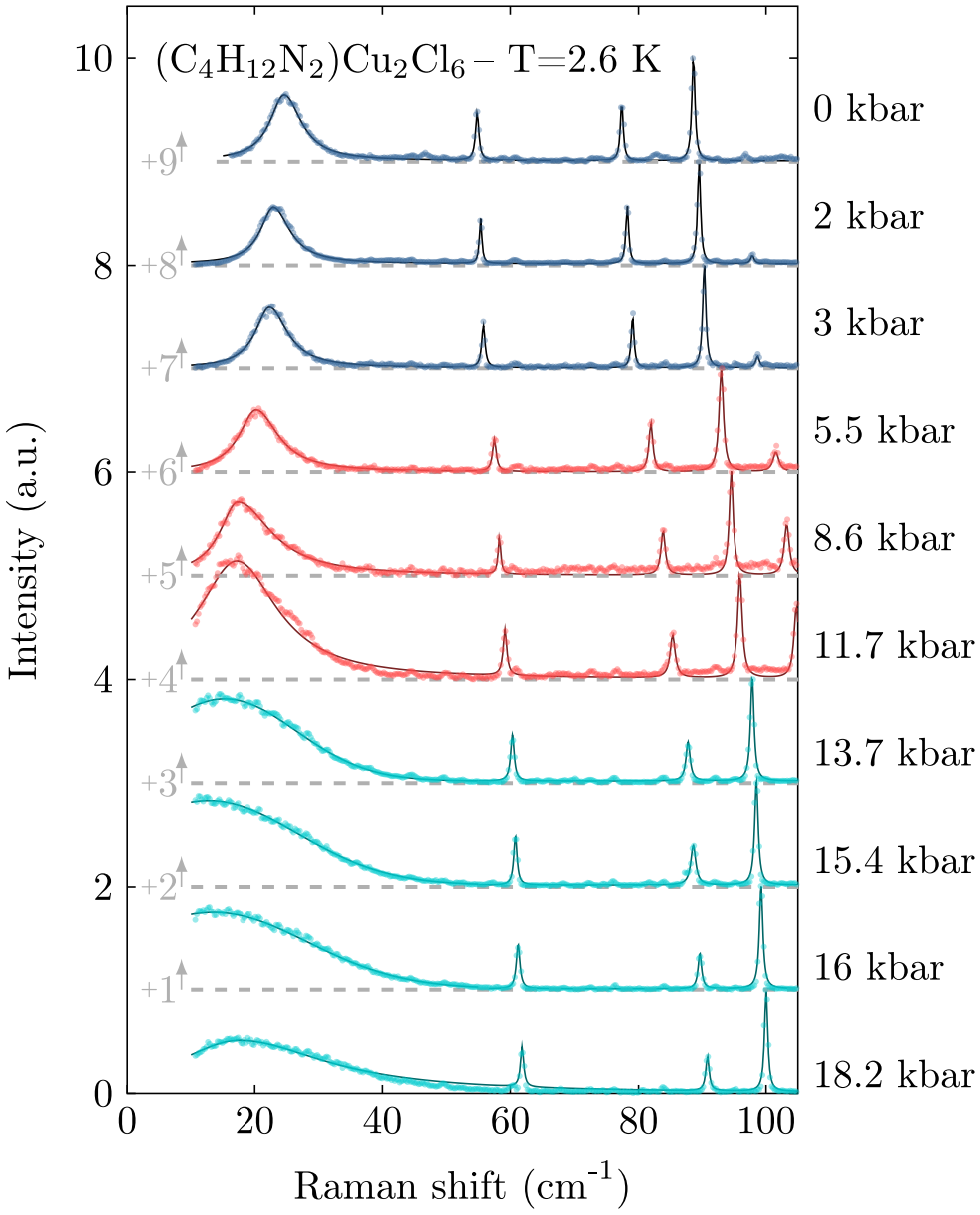

Figure 4.4: Stokes Raman scattering spectra measured in $(C_4H_{12}N_2)Cu_2Cl_6$ at $T = 2.6$ K in $\bar{Z}(XX)Z$ polarization, normalized to the peak intensity of the phonon with ω_0=88.5 cm^{-1}. Individual spectra are shown with incremental offsets for clarity. The solid lines are guides for the eye obtained in empirical Lorentzian (0–12 kbar and 18.2 kbar) or Gaussian (13–16 kbar) fits to the continuum contribution.

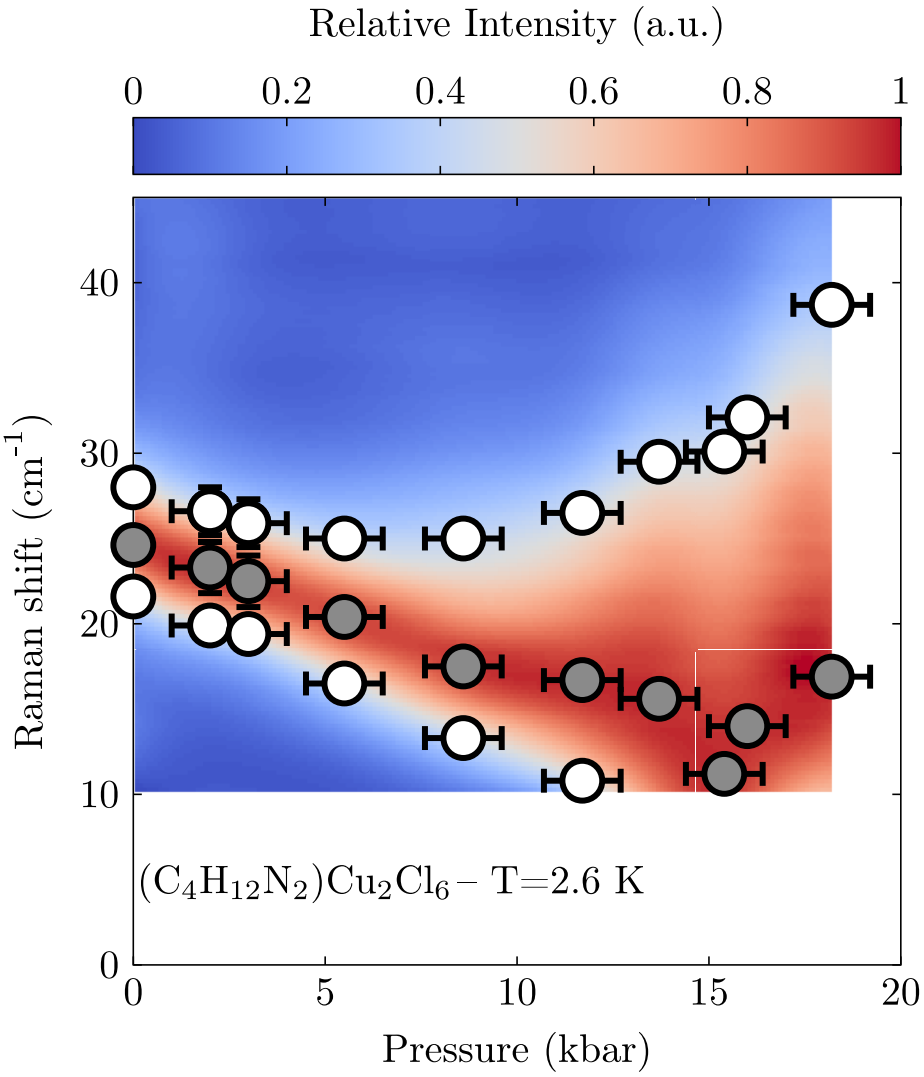

Figure 4.5: Peak position and half-maximum frequencies of continuum magnetic scattering as extracted from Stokes spectra at $T = 2.6$ K in $\bar{Z}(XX)Z$ polarization.

shape with a slight tail towards higher energies. Throughout this pressure range the continuum width and shape remain constant, while it shifts to lower energies as a whole (Fig. 4.4). In the intermediate-pressure range between P_c and $P_1 \sim 13$ kbar, we additionally observe a progressive change in the shape of the scattering. Whereas in the low-pressure range the asymmetry of the magnetic peak was subtle, the high-energy tail becomes considerably more pronounced at higher pressure. Increasing the pressure above $\sim P_1$ results in a further significant change in the shape of the spectrum. The magnetic scattering peak becomes rounded and overdamped, with no clear maximum. Increasing the pressure further the spectrum continues to be broadened and develops a long high-energy tail.

Unlike in simple spin systems such as spin ladders[120, 121], in a material with magnetic interactions as complex as they are in $(C_4H_{12}N_2)Cu_2Cl_6$ a quantitative analysis of the Raman spectrum does not appear feasible. To date, there exist no model calculations of even the single-magnon dispersion in $(C_4H_{12}N_2)Cu_2Cl_6$, let alone the Raman spectrum. As previously mentioned, even describing the ground state in terms of J_1-dimers is only approximate, since interdimer coupling is almost as strong. Instead, we chose a model-independent way to quantify the measured spectra. In Figure 4.5 we plot the positions of the maximum of magnetic scattering, and frequencies where the intensity reaches half of its maximum value. The color map in the background represents the measured Raman intensity relative to its maximum value at each pressure.

Phonons

Tracking the measured phonon frequencies against pressure confirms that the two transitions at P_c and P_1 are not associated with any crystallographic transformations. Indeed, as shown in Fig. 4.6, all phonons observed at base temperature show a smooth and almost linear pressure dependence (hardening). None of disappearing, splitting, or an appearance of new phonon lines was detected up to 18.2 kbar applied pressure.

Despite the monotonic pressure dependence at a fixed low temperature, most of the observed phonons show a remarkable pressure-induced evolution of their temperature dependencies. As shown in Fig. 4.3, the magnitude of the low-temperature frequency shifts is highly pressure dependent. For the two phonons

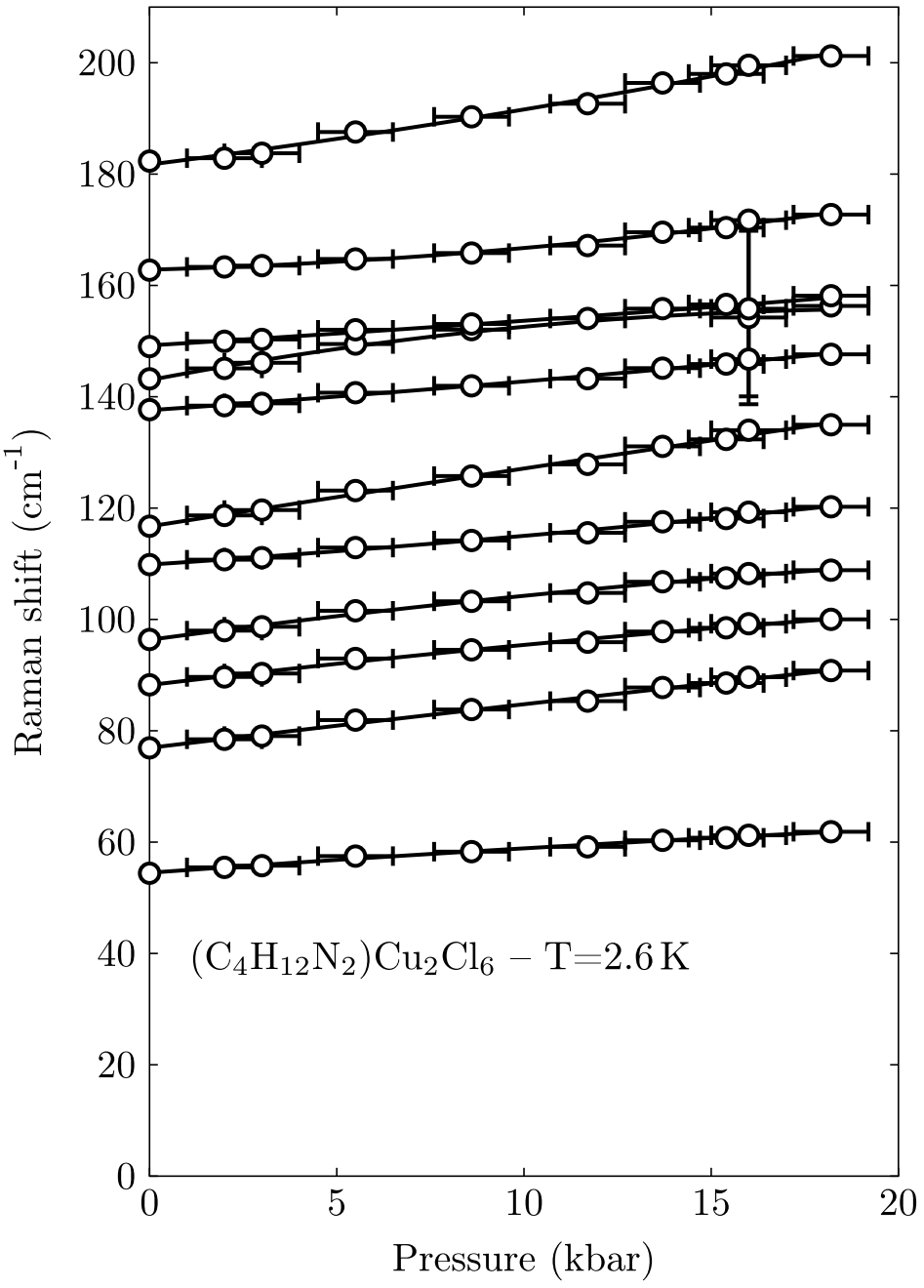

Figure 4.6: Pressure dependence of the phonon frequencies measured in $(C_4H_{12}N_2)Cu_2Cl_6$ at $T = 2.6$ K. Lines are guides to the eye.

that harden with increasing temperature at ambient pressure, even the *sign* of the temperature shift reverses under pressure. This reversal occurs between 11.7 and 15 kbar, and thus seemingly coincides with P_1.

4.2 Discussion

As argued in section 4.1.1, the magnetic scattering continuum can be ascribed to scattering from two-magnon processes that span between twice the energy gap and twice the maximum of magnon dispersion. Within this interpretation, the observed evolution of the spectrum below P_c implies a progressive softening of the gap without much change in the magnon bandwidth, in agreement with the neutron results. The only other comparable high pressure Raman study of a quantum paramagnet that we are aware of is that on $KCuCl_3$[122]. The much broader resolution, stronger elastic line and lower signal-to-noise ratio of the spectra reported in that work make a direct comparison to our data difficult.

What in our optical measurements on $(C_4H_{12}N_2)Cu_2Cl_6$ is clearly in contradiction with the previous neutron experiments of Ref. [11] are the observed steady increase of the magnon bandwidth above about 10 kbar, as deduced from the behavior of the upper continuum half-height frequency, and the clear changes of the shape of the scattering across the transition at P_1. In contrast, inelastic neutron scattering detected only insignificant changes in spin dynamics between 9 kbar and 18 kbar. Even those were only revealed in a quantitative fit to the measured neutron spectra, particularly to neutron intensities. The most likely reason for this discrepancy is an incorrect pressure calibration in the neutron study. As only became apparent through recent experience with the pressure cell used in the neutron experiment, the actual pressure can drop by as much as a third, compared to nominal, upon cooling the cell down to base temperature [78]. This effect was not taken into account in Ref. 11. Its magnitude for that particular experiment can not be assessed without additional in-situ pressure measurements using the same sample as in the original study. It appears likely though, that the nominally 18 kbar neutron data set actually corresponds to a pressure just below P_1. Note that in the present optical study the pressure is known reliably, as it is measured in situ at the experimental temperature. We

thus confirm that the transition at P_1 is, indeed, accompanied by a substantial change in spin excitations and a rapid increase of the excitation bandwidth.

We can expect a direct connection between the evolution of the magnetic ground state and the behavior of anomalous phonons. First, note that the anomalous phonon behavior occurs below about 20 K. In most conventional materials, phonon frequencies remain constant at such low temperatures. The only energy scale in $(C_4H_{12}N_2)Cu_2Cl_6$ that would be consistent with the low temperature range is that of magnetic exchange interactions. Below 20 K is precisely where short-range spin correlations set in. For the strongest bonds, the typical exchange energy in $(C_4H_{12}N_2)Cu_2Cl_6$ is about 1 meV[50], which is larger but comparable to the observed anomalous frequency shifts (about 0.15 meV for the $\omega_0 = 181.3$ cm^{-1} mode). With a high degree of certainty the anomalous behaviour can therefore be attributed to magnetoelastic coupling. The pressure dependence of anomalous frequency shifts signifies a strong pressure dependence of the local spin correlations in the system. A phase transition to a qualitatively different magnetic structure that we expect to occur at P_1 will thus have a particularly strong effect. We can speculate that it may be responsible for the observed sign reversals of two anomalous frequency shifts. A more concrete discussion of the microscopic mechanism would require an unambiguous identification of the the eigenvectors for the anomalous modes, which is presently lacking.

Chapter 5

Sign-switching of dimer correlations in $SrCu_2(BO_3)_2$ under pressure

The results presented in this chapter are also published in
S. Bettler, L. Stoppel, Z. Yan, S. Gvasaliya, and A. Zheludev. "Sign switching of dimer correlations in $SrCu_2(BO_3)_2$ under hydrostatic pressure.", Phys. Rev. Research 2, 012010(R) (2020) doi: 10.1103/PhysRevResearch.2.012010

How can one be sure that the pressure-induced phase which was found above ∼18 kbar is indeed plaquette-, rather than dimer-based? To date, the only supporting evidence comes from studies of the wave vector dependence of inelastic neutron scattering intensities[34]. Performing such measurements in a bulky cell needed to produce the required pressure for a sufficiently large sample is a formidable task. The resulting data are unavoidably limited and noisy, leaving the interpretation depending on strong assumptions and theoretical modeling [34]. In the present work we use an entirely different approach. We infer the strength of dimer spin correlations in $SrCu_2(BO_3)_2$ from their effect a particular optical phonon, called the pantograph mode. The phonon frequency can be measured with very high precision using Raman spectroscopy in a diamond-anvil pressure cell. We show that around P_c correlations on the dimer bond switch from AF to dominantly FM, and thereby independently confirm the destruction

of the AF-dimer ground state. Moreover, we obtain a *quantitative* estimate for the dimer spin correlations at pressures up to 34 kbar.

5.1 Results

A typical low-energy Raman spectrum collected in $SrCu_2(BO_3)_2$ at a pressure of $P = 2$ kbar and $T = 2.6$ K is shown in Fig. 5.1a. The observed frequencies appear fully consistent with previous measurements at ambient pressure [123]. The three visible lowest-energy excitations are magnetic in origin: two triplets and one singlet. All remaining peaks are phonons. The peak widths are in all cases below 1 cm^{-1} and correspond to the expected instrumental resolution. Since data for the entire spectrum are accumulated concurrently, this confirms that temporal drift of spectrometer alignment during the long data collection period is a non-issue.

The pantograph mode is the peak at around 198 cm^{-1}. It was identified by a density functional theory (DFT) ab-initio calculation with the Quantum Espresso software package [115], using the SSSP Accuracy (version 1.1) pseudopotential library [118, 124–129]. The kinetic energy cutoff was 120 Ry and the charge density cutoff 600 Ry. Brillouin zone integration was performed using a 4×4×4 k-point grid. For better convergence, a Marzari-Vanderbilt cold smearing of 0.01 Ry was applied. A detailed list of the DFT result and a comparison to literature values is given in appendix A.

In order to validate the experimental methodology we first checked the behavior of the three *magnetic* excitations. With increasing pressure all three peaks shift to lower energies and progressively weaken. Their measured frequencies are plotted in colored circles in Fig. 5.1c. At higher pressures they become undetectably weak or shift outside our measurement window (T_1). The observed softening of the triplet modes is fully consistent with previous electron spin resonance(ESR) [38] and inelastic neutron scattering [34] studies, shown as triangles and squares in the figure. The softening of the singlet mode is a new result, since neither ESR nor neutrons are sensitive to singlet-singlet transitions.

Dimer correlations from low-temperature phonon anharmonicites The central result of this project is the observation of an anomalous temperature de-

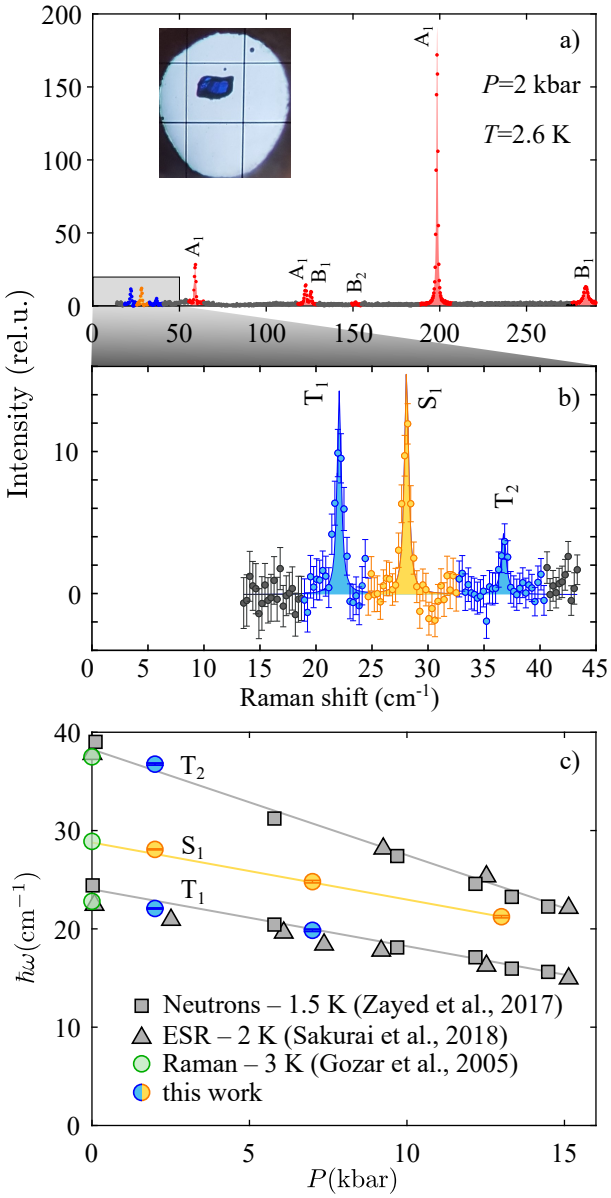

Figure 5.1: a) Raman data at T≈ 2.6 K and 2 kbar in $\bar{c}(a'b')c$ polarization measured with λ=532 nm laser. Symmetries of phonons are assigned as in Ref. [123]. Inset: picture of the single crystal sample inside the pressure cell along with two ruby spheres used for pressure calibration. b) Blowup of the low-energy portion of a). Triplets T_1 and T_2 and singlet S_1 are assigned according to Ref .[123] c) Comparison of excitation energies of singlet and triplet excitations to published results [34, 38, 123].

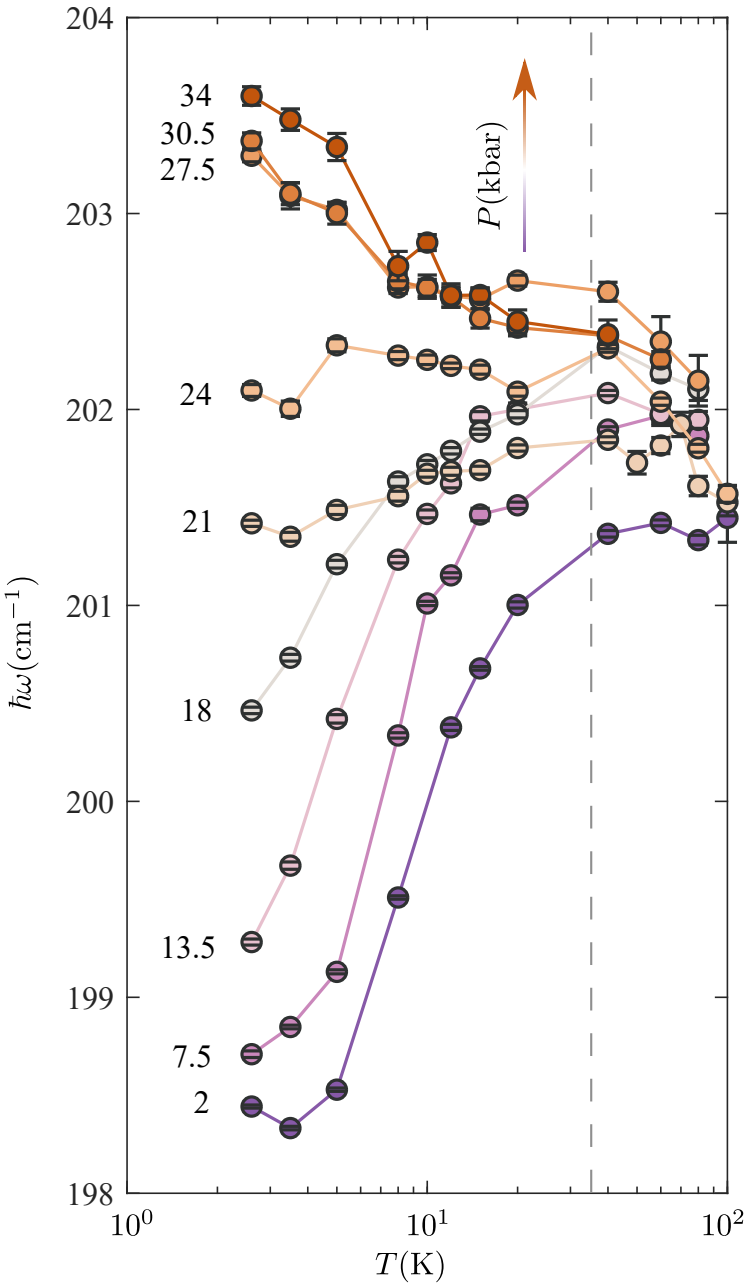

Figure 5.2: Measured temperature dependence of the pantograph mode frequency in $SrCu_2(BO_3)_2$ at different pressures. Note the logarithmic temperature scale. The dashed line is the temperature corresponding to the spin gap energy at ambient pressure.

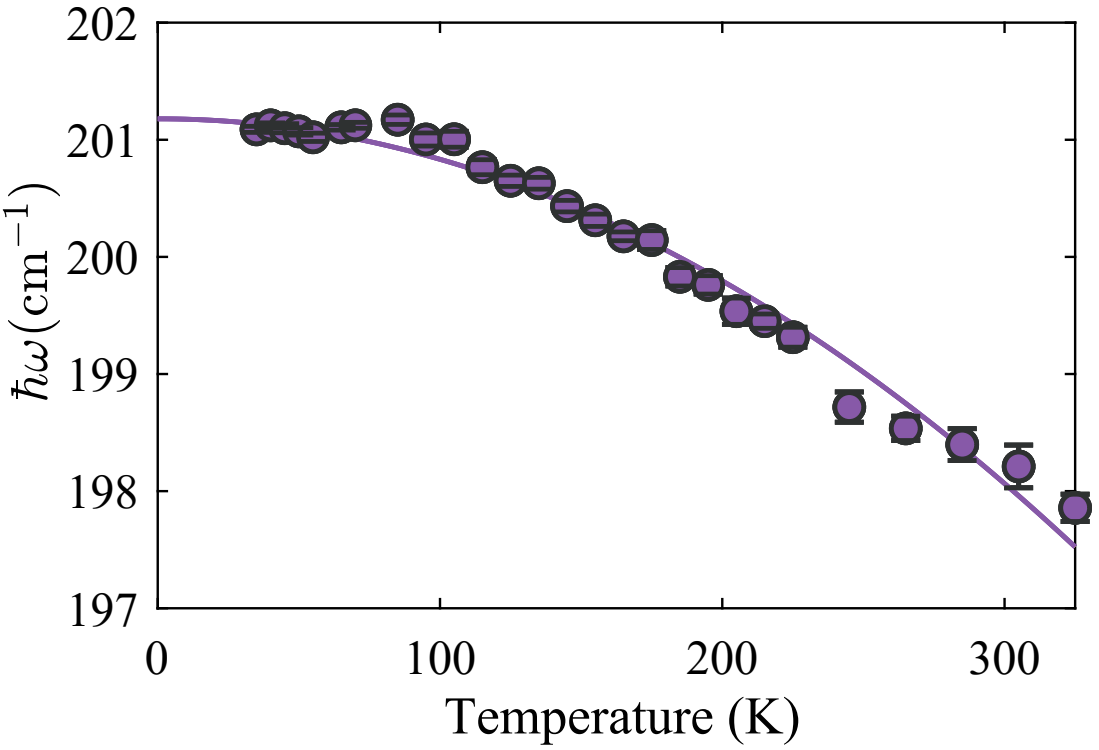

Figure 5.3: Measured temperature dependence of the pantograph mode in $SrCu_2(BO_3)_2$ at ambient pressure (symbols) and fit assuming anharmonic multi-phonon coupling (solid line).

pendence of the pantograph mode in $SrCu_2(BO_3)_2$, as visualized in Fig. 5.2. Note the logarithmic temperature scale. At all pressures, the pantograph mode undergoes at most a modest hardening upon cooling down to 40 K. This behavior is due to the usual anharmonicities of lattice vibrations and the temperature dependence of pressure in the loaded cell at higher temperatures.

In order to establish this, we measured the temperature dependence of the pantograph mode frequency between 35 K and room temperature at ambient pressure. The result is visualized in Fig. 5.3 (symbols). These data were analyzed using the a wide-spread empirical model for anharmonic multi-phonon coupling (Eq. 3.9 in [130]). An excellent fit is obtained using empirical parameters $\omega_0 = 201.2$ cm^{-1}, $C = 0$ and $D = -2.7(1) \cdot 10^{-3}$ cm^{-1} (solid line in Fig. 5.3). Extrapolating this curve to below 40 K yields an estimate of the anharmonic shift

in the low-temperature range: $\delta\omega \lesssim 0.1$ cm^{-1}. This is considerably smaller than the observed anomalous magnetic frequency shift and can be safely disregarded.

Below this point the mode suddenly becomes strongly T-dependent. At low applied pressures it *softens* upon cooling to base temperature by as much as 1.5%. At the highest pressures the effect is reversed: in the same low-temperature interval the excitation hardens by as much as 0.5%. Also revealing is the pressure dependence at different temperatures shown in Fig. 5.4 a). For $T \gtrsim 40$ K the pressure dependencies are almost T-independent. They all show a monotonous hardening with a small but reproducible dip at about 20 kbar. At lower temperatures the situation changes drastically, the frequency showing a steep, almost step-like, increase.

5.2 Discussion

At temperatures below 40 K anharmonic effects extrapolated from measurements above 35 K are entirely negligible 5.3. The only remaining relevant energy scale is the magnetic one. We conclude that the anomalous temperature dependence of the pantograph mode is due to magneto-elastic coupling. The corresponding relative frequency shift between 40 K and 2.6 K is plotted against pressure in Fig. 5.4 b) (left axis). As mentioned above, the cell pressure is practically constant in this temperature range. The shift remains flat up to about $P_1 \sim 15$ kbar and then steadily increases up to the highest attainable pressures, switching sign at about $P_2 \sim 22$ kbar.

As shown by ESR experiments [38], J' decreases by only about 12% from 0 to 15 kBar. This allows us to assume that the 2nd derivative in Eq. 2.19 is also *only weakly pressure-dependent* to some approximation. The lack of any pressure dependence for $P \lesssim P_1$ in Fig. 5.4 b) confirms this. Here the system is clearly in the dimer phase [34]. In this regime the exact result is $\langle \mathbf{S}_1 \mathbf{S}_2 \rangle \equiv -\frac{3}{4}$ regardless of J'/J [14], and the measured constant frequency shift implies a constant $\partial^2 J'/\partial u^2$. Assuming the trend continues at higher pressures, to within a scale factor Fig. 5.4 b) represents the pressure dependence of $\langle \mathbf{S}_1 \mathbf{S}_2 \rangle$. The exact value for the dimer phase provides a calibration for the entire plot (Fig. 5.4b), right axis). At P_2 the relative alignment of nearest neighbor spins *switches sign and becomes predominantly ferromagnetic.*

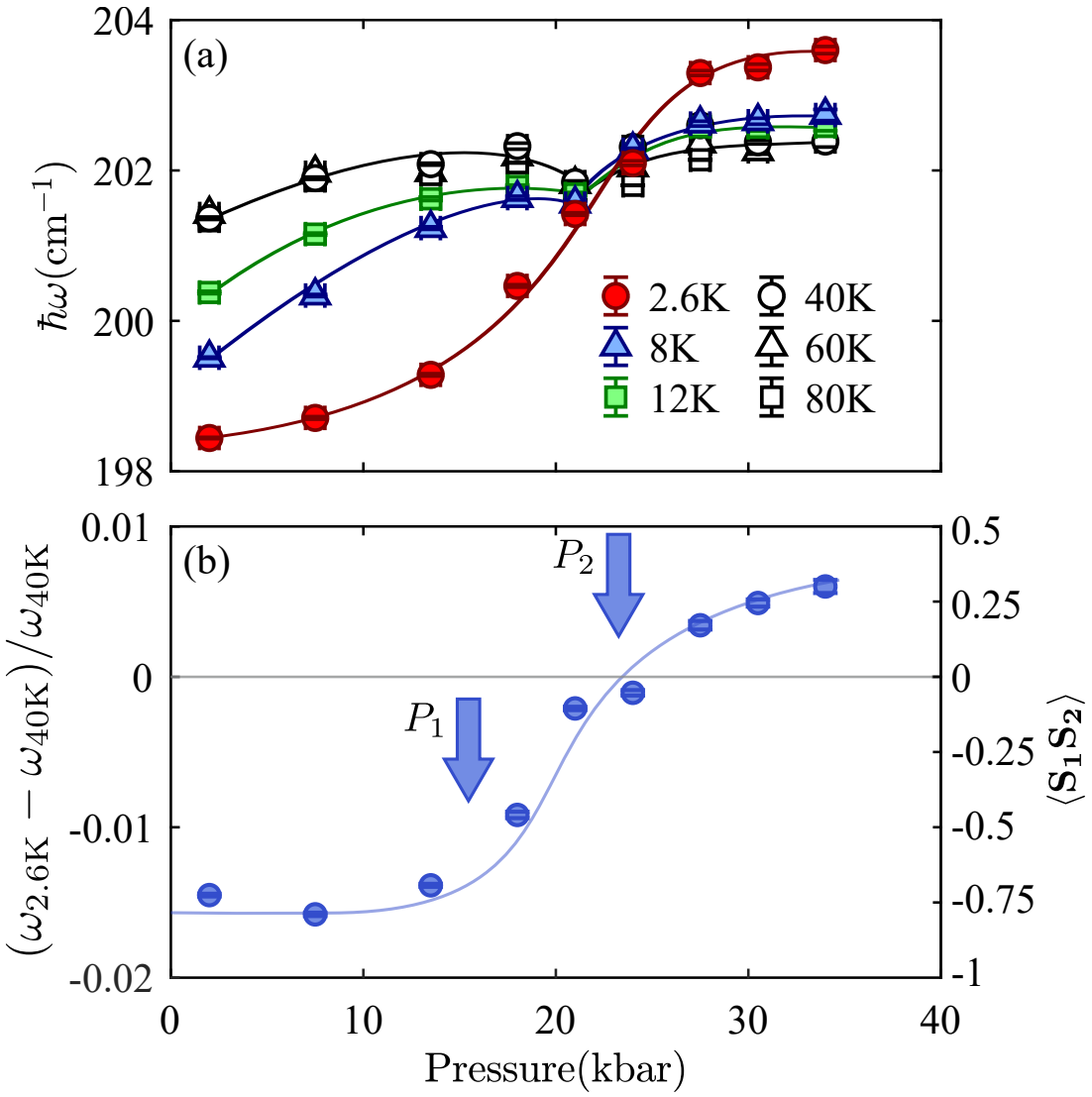

Figure 5.4: a) Measured pressure dependence of the pantograph mode frequency in $SrCu_2(BO_3)_2$ at several different temperatures (symbols). The lines are guides for the eye. b) Pressure dependence of the low-temperature frequency shift of the pantograph mode. P_1 indicates the beginning of the destruction of dimer correlations and P_2 denotes the sign switching of dimer correlations. The solid line is a guide to the eye.

That AF dimers are replaced by a completely new spin correlation pattern already at rather low pressures is significant. The only other indication of that is the rather tenuous 22 kbar strucure factor data from the neutron study of Ref. [34]. The transformation that we observe starts already at about 15 kbar. It can only be driven by a subtle change in the J'/J ratio, as assumed in most theoretical studies [13–31]. It takes place long before the exchange constants themselves can be expected to switch sign [38]. It also seems not to be associated with any structural transition, of which we do not observe any obvious signs such as splitting of phonon lines or the appearance of new modes.

According to a recent calorimetric study [35], there is a distinct thermodynamic phase that emerges below $T_c \sim 2$ K just about P_1. The authors suggest that it may be a plaquette state. The sign-switching reported here is consistent with that interpretation. While in the dimer phase the spin correlations are AF, in the plaquette state they at least partially switch to FM and may evolve continuously[28, 31]. Unfortunately, the lowest attainable temperature in our experiments is slightly above T_c. The observed behavior can be interpreted as a change in the character of dominant *short-range* spin correlations, which are just about to order in a new plaquette configuration upon further cooling. According to [35], Néel magnetic order sets in above approximately P_2. Here even stronger FM correlations are predicted [28], and indeed observed in our measurements.

Chapter 6

Magnetic structure, spin waves and high-field phase diagram in the frustrated ferro-antiferromagnet $Pb_2VO(PO_4)_2$

The results presented in this chapter have in parts been published in S. Bettler, F. Landolt, Ö. Aksoy, Z. Yan, S. Gvasaliya, Y. Qiu, E. Ressouche, K. Beauvois, S. Raymond, A.N. Ponomaryov, S.A. Zvyagin and A. Zheludev. "Magnetic structure and spin waves in the frustrated ferro-antiferromagnet $Pb_2VO(PO_4)_2$.", Phys. Rev. B **99***, 184437 (2019) doi: 10.1103/PhysRevB.99.184437*

By their nature, previous bulk measurements and powder neutron diffraction experiments were unable to assess just how well $Pb_2VO(PO_4)_2$ corresponds to the ferro-antiferro square lattice model in the first place. This is a valid point of concern, since the material is monoclinic rather than tetragonal. Therefore, the spins no longer form a perfect square. The spin arrangement is not even rectangular. There are as many as four atoms per crystallographic unit cell with several inequivalent bonds between them. In the this chapter, the results of neutron diffraction, inelastic neutron scattering, magnetization and magnetic

torque measurements on *single crystal* samples of $Pb_2VO(PO_4)_2$ are reported. We show that the excitations deviate significantly from those of a perfect square lattice. Still, the material is found to be exceptionally two-dimensional. Furthermore, we accurately measure the direction and magnitude of the ordered moment at low temperatures. In an effort to identify a possible spin-nematic phase in $Pb_2VO(PO_4)_2$ we performed high-field measurements of the magnetic torque at very low temperatures, where we can expect the signatures of such a phase to be the strongest.

6.1 Results

6.1.1 Magnetic structure

The magnetic structure at T = 1.5 K was determined from an analysis of 11 measured magnetic reflections. These were normalized using the scale factor obtained from the least-square fitting of 22 nuclear Bragg peaks measured intensities (R-factor 4.2 %). A refinement, also using the FULLPROF SUITE package[131] yielded a unique solution, a collinear CAF-type spin arrangement with moments along the crystallographic b axis (Fig. 6.1). The resulting magnetic structure factors are plotted against wave vector in Fig. 6.2, solid symbols. The relative alignment of spins from adjacent V-planes is ferromagnetic. The final R-factor was 5.7%. The ordered moment was determined to be 0.68(1) μ_B per site. The calculated structure factors are plotted in open symbols in Fig. 6.2 for a direct comparison with experiment.

In Fig. 6.3 we show the temperature dependence of neutron intensity measured at the position of a purely magnetic $(1, 0, 0)$ Bragg reflection. A simplistic power law fit in the temperature range $2.48 < T < 9.93$ K yields an ordering temperature of $T_N = 3.50(1)$ K and a crude estimate of the order parameter exponent $\beta = 0.20(2)$.

6.1.2 Spin waves

The first column in Fig. 6.4 shows false color plots of inelastic neutron intensities measured in $Pb_2VO(PO_4)_2$ at different energy transfers at the MACS instrument.

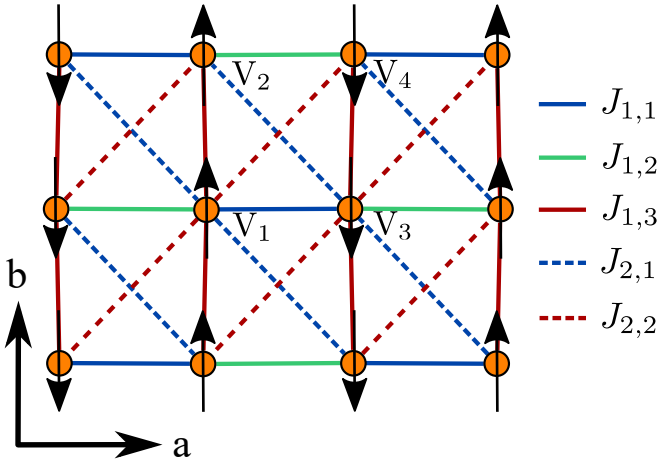

Figure 6.1: The five distinct nearest-neighbor and next-nearest-neighbor V-V bonds in each such layer (lines). Arrows represent the spin orientation in the ordered state as deduced from our single crystal diffraction data.

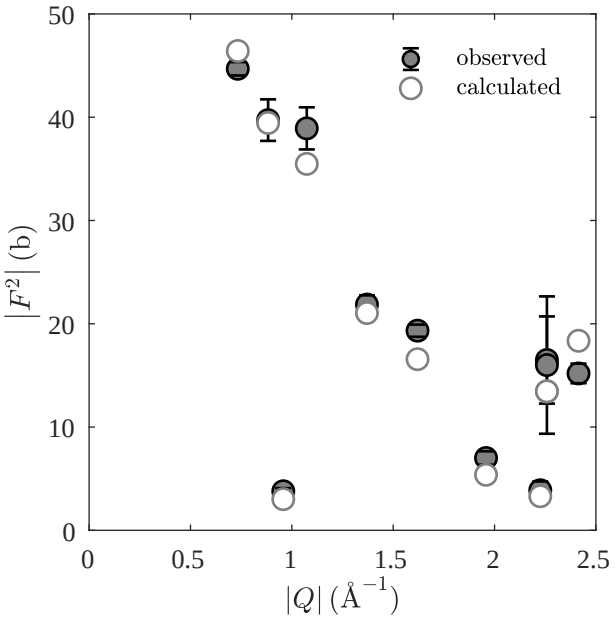

Figure 6.2: Measured (solid symbols) and calculated (open symbols) squared structure factors of magnetic Bragg reflections in $Pb_2VO(PO_4)_2$ plotted against momentum transfer.

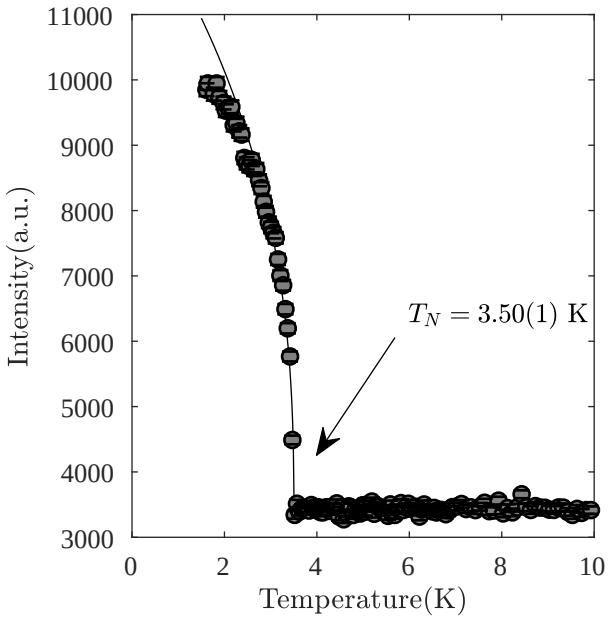

Figure 6.3: Measured temperature dependence of the $(1, 0, 0)$ magnetic Bragg peak intensity (symbols) and an empirical power law fit to the data as described in the text (solid line).

Bond	V-V-distance(Å)	J(meV)
$J_{1,1}$	4.42	-0.286(2)
$J_{1,2}$	4.66	-0.389(2)
$J_{1,3}$	4.67	
$J_{2,1}$	6.27	1.453(3)
$J_{2,2}$	6.30	0.538(2)

Table 6.1: Nearest and next nearest neighbor V-V distances in $Pb_2VO(PO_4)_2$ and exchange parameters obtained from analyzing the inelastic neutron data.

These spectra were modeled using linear spin wave theory, assuming a Heisenberg Hamiltonian with five distinct in-plane exchange constants as depicted in Fig. 6.1. The coupling between V-layers was assumed to be negligible, and all excitation widths were assumed to be resolution limited. The spin wave energies and structure factors were calculated using the program SpinW [132]. The neutron polarization factors were based on the collinear magnetic structure described above. The magnetic form factor for V^{4+} was taken in the dipolar approximation as calculated in Ref. 101. The thus computed inelastic magnetic neutron scattering cross section was numerically folded with the resolution function of the instrument calculated using the ResLib program [133]. The resolution calculation was done within the Popovici approximation [134]. The data collected at all energy transfers were fit simultaneously. However, since the process is rather computation intensive, all fits were restricted to a single Brillouin zone shown as a red rectangle at each energy in Fig. 6.4. The parameters were the five exchange constants, an overall intensity prefactor and a separate constant background at each energy transfer. Treating the exchange constants $J_{1,2}$ and $J_{1,3}$ as independent did not meaningfully improve the quality of the fits. Since they correspond to V-V bond lengths that are practically equal (but not identical by symmetry), in our final analysis they were constrained to be equal. An excellent fit is obtained with parameter values listed in Table 6.1. This set of Heisenberg exchange constants provides a very good description not only of the data in the target Brillouin zone, but also of that in the entire experimental range of momentum transfers. Intensities simulated using our fitting model and the final parameter set are shown in false color plots in the right column of Fig. 6.4.

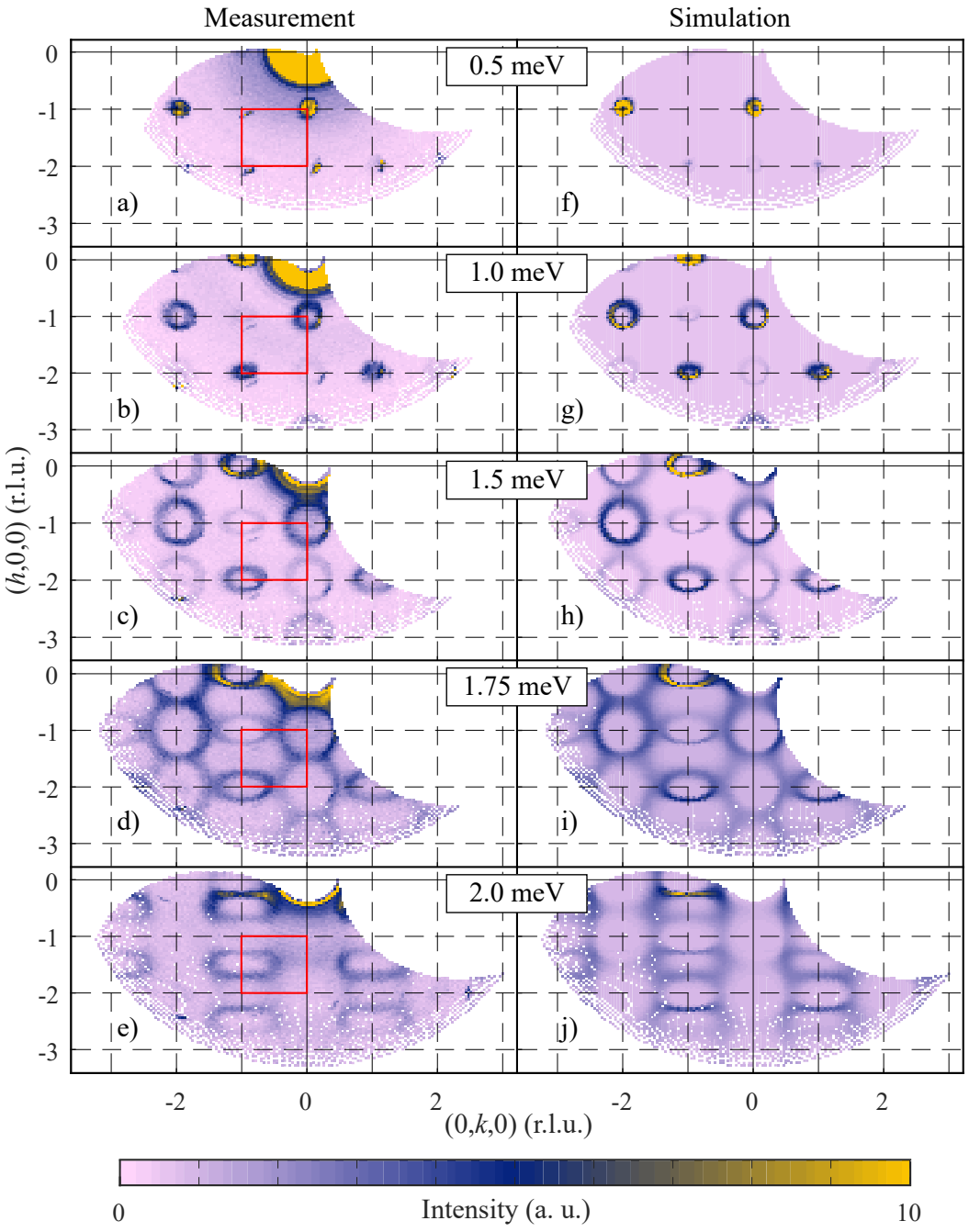

Figure 6.4: a)-e): False color plots of inelastic neutron scattering intensities measured in $Pb_2VO(PO_4)_2$ at $T < 0.1$ K on the MACS spectrometer. Each panel corresponds to a different energy transfer. f)-j): Spin wave theory simulations using fitted parameter values in Table 6.1 and a convolution with the calculated instrument resolution as described in the text. The red rectangle shows the Brillouin zone used in the fit.

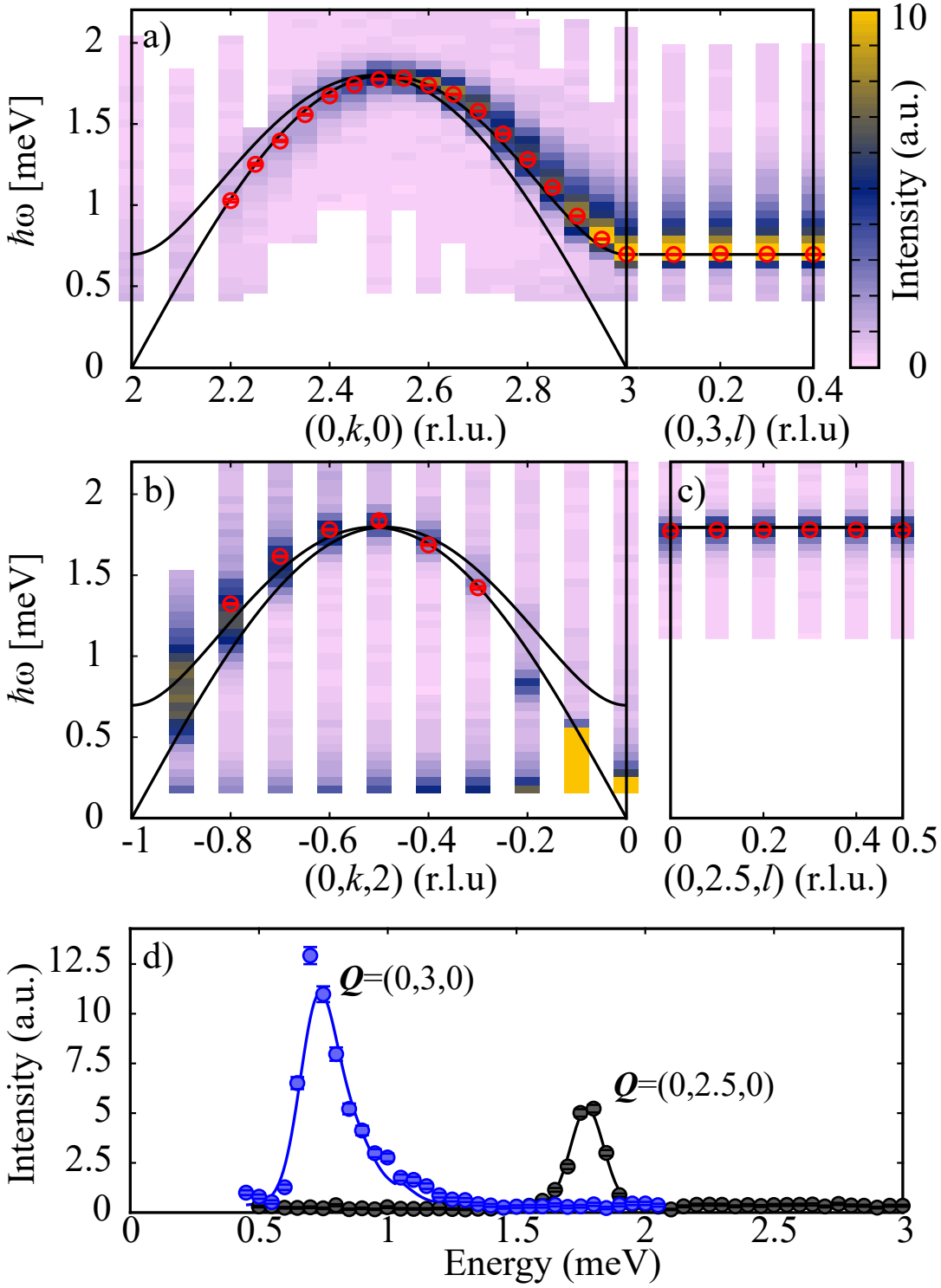

Figure 6.5: a)-c) False color plots of inelastic neutron scattering intensities measured at $T < 0.1$ K on IN12. Red symbols are peak positions in individual scans as obtained through the procedure described in the text. Solid lines show the spin wave dispersion calculated using parameter values in Table 6.1. d) Constant-Q scans at the Brillouin zone center and boundary. Solid lines are fits as described in the text.

The inelastic intensities collected on IN12 are shown in the false color plots of Fig. 6.5. In their analysis we also employed a combination of SpinW and ResLib, but chose to fit every energy scan separately. To account for resolution (focusing) effects, the spin wave dispersion was calculated using parameters values in Table 6.1. To independently extract the excitation energy in each scan, we allowed for an additional energy offset relative to this calculated dispersion. A flat background and an intensity scale factor were the two other parameters. The thus obtained spin wave energies are shown as open circles in Fig. 6.5. The solid lines are a dispersion calculation based on parameters in Table 6.1. We see an almost perfect agreement. The IN12 data re-affirm the determined values of in-plane exchange constants. In addition, they confirm a total lack of dispersion perpendicular to the planes. From our analysis we can estimate the corresponding bandwidth to be smaller than 20 μeV.

6.1.3 Magnetization

The observed magnetization along along the crystallographic b-axis is shown in figure 6.6 and is consistent with previous observations[73]. The Néel temperature $T_N \approx 3.5$ K was confirmed. The combination of a radial offset and non-spherical sample shape are a plausible explanation for the differences in measured magnetization of the order 1-2%.

6.1.4 Magnetic torque

For the external field applied along the anisotropy axis b, the only signatures were the previously observed[73] spin-flop transition at ~ 1 T(Fig.6.7) and saturation into a fully polarized state at $H_{sat} \sim 20.7$ T(Fig.6.8). In contrast, as seen in Fig.6.9 for the magnetic field applied perpendicular to the magnetic planes along c^*, an additional feature indicative of a first-order transition was observed at a field $H^* \sim 19.4\ T$. The results obtained on $Pb_2VO(PO_4)_2$ are summarized in the phase diagram shown in Fig.6.10. The low-field phase diagram for $H||c^*$ was obtained trough vibrating sample magnetometry. The phase boundary for $H||b$ is complemented by data digitized from reference [73], which was obtained through specific heat measurements.

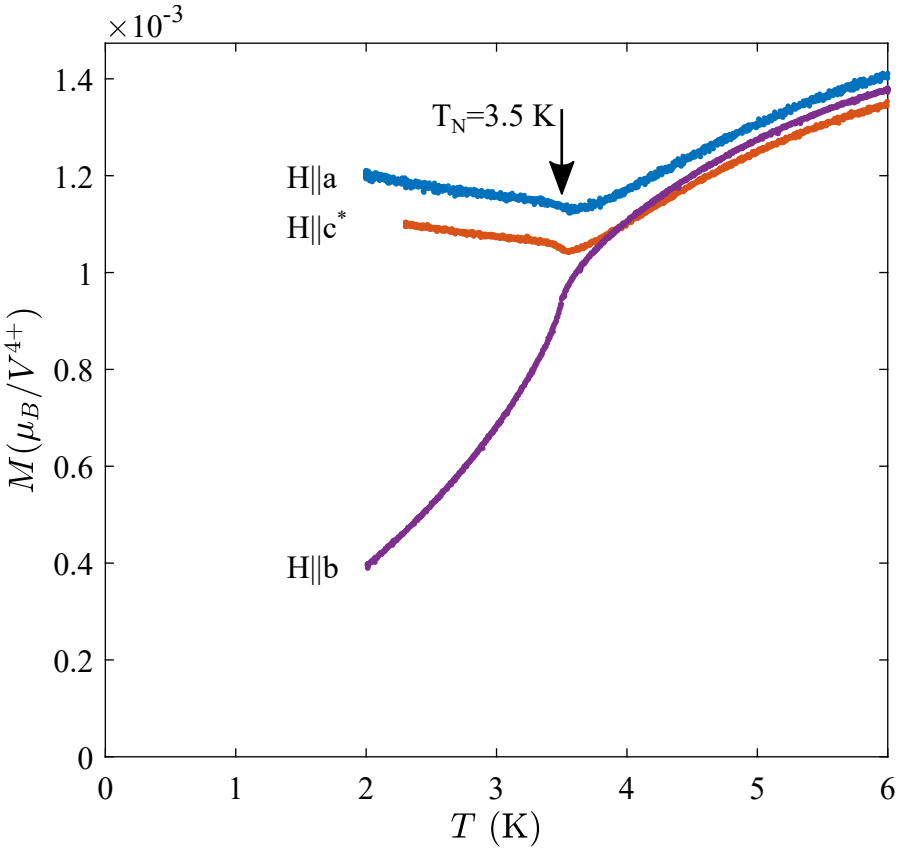

Figure 6.6: Temperature-dependence of magnetization in $Pb_2VO(PO_4)_2$ at 0.1 T.

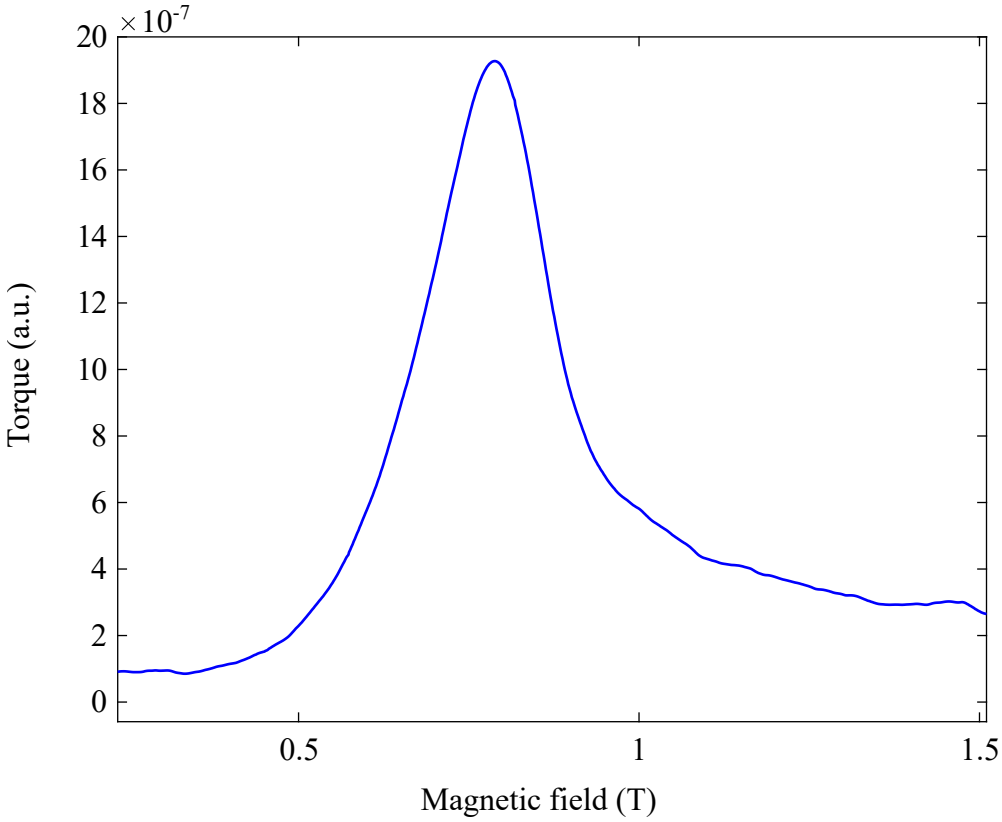

Figure 6.7: Magnetic torque at the spin-flop transition for the field $H||b$, measured at 20 mK.

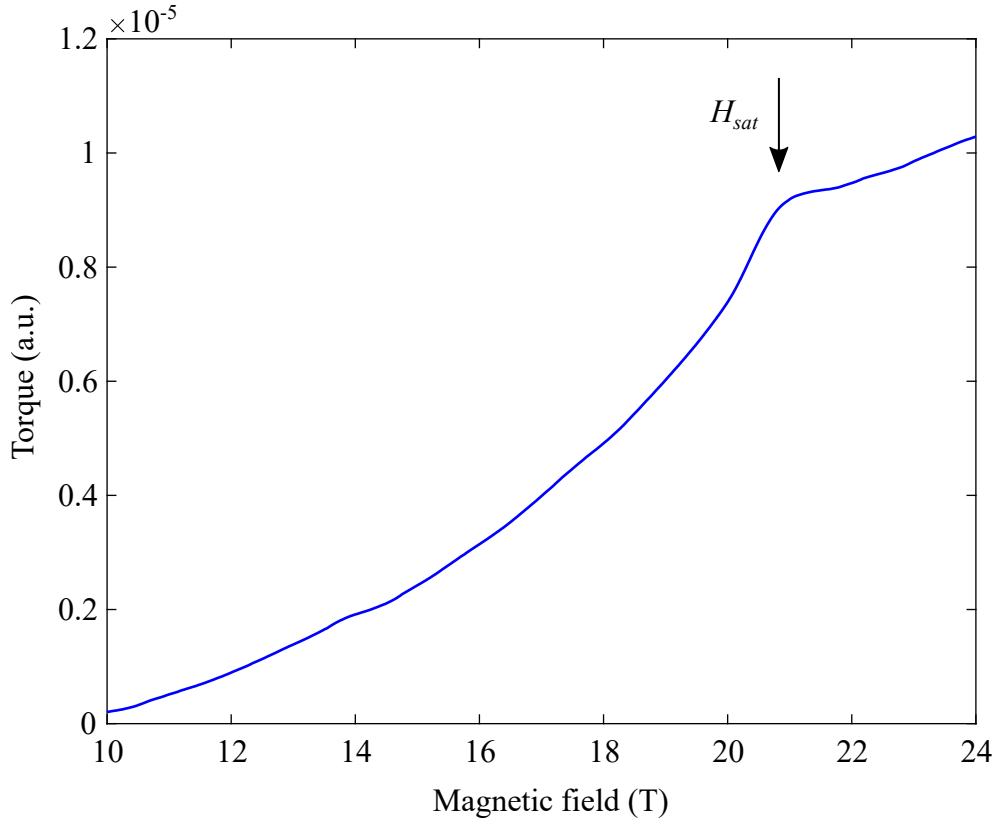

Figure 6.8: Magnetic torque for the field $H||b$, measured at 30 mK.

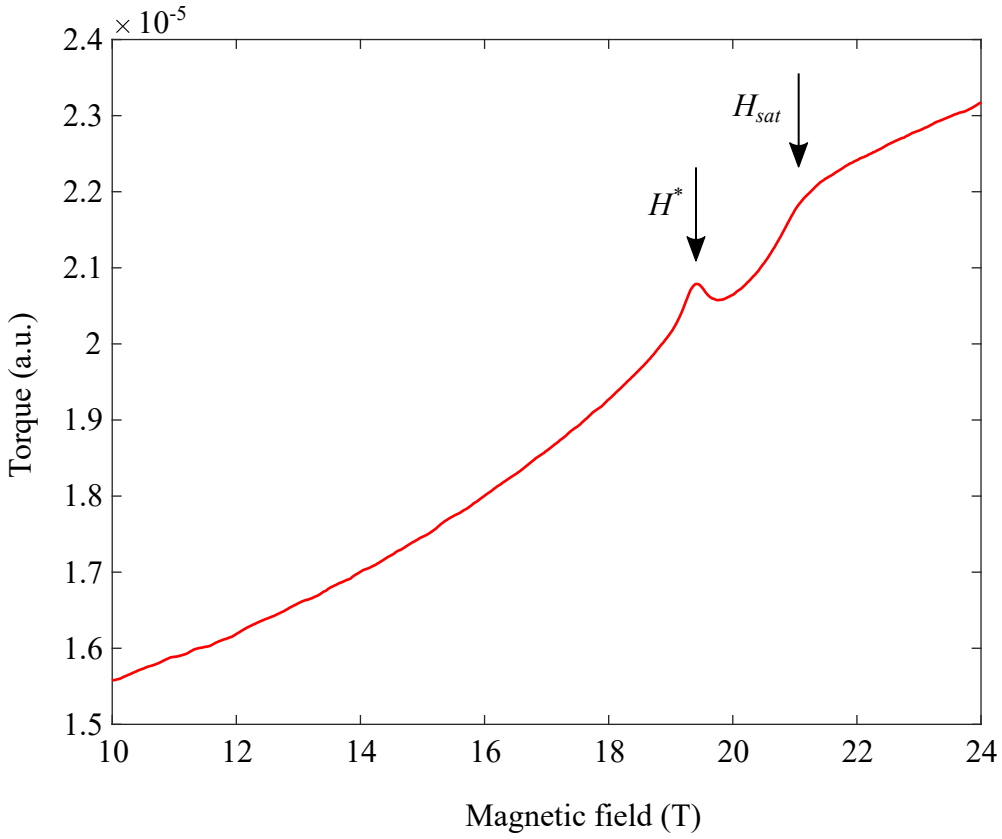

Figure 6.9: Magnetic torque for the field $H||c^*$, measured at 20 mK.

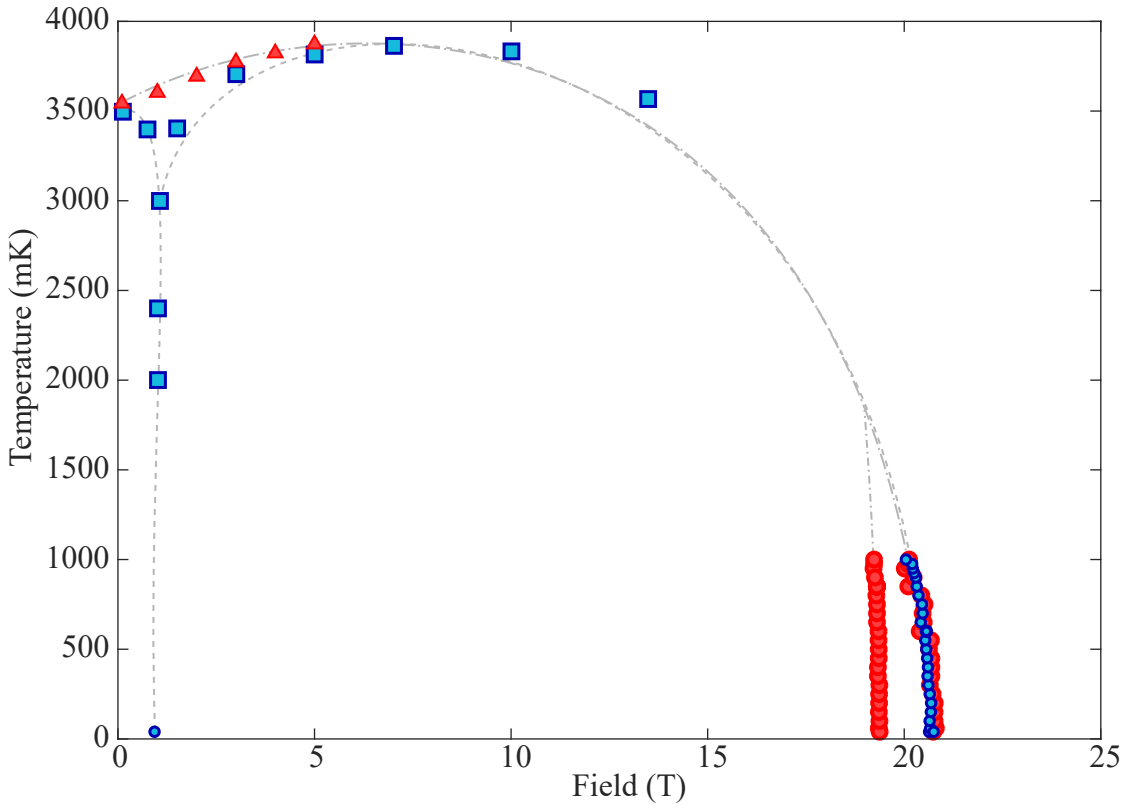

Figure 6.10: Field-temperature phase diagram of $Pb_2VO(PO_4)_2$. Phase boundary for field $H||b$ (■) digitized from Ref.[73]. Phase boundary for field $H||c^*$ (▲) obtained from magnetization measurements. Low-temperature phase boundary for field $H||b$ (●) and $H||c^*$ (●)extracted from magnetic torque measurements. Dashed lines are a guide to the eye for field $H||b$. Dash-dot lines are a guide to the eye for field $H||c^*$.

6.2 Discussion

While our results confirm the two-dimensional nature and a CAF-type magnetic structure for $Pb_2VO(PO_4)_2$, they also unambiguously show that a square lattice description with only two exchange parameters is insufficient to describe the magnetism in this compound. The nearest-neighbor coupling constants are indeed all ferromagnetic, but alternate substantially along the a axis. The most significant consequence is the splitting of the spin wave spectrum into two separate branches as seen in Fig. 6.5. This produces an additional gapped excitation at each zone-center, as also seen with ESR[135, 136]. Next nearest neighbor interactions are AF, but differ by almost a factor of three along the two diagonals.

Our data also show that the material is less frustrated than originally thought. A good measure of frustration is the ratio $\alpha^{-1} = 1 + S^2 \sum |J|/E_{\rm cl}$, where $\sum |J|$ is the sum of absolute values all exchange constants and $E_{\rm cl}$ is the classical ground state energy. In all cases $\alpha^{-1} \leq 0$ with $\alpha = 0$ corresponding to an absence of frustration. For the ferro-antiferromagnet square lattice CAF, $\alpha^{-1} = J_1/J_2$. In our exchange model for $Pb_2VO(PO_4)_2$, $E_{\rm cl}/S^2 = J_{1,3} - J_{1,1}/2 - J_{1,2}/2 - J_{2,1} - J_{2,2}$ and $\alpha^{-1} \approx -0.32(1)$. Previous estimates based on an assumed square lattice model[108] correspond to a stronger frustration $\alpha^{-1} \approx -0.62$. A weak frustration in $Pb_2VO(PO_4)_2$ is consistent with a rather large observed ordered moment. The latter is similar to that found in strongly 2-dimensional but unfrustrated $S = 1/2$ AFs such as the cuprates [137].

Given that the square lattice description of $Pb_2VO(PO_4)_2$ is clearly deficient, the observation of a pre-saturation phase raises the question whether $Pb_2VO(PO_4)_2$ could feature a spin-nematic phase after all. The identification of the phase as a spin-nematic is demanding since such an order does not break time-reversal symmetry[40]. Spin-nematic pre-saturation phases have been proposed to exist in the frustrated spin chain materials β-$TeVO_4$[138] and $LiCuVO_4$[139] and the distorted square lattices volborthite[140] and $BaCdVO(PO_4)_2$[141, 142]. However, a recent neutron diffraction study on β-$TeVO_4$ showed that the proposed spin-nematic phase in fact still features dipolar long range order[143]. In $LiCuVO_4$ the saturation field is far beyond reach of most experimental techniques and a direct verification of the nature of the high field phases in this compound will remain extremely challenging. In volborthite the magnetic Hamiltonian, ground state and

the nature of the several field-induced phases are still largely unclear[144–146]. The best candidates to observe spin-nematic order thus remain $BaCdVO(PO_4)_2$ and $Pb_2VO(PO_4)_2$. It is however not excluded that another type of dipolar order is stabilized instead.

Chapter 7

Conclusion

We have shown that neither of the pressure-induced magnetic transitions in $(C_4H_{12}N_2)Cu_2Cl_6$ involve crystallographic transformations. The transition at P_c is associated with a progressive softening of the magnon gap with little change of bandwidth. Contrary to previous indications, the transition at P_1 leads to a substantial reorganization of the spin excitation spectrum. The corresponding change of the magnetic ground state has a dramatic impact on the temperature dependencies of certain phonon modes. This indicates that the low- and the high-pressure ordered phases in $(C_4H_{12}N_2)Cu_2Cl_6$ are clearly distinct. The overdamped nature of the two-magnon continuum close to P_1 is reminiscent of multi-spinon continua observed e.g. with resonant inelastic x-ray scattering at $Q = 0$ in spin chains[147]. This is surprising given that μSR experiments found clear signs of commensurate long range order above P_1[9].

Our measurements of the pantograph mode in $SrCu_2(BO_3)_2$ provide an indirect but precise measurement of a pressure-induced sign switching of nearest-neighbor dimer spin correlations. We hope that a quantitative comparison with theoretical studies will become possible in the future. A low-temperature investigation of the crystal structure under pressure may yield detailed information on magnetic correlations and the magnetic order which is eventually established. In addition, high-quality crystallographic information is an important prerequisite for accurate theoretical predictions.

While $Pb_2VO(PO_4)_2$ and probably all related layered vanadophosphates are indeed highly two-dimensional and feature competing ferromagnetic and antifer-

romagnetic interactions, the actual spin Hamiltonian in these systems is probably more sensitive to structural details than originally thought. The pre-saturation phase detected in magnetic torque measurements may be a spin-nematic phase. However, a further experimental characterization of this phase is necessary to determine its nature. Most importantly, the corroborated suppression of magnetic order at H^* should be verified by means of nuclear magnetic resonance and neutron diffraction.

Appendix A

First principles identification of phonons in $SrCu_2(BO_3)_2$

The pantograph mode is identified as the only A_1 Raman-active phonon in the range between 122 and 285 cm^{-1}. The difference between the calculated and observed frequency for the pantograph mode is reasonable($\sim$ 8 cm^{-1}). Considering the overall quality of agreement between calculated and observed phonon energies, this assignment can be considered safe. Due to the high symmetry of $SrCu_2(BO_3)_2$, most modes can be uniquely identified. It is noteworthy that saving two exceptions (18-19,42), the phonon energies are underestimated.

Symmetry(Nº)	DFT(cm^{-1})	Raman(cm^{-1})	IR(cm^{-1})
E(1-2)	0	-	-
B_2(3)	0	-	-
A_1(4)	23	59.0	-
B_2(5)	69	-	101
E(6-7)	77	-	80
E(8-9)	79	-	112
A_1(10)	101	121.8	-
B_1(11)	104	125.0	-
E(12-13)	113	-	125
E(14-15)	136	-	141
B_2(16)	143	151.0	150
A_2(17) *silent*	149	155.9	-

Symmetry(Nº)	DFT(cm^{-1})	Raman(cm^{-1})	IR(cm^{-1})
E(18-19)	167	-	157
A_1(20)	190	198.1	-
E(21-22)	192	-	223
A_2(23) *silent*	196	-	-
B_2(24)	203	-	211
E(25-26)	221	-	231
A_2(27) *silent*	236	-	-
A_1(28)	242	285.1	-
B_1(29)	278	282.7	-
E(30-31)	294	-	319
A_2(32) *silent*	296	-	-
B_2(33)	297	316.8	317
B_1(34)	303	322.9	-
B_1(35)	383	386	-
E(36-37)	384	-	424
B_2(38)	416	-	447
E(39-40)	436	-	443
A_2(41) *silent*	446	-	-
A_1(42)	475	473	-
A_2(43) *silent*	589	-	-
E(44-45)	604	-	661
B_2(46)	626	-	682
A_1(47)	643	-	-
B_2(48)	643	-	695
B_1(49)	650	706	-
A_1(50)	660	-	-
E(51-52)	665	-	693
E(53-54)	668	-	721
E(55-56)	915	-	934
B_2(57)	937	-	955
A_1(58)	939	950	-
B_1(59)	1195	-	-
A_2(60) *silent*	1225	-	-

Symmetry(N^o)	DFT(cm^{-1})	Raman(cm^{-1})	IR(cm^{-1})
E(61-62)	1227	-	1228
E(63-64)	1321	-	1308
B_2(65)	1325	-	1347
A_1(66)	1348	1360	-

Table A.1: Comparison of calculated and experimentally observed IR-([148]) and Raman-active([123, 148]) phonon energies for $SrCu_2(BO_3)_2$. Silent phonons are marked according to the DFT result.

Bibliography

[1] S. Sachdev, *Quantum magnetism and criticality*, Nature Physics **4**, 173 (2008).

[2] O. Starykh, *Unusual ordered phases of highly frustrated magnets: A review*, Reports on Progress in Physics **78**, 052502 (2015).

[3] E. G. Batyev and L. S. Braginski, Sov. Phys. JETP **60**, 781 (1984).

[4] T. Giamarchi and A. M. Tsvelik, Phys. Rev. B **59**, 11398 (1999).

[5] T. Giamarchi, C. Ruegg, and O. Tchernyshev, Nature Physics **4**, 198 (2008).

[6] H. Tanaka, K. Goto, M. Fujisawa, T. Ono, and Y. Uwatoko, *Magnetic ordering under high pressure in the quantum spin system TlCuCl3*, Physica B: Condensed Matter **329-333, Part 2**, 697698 (2003).

[7] C. Rüegg, A. Furrer, D. Sheptyakov, T. Strässle, K. W. Krämer, H.-U. Güdel, and L. Mélési, *Pressure-Induced Quantum Phase Transition in the Spin-Liquid* $TlCuCl_3$, Phys. Rev. Lett. **93**, 257201 (2004).

[8] K. Goto, M. Fujisawa, H. Tanaka, Y. Uwatoko, A. Oosawa, T. Osakabe, and K. Kakurai, *Pressure-Induced Magnetic Quantum Phase Transition in Gapped Spin System KCuCl3*, Journal of the Physical Society of Japan **75**, 064703 (2006).

[9] M. Thede, A. Mannig, M. Månsson, D. Hüvonen, R. Khasanov, E. Morenzoni, and A. Zheludev, *Pressure-Induced Quantum Critical and Multicritical Points in a Frustrated Spin Liquid*, Phys. Rev. Lett. **112**, 087204 (2014).

[10] T. Hong, C. Stock, I. Cabrera, C. Broholm, Y. Qiu, J. B. Leao, S. J. Poulton, and J. R. D. Copley, *Neutron scattering study of a quasi-two-dimensional spin-$\frac{1}{2}$ dimer system: Piperazinium hexachlorodicuprate under hydrostatic pressure*, Phys. Rev. B **82**, 184424 (2010).

[11] G. Perren, J. S. Möller, D. Hüvonen, A. A. Podlesnyak, and A. Zheludev, *Spin dynamics in pressure-induced magnetically ordered phases in* $(C_4H_{12}N_2)Cu_2Cl_6$, Phys. Rev. B **92**, 054413 (2015).

[12] B. S. Shastry and B. Sutherland, *Exact ground state of a quantum mechanical antiferromagnet*, Physica B+C **108**, 1069 (1981).

[13] M. Albrecht and F. Mila, *First-order transition between magnetic order and valence bond order in a 2D frustrated Heisenberg model*, Europhysics Letters (EPL) **34**, 145 (1996).

[14] S. Miyahara and K. Ueda, *Exact Dimer Ground State of the Two Dimensional Heisenberg Spin System* $SrCu_2(BO_3)_2$, Phys. Rev. Lett. **82**, 3701 (1999).

[15] Z. Weihong, C. J. Hamer, and J. Oitmaa, *Series expansions for a Heisenberg antiferromagnetic model for* $SrCu_2(BO_3)_2$, Phys. Rev. B **60**, 6608 (1999).

[16] A. Koga and N. Kawakami, *Quantum Phase Transitions in the Shastry-Sutherland Model for* $SrCu_2(BO_3)_2$, Phys. Rev. Lett. **84**, 4461 (2000).

[17] E. Müller-Hartmann, R. R. P. Singh, C. Knetter, and G. S. Uhrig, *Exact Demonstration of Magnetization Plateaus and First-Order Dimer-Néel Phase Transitions in a Modified Shastry-Sutherland Model for* $SrCu_2(BO_3)_2$, Phys. Rev. Lett. **84**, 1808 (2000).

[18] Y. Takushima, A. Koga, and N. Kawakami, *Competing Spin-Gap Phases in a Frustrated Quantum Spin System in Two Dimensions*, Journal of the Physical Society of Japan **70**, 1369 (2001), https://doi.org/10.1143/JPSJ.70.1369.

[19] D. Carpentier and L. Balents, *Field theory for generalized Shastry-Sutherland models*, Phys. Rev. B **65**, 024427 (2001).

[20] C. H. Chung, J. B. Marston, and S. Sachdev, *Quantum phases of the Shastry-Sutherland antiferromagnet: Application to* $SrCu_2(BO_3)_2$, Phys. Rev. B **64**, 134407 (2001).

[21] W. Zheng, J. Oitmaa, and C. J. Hamer, *Phase diagram of the Shastry-Sutherland antiferromagnet*, Phys. Rev. B **65**, 014408 (2001).

[22] A. Läuchli, S. Wessel, and M. Sigrist, *Phase diagram of the quadrumerized Shastry-Sutherland model*, Phys. Rev. B **66**, 014401 (2002).

[23] M. Al Hajj and J.-P. Malrieu, *Phase transitions in the Shastry-Sutherland lattice*, Phys. Rev. B **72**, 094436 (2005).

[24] R. Darradi, J. Richter, and D. J. J. Farnell, *Coupled cluster treatment of the Shastry-Sutherland antiferromagnet*, Phys. Rev. B **72**, 104425 (2005).

[25] A. Isacsson and O. F. Syljuåsen, *Variational treatment of the Shastry-Sutherland antiferromagnet using projected entangled pair states*, Phys. Rev. E **74**, 026701 (2006).

[26] S. Moukouri, *Plaquette ground state of the Shastry-Sutherland model: Density-matrix renormalization-group calculations*, Phys. Rev. B **78**, 132405 (2008).

[27] M. Moliner, I. Rousochatzakis, and F. Mila, *Emergence of one-dimensional physics from the distorted Shastry-Sutherland lattice*, Phys. Rev. B **83**, 140414(R) (2011).

[28] P. Corboz and F. Mila, *Tensor network study of the Shastry-Sutherland model in zero magnetic field*, Phys. Rev. B **87**, 115144 (2013).

[29] D. C. Ronquillo and M. R. Peterson, *Identifying topological order in the Shastry-Sutherland model via entanglement entropy*, Phys. Rev. B **90**, 201108(R) (2014).

[30] Z. Wang and C. D. Batista, *Dynamics and Instabilities of the Shastry-Sutherland Model*, Phys. Rev. Lett. **120**, 247201 (2018).

[31] C. Boos, S. Crone, I. Niesen, P. Corboz, K. Schmidt, and F. Mila, *Theory of the intermediate phase of $SrCu_2(BO_3)_2$ under pressure*, arXiv preprint arXiv:1903.07887 (2019).

[32] C. Knetter and G. S. Uhrig, *Dynamic Structure Factor of the Two-Dimensional Shastry-Sutherland Model*, Phys. Rev. Lett. **92**, 027204 (2004).

[33] H. Kageyama, K. Yoshimura, R. Stern, N. V. Mushnikov, K. Onizuka, M. Kato, K. Kosuge, C. P. Slichter, T. Goto, and Y. Ueda, *Exact Dimer Ground State and Quantized Magnetization Plateaus in the Two-Dimensional Spin System* $SrCu_2(BO_3)_2$, Phys. Rev. Lett. **82**, 3168 (1999).

[34] M. Zayed, C. Rüegg, A. Läuchli, C. Panagopoulos, S. Saxena, M. Ellerby, D. McMorrow, T. Strässle, S. Klotz, G. Hamel, et al., *4-spin plaquette singlet state in the Shastry–Sutherland compound $SrCu_2(BO_3)_2$*, Nature Physics **13**, 962 (2017).

[35] J. Guo, G. Sun, B. Zhao, L. Wang, W. Hong, V. A. Sidorov, N. Ma, Q. Wu, S. Li, Z. Y. Meng, et al., *Quantum phases of $Sr_2Cu_2(BO_3)_2$ from high-pressure thermodynamics*, arXiv e-prints arXiv:1904.09927 (2019).

[36] S. Haravifard, A. Banerjee, J. C. Lang, G. Srajer, D. M. Silevitch, B. D. Gaulin, H. A. Dabkowska, and T. F. Rosenbaum, *Continuous and discontinuous quantum phase transitions in a model two-dimensional magnet*, Proceedings of the National Academy of Sciences **109**, 2286 (2012).

[37] T. Waki, K. Arai, M. Takigawa, Y. Saiga, Y. Uwatoko, H. Kageyama, and Y. Ueda, *A Novel Ordered Phase in $SrCu_2(BO_3)_2$ under High Pressure*, Journal of the Physical Society of Japan **76**, 073710 (2007), https://doi.org/10.1143/JPSJ.76.073710.

[38] T. Sakurai, Y. Hirao, K. Hijii, S. Okubo, H. Ohta, Y. Uwatoko, K. Kudo, and Y. Koike, *Direct Observation of the Quantum Phase Transition of*

$SrCu_2(BO_3)_2$ by High-Pressure and Terahertz Electron Spin Resonance, Journal of the Physical Society of Japan **87**, 033701 (2018).

[39] N. Shannon, T. Momoi, and P. Sindzingre, *Nematic Order in Square Lattice Frustrated Ferromagnets*, Phys. Rev. Lett. **96**, 027213 (2006).

[40] H. T. Ueda and K. Totsuka, *Ground-state phase diagram and magnetic properties of a tetramerized spin-1/2 J_1-J_2 model: BEC of bound magnons and absence of the transverse magnetization*, Phys. Rev. B **76**, 214428 (2007).

[41] R. Shindou, S. Yunoki, and T. Momoi, *Dynamical spin structure factors of quantum spin nematic states*, Phys. Rev. B **87**, 054429 (2013).

[42] H. T. Ueda and T. Momoi, *Nematic phase and phase separation near saturation field in frustrated ferromagnets*, Phys. Rev. B **87**, 144417 (2013).

[43] H. T. Ueda, *Magnetic phase diagram slightly below the saturation field in the stacked J1-J2model in the square lattice with the JCinterlayer coupling*, Journal of the Physical Society of Japan **84**, 023601 (2015).

[44] A. A. Tsirlin and H. Rosner, *Extension of the spin-$\frac{1}{2}$ frustrated square lattice model: The case of layered vanadium phosphates*, Phys. Rev. B **79**, 214417 (2009).

[45] S. Sachdev, *Quantum Phase transitions* (Cambridge University Press, Cambridge, UK, 1999).

[46] C. Lacroix, P. Mendels, and F. Mila, *Introduction to frustrated magnetism: materials, experiments, theory*, vol. 164 (Springer Science & Business Media, 2011).

[47] M. Matsumoto, C. Yasuda, S. Todo, and H. Takayama, *Ground-state phase diagram of quantum Heisenberg antiferromagnets on the anisotropic dimerized square lattice*, Phys. Rev. B **65**, 014407 (2001).

[48] See, for example, A. Auerbach, Interacting Electrons and Quantum Magnetism, Springer, New York, 1944, chapter 9.

[49] M. Matsumoto, B. Normand, T. M. Rice, and M. Sigrist, *Field- and pressure-induced magnetic quantum phase transitions in* $TlCuCl_3$, Phys. Rev. B **69**, 054423 (2004).

[50] M. B. Stone, I. Zaliznyak, D. H. Reich, and C. Broholm, *Frustration-induced two-dimensional quantum disordered phase in piperazinium hexachlorodicuprate*, Phys. Rev. B **64**, 144405 (2001).

[51] L. P. Battaglia, A. B. Corradi, U. Geiser, R. D. Willett, A. Motori, F. Sandrolini, L. Antolini, T. Manfredini, L. Menabue, and G. C. Pellacani, *The crystal structures, magnetic and electrical properties of two polymeric chlorocuprate(II) compounds*, J. Chem. Soc. Dalton Trans. pp. 265–271 (1988).

[52] D. Hüvonen, S. Zhao, G. Ehlers, M. Månsson, S. N. Gvasaliya, and A. Zheludev, *Excitations in a quantum spin liquid with random bonds*, Phys. Rev. B **86**, 214408 (2012).

[53] M. B. Stone, I. A. Zaliznyak, T. Hong, C. L. Broholm, and D. H. Reich, *Quasiparticle breakdown in a quantum spin liquid*, Nature **440**, 187 (2006).

[54] G. Perren, Ph.D. thesis, ETH Zurich, Zurich (2018).

[55] T. Yankova, D. Hüvonen, S. Mühlbauer, D. Schmidiger, E. Wulf, S. Zhao, A. Zheludev, T. Hong, V. Garlea, R. Custelcean, et al., *Crystals for neutron scattering studies of quantum magnetism*, Philosophical Magazine **92**, 2629 (2012), http://www.tandfonline.com/doi/pdf/10.1080/14786435.2012.669072.

[56] B. S. Shastry and B. Sutherland, *Exact ground state of a quantum mechanical antiferromagnet*, Physica B+C **108**, 1069 (1981).

[57] X. Z. Lu, X. Wu, and H. J. Xiang, *General microscopic model of magnetoelastic coupling from first principles*, Phys. Rev. B **91**, 100405 (2015).

[58] W. Voigt, *Lehrbuch der kristallphysik (mit ausschluss der kristalloptik), edited by bg teubner and jw edwards, leipzig berlin*, Ann Arbor, Mich (1928).

[59] C. Vecchini, O. Adamopoulos, L. Chapon, A. Lappas, H. Kageyama, Y. Ueda, and A. Zorko, *Structural distortions in the spin-gap regime of the quantum antiferromagnet $SrCu_2(BO_3)_2$*, Journal of Solid State Chemistry **182**, 3275 (2009).

[60] C. Raas, U. Löw, G. S. Uhrig, and R. W. Kühne, *Spin-phonon chains with bond coupling*, Phys. Rev. B **65**, 144438 (2002).

[61] K.-Y. Choi, A. Oosawa, H. Tanaka, and P. Lemmens, *Interplay of triplets and lattice degrees of Freedom in the coupled spin dimer system* $KCuCl_3$, Phys. Rev. B **72**, 024451 (2005).

[62] S. Bettler, G. Simutis, G. Perren, D. Blosser, S. Gvasaliya, and A. Zheludev, *High-pressure Raman study of the quantum magnet* $(\mathbf{C_4H_{12}N_2})\mathbf{Cu_2Cl_6}$, Phys. Rev. B **96**, 174431 (2017).

[63] G. Radtke, A. Saúl, H. A. Dabkowska, M. B. Salamon, and M. Jaime, *Magnetic nanopantograph in the $SrCu_2(BO_3)_2$ Shastry–Sutherland lattice*, Proceedings of the National Academy of Sciences **112**, 1971 (2015).

[64] K.-Y. Choi, Y. G. Pashkevich, K. V. Lamonova, H. Kageyama, Y. Ueda, and P. Lemmens, *Strong anharmonicity and spin-phonon coupling in the quasi-two-dimensional quantum spin system* $Sr_{1-x}Ba_xCu_2(BO_3)_2$, Phys. Rev. B **68**, 104418 (2003).

[65] S. Miyahara, F. Becca, and F. Mila, *Theory of spin-density profile and lattice distortion in the magnetization plateaus of* $SrCu_2(BO_3)_2$, Phys. Rev. B **68**, 024401 (2003).

[66] R. W. Smith and D. A. Keszler, *Synthesis, structure, and properties of the orthoborate SrCu2(BO3)2*, Journal of Solid State Chemistry **93**, 430 (1991).

[67] A. Smerald and N. Shannon, *Theory of NMR $1/T_1$ relaxation in a quantum spin nematic in an applied magnetic field*, Phys. Rev. B **93**, 184419 (2016).

[68] M. Skoulatos, J. P. Goff, N. Shannon, E. E. Kaul, C. Geibel, A. P. Murani, M. Enderle, and A. R. Wildes, *Spin correlations in the frustrated square lattice Pb2VO(PO4)2*, Journal of Magnetism and Magnetic Materials (2007).

[69] M. Skoulatos, J. P. Goff, C. Geibel, E. E. Kaul, R. Nath, N. Shannon, B. Schmidt, A. P. Murani, P. P. Deen, M. Enderle, et al., *Spin correlations and exchange in square-lattice frustrated ferromagnets*, EPL (Europhysics Letters) **88**, 57005 (2009).

[70] E. E. Kaul, H. Rosner, N. Shannon, R. V. Shpanchenko, and C. Geibel, *Evidence for a frustrated square lattice with ferromagnetic nearest-neighbor interaction in the new compound Pb2VO(PO 4)2*, Journal of Magnetism and Magnetic Materials (2004).

[71] T. Förster, F. A. Garcia, T. Gruner, E. E. Kaul, B. Schmidt, C. Geibel, and J. Sichelschmidt, *Spin fluctuations with two-dimensional XY behavior in a frustrated $S = \frac{1}{2}$ square-lattice ferromagnet*, Phys. Rev. B **87**, 180401(R) (2013).

[72] R. Nath, Y. Furukawa, F. Borsa, E. E. Kaul, M. Baenitz, C. Geibel, and D. C. Johnston, *Single-crystal ^{31}P NMR studies of the frustrated square-lattice compound $Pb_2(VO)(PO_4)_2$*, Phys. Rev. B **80**, 214430 (2009).

[73] E. E. Kaul, Ph.D. thesis, Technische Universität Dresden (2005).

[74] V. Shpanchenko, E. E. Kaul, C. Geibel, and E. V. Antipov, Acta Crystallog. C **62**, 88 (2006).

[75] B. Ouladdiaf, J. Archer, G. McIntyre, A. Hewat, D. Brau, and S. York, *OrientExpress: A new system for Laue neutron diffraction*, Physica B: Condensed Matter **385-386**, 1052 (2006).

[76] A. Oosawa, K. Kakurai, T. Osakabe, M. Nakamura, M. Takeda, and H. Tanaka, J. Phys. Soc. Jpn. **73**, 1446 (2004).

[77] S. Hayashida, O. Zaharko, N. Kurita, H. Tanaka, M. Hagihala, M. Soda, S. Itoh, Y. Uwatoko, and T. Masuda, *Pressure-induced quantum phase transition in the quantum antiferromagnet* $CsFeCl_3$, Phys. Rev. B **97**, 140405 (2018).

[78] A. Podleznyak, private communication (2017).

[79] A. Podlesnyak, M. Loguillo, G. M. Rucker, B. Haberl, R. Boehler, G. Ehlers, L. L. Daemen, D. Armitage, M. D. Frontzek, and M. Lumsden, *Clamp cell with in situ pressure monitoring for low-temperature neutron scattering measurements*, High Pressure Research **38**, 482 (2018), https://doi.org/10.1080/08957959.2018.1519560.

[80] C.-S. Zha, H.-k. Mao, and R. J. Hemley, *Elasticity of MgO and a primary pressure scale to 55 GPa*, Proceedings of the National Academy of Sciences **97**, 13494 (2000), https://www.pnas.org/content/97/25/13494.full.pdf.

[81] Y. Feng, R. Jaramillo, J. Wang, Y. Ren, and T. F. Rosenbaum, *Invited Article: High-pressure techniques for condensed matter physics at low temperature*, Review of Scientific Instruments **81**, 041301 (2010).

[82] W. Hayes and R. Loudon, *Scattering of Light by Crystals*, Dover science books (Dover Publications, 2004), ISBN 9780486438665.

[83] M. Cottam and D. Lockwood, *Light scattering in magnetic solids*, Wiley-Interscience publication (Wiley, 1986), ISBN 9780471817017.

[84] G. Landsberg and L. Mandelstam, *Über die Lichtzerstreuung in Kristallen*, Zeitschrift für Physik **50**, 769 (1928).

[85] S. M. Shapiro, D. C. O'Shea, and H. Z. Cummins, *Raman Scattering Study of the Alpha-Beta Phase Transition in Quartz*, Phys. Rev. Lett. **19**, 361 (1967).

[86] P. A. Fleury and R. Loudon, *Scattering of Light by One- and Two-Magnon Excitations*, Phys. Rev. **166**, 514 (1968).

[87] M. E. Valentine, S. Koohpayeh, W. A. Phelan, T. M. McQueen, P. F. Rosa, Z. Fisk, and N. Drichko, *Breakdown of the Kondo insulating state in SmB 6 by introducing Sm vacancies*, Physical Review B **94**, 075102 (2016).

[88] T. Moriya, *Theory of Light Scattering by Magnetic Crystals*, Journal of the Physical Society of Japan **23**, 490 (1967), https://doi.org/10.1143/JPSJ.23.490.

[89] R. Elliott and M. Thorpe, *The effects of magnon-magnon interaction on the two-magnon spectra of antiferromagnets*, Journal of Physics C: Solid State Physics **2**, 1630 (1969).

[90] E. Sterer, M. P. Pasternak, and R. D. Taylor, *A multipurpose miniature diamond anvil cell*, Review of Scientific Instruments **61**, 1117 (1990).

[91] K. Yokogawa, K. Murata, H. Yoshino, and S. Aoyama, *Solidification of High-Pressure Medium Daphne 7373*, Japanese Journal of Applied Physics **46**, 3636 (2007).

[92] N. Tateiwa and Y. Haga, *Evaluations of pressure-transmitting media for cryogenic experiments with diamond anvil cell*, Review of Scientific Instruments **80**, 123901 (2009).

[93] S. Klotz, J.-C. Chervin, P. Munsch, and G. L. Marchand, *Hydrostatic limits of 11 pressure transmitting media*, Journal of Physics D: Applied Physics **42**, 075413 (2009).

[94] D. D. Ragan, R. Gustavsen, and D. Schiferl, *Calibration of the ruby R 1 and R 2 fluorescence shifts as a function of temperature from 0 to 600 K*, Journal of applied physics **72**, 5539 (1992).

[95] R. Bentley, *HANDBOOK OF TEMPERATURE MEASUREMENT.: Volume 1, Temperature and Humidity Measurement*, Handbook of Temperature Measurement (Springer, 1998), ISBN 9789814021098.

[96] G. L. Squires, *Introduction To The theory Of Thermal neutron Scattering* (Cambridge University Press, 1978).

[97] A. Furrer and T. Mesot, JoëL. Strässle, *Neutron Scattering in Condensed Matter Physics* (2009).

[98] E. Fermi, *Paper no. 119a "Sul moto dei neutroni nelle sostanze idrogenate"*, in *Enrico Fermi — Collected papers(Note e memorie)*, edited by E. Segrè, E. Amaldi, H. Anderson, E. Persico, F. Rasetti, C. Smith, and A. Wattenberg (The University of Chicago Press, 1962), vol. 1, pp. 943–979.

[99] J. Kopecky, J.-C. Sublet, J. Simpson, R. Forrest, and D. Nierop, Tech. Rep., International Atomic Energy Agency (1997).

[100] V. F. Sears, *Neutron scattering lengths and cross sections*, Neutron News **3**, 26 (1992).

[101] A. Wilson and E. Prince, eds., *International Tables for Crystallography, Vol. C* (Kluwer Academic Publishers, Dordrecht, Boston, London, 1992).

[102] Ressouche, E., *Reminder: Magnetic structures description and determination by neutron diffraction*, JDN **13**, 02001 (2014).

[103] J. A. Rodriguez, D. M. Adler, P. C. Brand, C. Broholm, J. C. Cook, C. Brocker, R. Hammond, Z. Huang, P. Hundertmark, J. W. Lynn, et al., *MACS—a new high intensity cold neutron spectrometer at NIST*, Measurement Science and Technology **19**, 034023 (2008).

[104] K. Schmalzl, W. Schmidt, S. Raymond, H. Feilbach, C. Mounier, B. Vettard, and T. Brückel, *The upgrade of the cold neutron three-axis spectrometer IN12 at the ILL*, Nuclear Instruments and Methods in Physics Research Section A: Accelerators, Spectrometers, Detectors and Associated Equipment **819**, 89 (2016).

[105] S. Foner, *Versatile and Sensitive Vibrating-Sample Magnetometer*, Review of Scientific Instruments **30**, 548 (1959).

[106] G. W. Van Oosterhout, *A rapid method for measuring coercive force and other ferromagnetic properties of very small samples*, Applied Scientific Research, Section B **6**, 101 (1957).

[107] *Vibrating Sample Magnetometer (VSM) Option User's Manual*, Quantum Design (2011).

[108] A. A. Tsirlin, B. Schmidt, Y. Skourski, R. Nath, C. Geibel, and H. Rosner, *Exploring the spin-$\frac{1}{2}$ frustrated square lattice model with high-field magnetization studies*, Phys. Rev. B **80**, 132407 (2009).

[109] R. Griessen, *A capacitance torquemeter for de Haas-van Alphen measurements*, Cryogenics **13**, 375 (1973).

[110] M. Qvarford, K. Heeck, J. G. Lensink, R. J. Wijngaarden, and R. Griessen, *Microtorquemeter for magnetization measurements on small superconducting samples*, Review of Scientific Instruments **63**, 5726 (1992), https://doi.org/10.1063/1.1143355.

[111] Y. Feng, K. Y. Povarov, and A. Zheludev, *Magnetic phase diagram of the strongly frustrated quantum spin chain system* $PbCuSO_4(OH)_2$ *in tilted magnetic fields*, Phys. Rev. B **98**, 054419 (2018).

[112] P. Lemmens, M. Grove, M. Fischer, G. Güntherodt, V. N. Kotov, H. Kageyama, K. Onizuka, and Y. Ueda, *Collective Singlet Excitations and Evolution of Raman Spectral Weights in the 2D Spin Dimer Compound* $SrCu_2(BO_3)_2$, Phys. Rev. Lett. **85**, 2605 (2000).

[113] K.-Y. Choi, G. Güntherodt, A. Oosawa, H. Tanaka, and P. Lemmens, *Spin dynamics of the spin dimer system* $TlCuCl_3$ *probed by Raman spectroscopy*, Phys. Rev. B **68**, 174412 (2003).

[114] G. Simutis, S. Gvasaliya, F. Xiao, C. P. Landee, and A. Zheludev, *Raman study of spin excitations in the tunable quantum spin ladder* $Cu(Qnx)(Cl_{1-x}Br_x)_2$, Phys. Rev. B **93**, 094412 (2016).

[115] P. Giannozzi, S. Baroni, N. Bonini, M. Calandra, R. Car, C. Cavazzoni, D. Ceresoli, G. L. Chiarotti, M. Cococcioni, I. Dabo, et al., *QUANTUM ESPRESSO: a modular and open-source software project for quantum simulations of materials*, Journal of Physics: Condensed Matter **21**, 395502 (2009).

[116] R. Sabatini, T. Gorni, and S. de Gironcoli, *Nonlocal van der Waals density functional made simple and efficient*, Phys. Rev. B **87**, 041108 (2013).

[117] O. A. Vydrov and T. V. Voorhis, *Nonlocal van der Waals density functional: The simpler the better*, The Journal of Chemical Physics **133**, 244103 (2010).

[118] A. D. Corso, *Pseudopotentials periodic table: From H to Pu*, Computational Materials Science **95**, 337 (2014).

[119] A. Oueslati, A. Bulou, F. Calvayrac, K. Adil, M. Gargouri, and F. Hlel, *Infrared, polarized Raman and ab initio calculations of the vibrational spectra of [N(C3H7)4]2Cu2Cl6 crystals*, Vibrational Spectroscopy **64**, 10 (2013).

[120] W. Brenig and K. W. Becker, *Magnetism of a tetrahedral cluster spin chain*, Phys. Rev. B **64**, 214413 (2001).

[121] K. P. Schmidt, C. Knetter, and G. S. Uhrig, *Raman response in antiferromagnetic two-leg S = 1/2 Heisenberg ladders*, EPL (Europhysics Letters) **56**, 877 (2001).

[122] H. Kuroe, N. Takami, N. Niwa, T. Sekine, M. Matsumoto, F. Yamada, H. Tanaka, and K. Takemura, *Longitudinal magnetic excitation in KCuCl 3 studied by Raman scattering under hydrostatic pressures*, Journal of Physics: Conference Series **400**, 032042 (2012).

[123] A. Gozar, B. S. Dennis, H. Kageyama, and G. Blumberg, *Symmetry and light coupling to phononic and collective magnetic excitations in* $SrCu_2(BO_3)_2$, Phys. Rev. B **72**, 064405 (2005).

[124] G. Prandini, A. Marrazzo, I. E. Castelli, N. Mounet, and N. Marzari, *Precision and efficiency in solid-state pseudopotential calculations*, npj Computational Materials **4**, 72 (2018).

[125] K. Lejaeghere, G. Bihlmayer, T. Björkman, P. Blaha, S. Blügel, V. Blum, D. Caliste, I. E. Castelli, S. J. Clark, A. Dal Corso, et al., *Reproducibility in density functional theory calculations of solids*, Science **351** (2016).

[126] D. R. Hamann, *Optimized norm-conserving Vanderbilt pseudopotentials*, Phys. Rev. B **88**, 085117 (2013).

[127] M. Schlipf and F. Gygi, *Optimization algorithm for the generation of ONCV pseudopotentials*, Computer Physics Communications **196**, 36 (2015).

[128] G. Prandini, A. Marrazzo, I. E. Castelli, N. Mounet, and N. Marzari, *A Standard Solid State Pseudopotentials (SSSP) library optimized for precision and efficiency (Version 1.1, data download)* (2018).

[129] K. F. Garrity, J. W. Bennett, K. M. Rabe, and D. Vanderbilt, *Pseudopotentials for high-throughput DFT calculations*, Computational Materials Science **81**, 446 (2014).

[130] M. Balkanski, R. Wallis, and E. Haro, *Anharmonic effects in light scattering due to optical phonons in silicon*, Physical Review B **28**, 1928 (1983).

[131] J. Rodríguez-Carvajal, *Recent advances in magnetic structure determination by neutron powder diffraction*, Physica B: Condensed Matter **192**, 55 (1993).

[132] S. Toth and B. Lake, *Linear spin wave theory for single-Q incommensurate magnetic structures*, Journal of Physics: Condensed Matter **27**, 166002 (2015).

[133] A. Zheludev, *ResLib Resolution Library for MatLab*, http://www.neutron.ethz.ch/research/resources/reslib (2009).

[134] M. Popovici, Acta Cryst. **A31**, 507 (1975).

[135] B. Schmidt, M. Siahatgar, and P. Thalmeier, *Frustrated local-moment models for iron pnictide magnetism*, Phys. Rev. B **81**, 165101 (2010).

[136] S. Bettler, F. Landolt, O. M. Aksoy, Z. Yan, S. Gvasaliya, Y. Qiu, E. Ressouche, K. Beauvois, S. Raymond, A. N. Ponomaryov, et al., *Magnetic structure and spin waves in the frustrated ferro-antiferromagnet* $Pb_2VO(PO_4)_2$, Phys. Rev. B **99**, 184437 (2019).

[137] J. Tranquada and G. Shirane, *Neutron scattering studies of magnetic correlations in the layered cuprates*, Physica C: Superconductivity and its Applications **162-164**, 849 (1989).

[138] M. Pregelj, A. Zorko, O. Zaharko, H. Nojiri, H. Berger, L. Chapon, and D. Arčon, *Spin-stripe phase in a frustrated zigzag spin-1/2 chain*, Nature communications **6**, 7255 (2015).

[139] A. Orlova, E. L. Green, J. M. Law, D. I. Gorbunov, G. Chanda, S. Krämer, M. Horvatić, R. K. Kremer, J. Wosnitza, and G. L. J. A. Rikken, *Nuclear*

Magnetic Resonance Signature of the Spin-Nematic Phase in $LiCuVO_4$ *at High Magnetic Fields*, Phys. Rev. Lett. **118**, 247201 (2017).

[140] Y. Kohama, H. Ishikawa, A. Matsuo, K. Kindo, N. Shannon, and Z. Hiroi, *Possible observation of quantum spin-nematic phase in a frustrated magnet*, Proceedings of the National Academy of Sciences **116**, 10686 (2019), https://www.pnas.org/content/116/22/10686.full.pdf.

[141] M. Skoulatos, F. Rucker, G. J. Nilsen, A. Bertin, E. Pomjakushina, J. Ollivier, A. Schneidewind, R. Georgii, O. Zaharko, L. Keller, et al., *Putative spin-nematic phase in* $BaCdVO(PO_4)_2$, Phys. Rev. B **100**, 014405 (2019).

[142] V. K. Bhartiya, K. Y. Povarov, D. Blosser, S. Bettler, Z. Yan, S. Gvasaliya, S. Raymond, E. Ressouche, K. Beauvois, J. Xu, et al., *Presaturation phase with no dipolar order in a quantum ferro-antiferromagnet*, Phys. Rev. Research **1**, 033078 (2019).

[143] M. Pregelj, A. Zorko, M. Klanjšek, O. Zaharko, J. S. White, O. Prokhnenko, M. Bartkowiak, H. Nojiri, H. Berger, and D. Arčon, *Magnetic ground state of the frustrated spin-*$\frac{1}{2}$ *chain compound* β*–*$TeVO_4$ *at high magnetic fields*, Phys. Rev. B **100**, 094433 (2019).

[144] M. Yoshida, M. Takigawa, H. Yoshida, Y. Okamoto, and Z. Hiroi, *Phase Diagram and Spin Dynamics in Volborthite with a Distorted Kagome Lattice*, Phys. Rev. Lett. **103**, 077207 (2009).

[145] M. Yoshida, M. Takigawa, S. Krämer, S. Mukhopadhyay, M. Horvatić, C. Berthier, H. Yoshida, Y. Okamoto, and Z. Hiroi, *High-Field Phase Diagram and Spin Structure of Volborthite Cu3V2O7(OH)2·2H2O*, Journal of the Physical Society of Japan **81**, 024703 (2012), https://doi.org/10.1143/JPSJ.81.024703.

[146] H. Ishikawa, M. Yoshida, K. Nawa, M. Jeong, S. Krämer, M. Horvatić, C. Berthier, M. Takigawa, M. Akaki, A. Miyake, et al., *One-Third Magnetization Plateau with a Preceding Novel Phase in Volborthite*, Phys. Rev. Lett. **114**, 227202 (2015).

[147] J. Schlappa, T. Schmitt, F. Vernay, V. N. Strocov, V. Ilakovac, B. Thielemann, H. M. Ronnow, S. Vanishri, A. Piazzalunga, X. Wang, et al., Phys. Rev. Lett. **103**, 047401 (2009).

[148] C. C. Homes, S. V. Dordevic, A. Gozar, G. Blumberg, T. Rõ om, D. Hüvonen, U. Nagel, A. D. LaForge, D. N. Basov, and H. Kageyama, *Infrared spectra of the low-dimensional quantum magnet $SrCu_2(BO_3)_2$: Measurements and ab initio calculations*, Phys. Rev. B **79**, 125101 (2009).

List of Figures